Optimization of a Low-melting Alloy for Fused Filament Fabrication

by

Kimball E. Andersen

B.Sc., University of California Merced, 2013

Thesis Submitted in Partial Fulfillment of the
Requirements for the Degree of
Master of Applied Science

in the
School of Mechatronic Systems Engineering
Faculty of Applied Sciences

© Kimball E. Andersen 2015

SIMON FRASER UNIVERSITY

Summer 2015

All rights reserved.
However, in accordance with the *Copyright Act of Canada*, this work may be reproduced, without authorization, under the conditions for "Fair Dealing." Therefore, limited reproduction of this work for the purposes of private study, research, criticism, review and news reporting is likely to be in accordance with the law, particularly if cited appropriately.

Approval

Name:	**Kimball E. Andersen**
Degree:	**Master of Applied Science**
Title:	***Optimization of a Low-melting Alloy for Fused Filament Fabrication***
Examining Committee:	**Chair:** Mehrdad Moallem Professor

Woo Soo Kim
Senior Supervisor
Assistant Professor

Kevin Oldknow
Supervisor
Lecturer

Krishna Vijayaraghavan
Internal Examiner
Assistant Professor

Date Defended: August 13, 2015

Abstract

With low-cost Fused Filament Fabrication (FFF) systems proliferating among researchers, developing new filament materials to expand the design capabilities of 3D printed objects has become a focus for research. One material property that has been difficult to achieve though is high conductivity, which would enable the integration of embedded circuitry into functional 3D printed devices. This thesis presents the optimization and integration of low-melting alloys into a FFF system for the production of FFF metal components. The material, extrusion system, and the print parameters were optimized to enable reliable extrusion of the selected non-eutectic alloy. By combining this new material with existing FFF plastics, a 3D printed device with functional electronic circuits will become possible.

Keywords: Fused Filament Fabrication; 3D Printing; Low-melting Alloy; Additive Manufacturing; Multi Material Additive Manufacturing

For my loving wife, Robyn, who has provided me with support and encouragement when I needed it most. And to my daughter, Leithe, who never ceases to amaze me with her boundless energy, and for the inspiration and joy she has brought to my life.

Acknowledgements

I wish to thank my advisor, Dr. Woo Soo Kim, for his support on this project, as well as the other members of my thesis committee: Kevin Oldknow, Krishna Vijayaraghavan, and Mehrdad Moallem.

To the staff of the SFU MSE department, a heartfelt thank you for all of your hard work keeping the program operating, and especially to Zain and Mustafa, who were always willing to help when I had questions or needed to work in the machine shop.

This work made use of the 4D LABS shared facilities supported by the Canada Foundation for Innovation (CFI), British Columbia Knowledge Development Fund (BCKDF), Western Economic Diversification Canada (WD), and Simon Fraser Uiversity (SFU).

Finally, it has been an honor working with all of the other members of the stretchable devices laboratory, and our many conversations, on topic or off, were always a pleasure.

Table of Contents

Approval ii
Abstract iii
Dedication iv
Acknowledgements v
Table of Contents vi
List of Tables ix
List of Figures x
List of Equations xii
List of Acronyms xiii

Chapter 1. Introduction 1
1.1. Motivation 4
1.2. Objectives 5
1.3. Contribution 5
1.4. Thesis Organization 6

Chapter 2. Filament-Based Additive Manufacturing (FAM) Systems 7
2.1. Mechanical Positioning System 7
2.1.1. Cartesian 8
2.1.2. SCARA 9
2.1.3. Delta Robot 10
2.2. Software and Electronic Control Systems 11
2.2.1. 3D Design Software 12
2.2.2. Slicing Software 13
2.2.3. Printer Host Software 16
2.2.4. Firmware and Printer Electronics 17
2.3. Material Deposition (Extruder) System 17
2.3.1. Material Driver (Cold End) 18
2.3.2. Liquifier (Hot End) 21
2.4. Accessories 26
2.4.1. Printer Bed 26
2.4.2. Build Chamber 26
2.4.3. Cooling Systems 27
2.4.4. Filament Management 28

Chapter 3. Experimental Equipment, Modifications, and Procedures 29
3.1. Rostock Max 29
3.1.1. Configuration and Modifications 30
Kraken Quad Extrusion System 30
Printer Control Board and Software 31
Custom Nozzle Fabrication 32
3.1.2. Delta Robot Kinematics 32
3D Model and Variable Definitions 33

Inverse Kinematics Problem 34
Jacobian Matrix 35
Condition Number and Local Conditioning Index 36
Optimization of Link Length 37
3.2. Fabrication of Low-melt Alloy Filament 38
3.2.1. Production of Molten Alloy 39
3.2.2. Production of Alloy Metal Filament....39
3.2.3. Filament Joining and Storage 41

Chapter 4. Design and Analysis of Low-melting Metal Alloy Filament 43
4.1. Background 44
4.1.1. Solder alloy background 45
4.1.2. Eutectic vs. Non-Eutectic....46
4.1.3. Prior Arts on 3D Printing of Low-melting Alloy 47
4.2. Materials Space Evaluation 48
4.2.1. Melting Range Optimization....50
4.2.2. Thermal and Electrical Conductivity....50
4.2.3. Dopant Effects....51
4.3. Filament Analysis 51
4.3.1. DSC....52
4.3.2. Cross Section Optical Images....53
4.3.3. SEM/EDS 54
4.3.4. Conductivity....57
4.3.5. Mechanical Properties 58
4.4. Fused Filament Fabrication of Metal Alloys 58
4.4.1. Nozzle Optimization....59
4.4.2. Optimizing print parameters....62
4.4.3. Printed material analysis....68
4.4.4. Multi-material printing 70

Chapter 5. Conclusion and Opportunities for Future Work....72
5.1. Conclusions....72
5.2. Opportunities for Future Work....73

References 75
Appendix A: Matlab code for LCI plot over build space 83
Appendix B: Matlab code for normalized arm length optimization 84
Appendix C: E3D Nozzle Design Document....85
Appendix D: Modified E3D Heater Block for P3D Nozzles....86
Appendix E: Phase diagrams of binary and ternary alloy systems 87
Appendix F: Activity series of metals 89
Appendix G: DSC data for metal alloy samples tested 90
Appendix H: EDXS spot mapping of alloy samples 92
Appendix I: Early test of SnZn eutectic commercial solder alloy 98
Appendix J: Record of experimental conditions and results for stainless steel nozzle print calibration....103

Appendix K: Record of experimental conditions and results for anodized nozzle print calibration 1 105
Appendix L: Record of experimental conditions and results for electroless nickel coated nozzle print calibration 114
Appendix M: Record of experimental conditions and results for anodized nozzle print calibration 2 120
Appendix N: Video of Sample 1 being printed 123

List of Tables

Table 1: Different infill styles available in Slic3r. 15
Table 2: Kinematic variable definitions 34
Table 3: Materials considered and their relevant properties. 49
Table 4: Melting parameters of the sample alloys determined by DSC. 52
Table 5: Resistance measurements of metal alloy filaments 58
Table 6: Nozzles tested with metal alloy system 60

List of Figures

Figure 1: Growth of open source 3D models on Thingiverse.com[4]. 2

Figure 2: Printed part categories comparison on 3DHubs[7]. 3

Figure 3: 3D Printer model breakdown from 3DHubs' June trend report[7]. 4

Figure 4: Cartesian coordinate 3D printers. 9

Figure 5: RepRap Morgan[14]. 10

Figure 6: Rostock linear delta robot 3D printer[16]. 11

Figure 7: Slicing artifacts due to sharp angles. 13

Figure 8: Adaptive Slicing for efficient layer height calculation. 16

Figure 9: RepRap printer cold ends. 19

Figure 10: Integrated filament delivery and extrusion system for consumable system[46]. 19

Figure 11: Multi nozzle single drive motor designs. 21

Figure 12: Early Stratasys liquifier designs demonstrating the improvement in extrusion pressure when switching to a shorter and more direct melt path. 23

Figure 13: Hierarchical design in E3D nozzles[60]. 25

Figure 14: Dual path-width print nozzle[61]. 25

Figure 15: Dual nozzle configuration of the Rostock Max. 30

Figure 16: Kraken quad nozzle system. 31

Figure 17: 3D render of the complete PULD system and diagram of a single arm. 33

Figure 18: Render of the simplified kinematic system. 34

Figure 19: Contour lines of the Local Conditioning Index across the maximal workspace of a PULD system with L=2R=2. 37

Figure 20: Good conditioned maximum inscribed circle radius vs. normalized arm length (LCI≥0.3). 38

Figure 21: Filament Casting Setup. 41

Figure 22: Filament joining jig. 42

Figure 23: Filament stored on spool, ready for 3D printing. 42

Figure 24: Phase diagram of Tin Bismuth binary alloy system. 47

Figure 25: Optical microscope images of cross sections of filament. 54

Figure 26: SEM image of cross section of Sn80Bi20 filament. 55

Figure 27: SEM image of cross section of Sn70Bi30 filament. 56

Figure 28: SEM image of cross section of Sn66Bi30Ag4 filament. 57
Figure 29: Stainless Steel nozzle after printing with metal alloy filaments. 60
Figure 30: Images of Al 2011 nozzle orifice erosion after printing with SnBi alloy. 61
Figure 31: Al 6061 nozzle with stainless steel nozzle-tip insert. 61
Figure 32: Al 6061 nozzle with hard anodized coating..... 62
Figure 33: Electroless Nickel coated brass nozzle prior to, and after use with metal alloy filament. 62
Figure 34: Sample 1 - The first object successfully printed using the Rostock Max from a low melting temperature SnBi alloy filament. 64
Figure 35: Sample 2 - Made using the same settings as Sample 1, but with a stainless steel nozzle with aluminum foil wrapped around the base of the tip, and a slightly elevated temperature of 225°C..... 64
Figure 36: Sample 3 - Made using the same settings as Sample 2, but with an increase in the nozzle temp to 230°C. 65
Figure 37: Samples 4&5 - Made with the same settings as sample 2, but elevated temperatures of 235°C and 240°C respectively..... 65
Figure 38: Overview of samples. 66
Figure 39: Effect of part-cooling fan on print quality. 67
Figure 40: Sn66Bi30Ag4 printed with Al6061 hard anodized nozzle..... 67
Figure 41: Etched cross section of printed SnBi printed layers showing the lack of a clearly defined interface between subsequent depositions. 68
Figure 42: Cross Sections of Sn66Bi30Ag4 prints and nozzle. 69
Figure 43: Part contamination resulting from heating of inactive nozzle due to zero clearance. 70
Figure 44: Printed traces in PLA channels. 71

List of Equations

Equation 1: Critical Load of a Column in Axial Loading. 19
Equation 2: Hagen Poiseuille equation for viscous flow in a cylindrical pipe. 25

List of Acronyms

ABS	Acrylonitrile Butadiene Styrene
AM	Additive Manufacturing
CAD	Computer Aided Design
CAM	Computer Aided Manufacture
CNC	Computer Numerical Control
DSC	Differential Scanning Calorimeter
ED(X)S	Energy Dispersive X-Ray Spectrometry
FAM	Filament Based Additive Manufacturing
FDM	Fused Deposition Modeling (Commercial trademark of Stratasys, equivalent to FFF)
FFF	Fused Filament Fabrication
GCode	CNC Communication and Programming Language
LOM	Layered Object Manufacturing
PEEK	polyEther Ether Ketone
PLA	polyLactic Acid
PTFE	polyTetraFlouroEthylene
RepRap	Replicating Rapid Prototyper
SEM	Scanning Electron Microscope
SFF	Solid Freeform Fabrication
SFU	Simon Fraser University
SLA	Stereolithography Apparatus
SLS	Selective Laser Sintering
STL	Commonly used file format in 3D Printing, defines a triangulated mesh of a three-dimensional object

Chapter 1.
Introduction

Additive Manufacturing (AM), or 3D printing as it is often referred to colloquially, was first introduced in 1984 with the invention of an experimental stereolithographic device by Charles Hull. But it wasn't until the commercialization of 3D Systems' stereolithography based 3D printer, SLA 1, that commercial 3D printers began to take off[1]. Following this, several other technologies for AM were commercialized including: Laminated Object Manufacturing (LOM) and Selective Laser Sintering (SLS) in 1986, and Fused Deposition Modeling (FDM) and MIT's inkjet binder-based 3D printing in 1989[2]. Early systems were primarily used in industry as a form of rapid prototyping due to a number of factors including: the high cost of the machines, the slow speed of production, and the relatively low quality of the parts. As new and more advanced technologies have emerged, the possibility to produce end-use parts on AM systems has become a reality, and the potential to create designs that are impossible to produce through other means has emerged. In May 2008 a major milestone in AM was reached when the first RepRap 3D printer built from parts created by a parent RepRap created its own part[3]. With the release of the open source RepRap 3D printer designs, a democratization of AM has begun, with users all over the world building and improving on the RepRap system, and sharing these improvements with the world through sites such as Thingiverse (Figure 1).

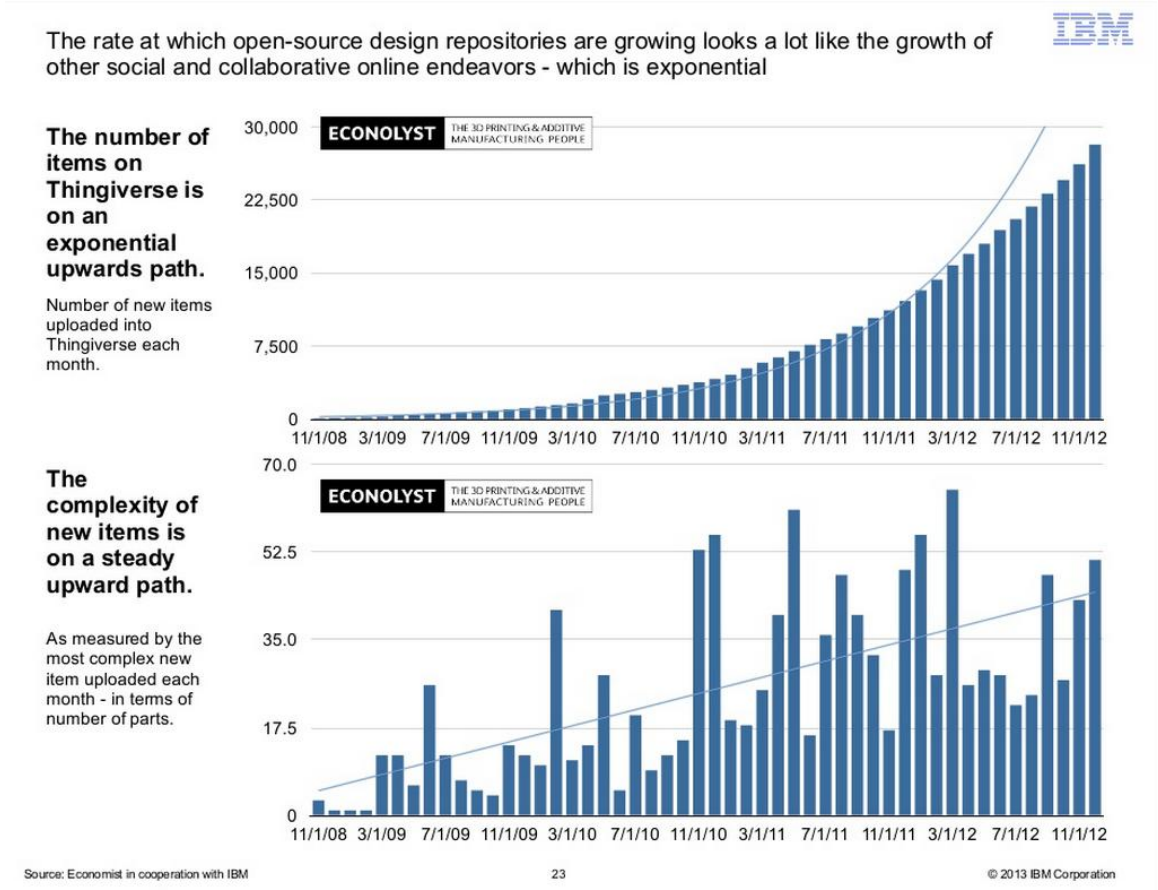

Figure 1: Growth of open source 3D models on Thingiverse.com[4].

It is interesting to compare the parallels between recent developments in 3D printing to historical developments in paper printing. As with early handwritten texts, most 3D parts prior to the introduction of 3D printing were manufactured by hand, or more recently through automated computer numerically controlled (CNC) production machines, or through injection molding, which are analogous to early printing presses as they are able to quickly mass-produce a single product, but require a long set up process for each new design. Like the introduction of inkjet printing, early 3D printers were expensive and difficult to maintain, making them most useful for large companies with the infrastructure to support them. However, as the technology matured, the home inkjet and laser printer were introduced and are now ubiquitous in our society. A similar proliferation of 3D printers is now beginning, with home 3D printers rapidly evolving and dropping in price with recent offerings of systems as low as $100 US[5] for a SLA system and $200 US[6] for a fused filament based system.

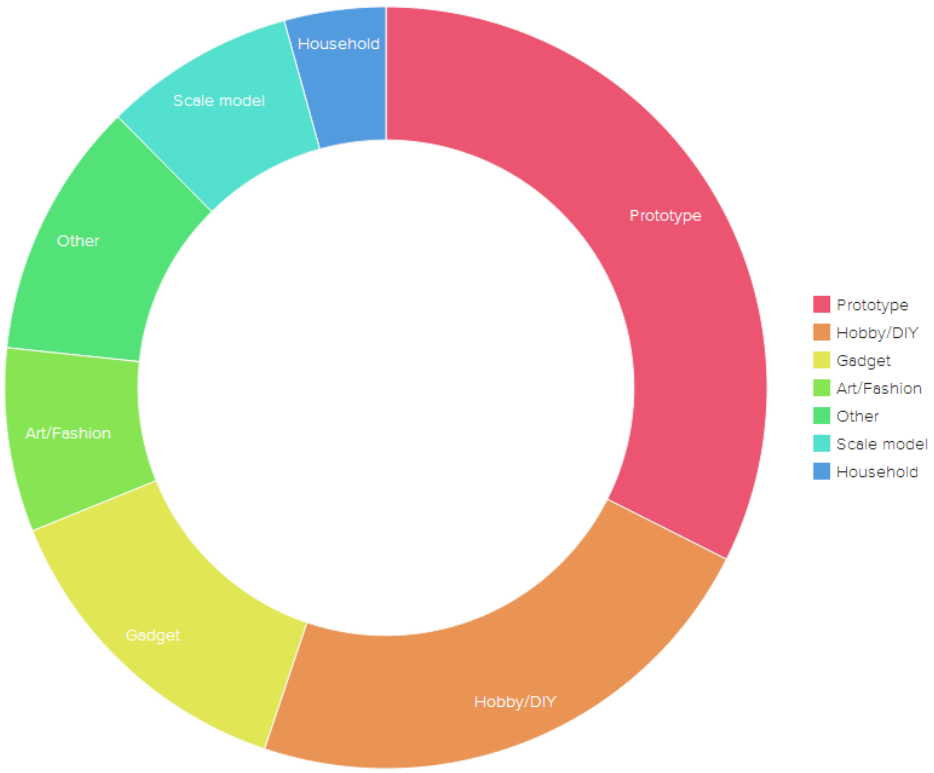

Figure 2: Printed part categories comparison on 3DHubs[7].
A comparison of the parts ordered through 3DHubs during May 2014 showing the end use application of the parts.

While these early home systems have some drawbacks and are primarily used by hobbyists and "prosumers", the rapid pace of innovation in this area is staggering. As these devices have proliferated, a plethora of new and innovative designs, as well as materials, has emerged. These printers are also providing new jobs and sources of innovation as they empower their users, sometimes referred to as Makers, to produce custom parts on demand. Several sites, including 3DHubs which has over 5000 printer listings[7], have leveraged these Makers' systems to provide a distributed print on demand service. The types of parts created by these printers (Figure 2) varies, and while AM for rapid prototyping is still a major fraction of their use, functional parts for end use are becoming more common. Another measure of the proliferation of home printers is the rate and complexity of designs posted to 3D model sharing sites such as Thingiverse (Figure 1), which mirrors the rise in collaborative online endeavors[4]. Because the majority of these home printers are filament-based (Figure 3), developing

new filament materials to expand the design space available has become a rapidly expanding market.

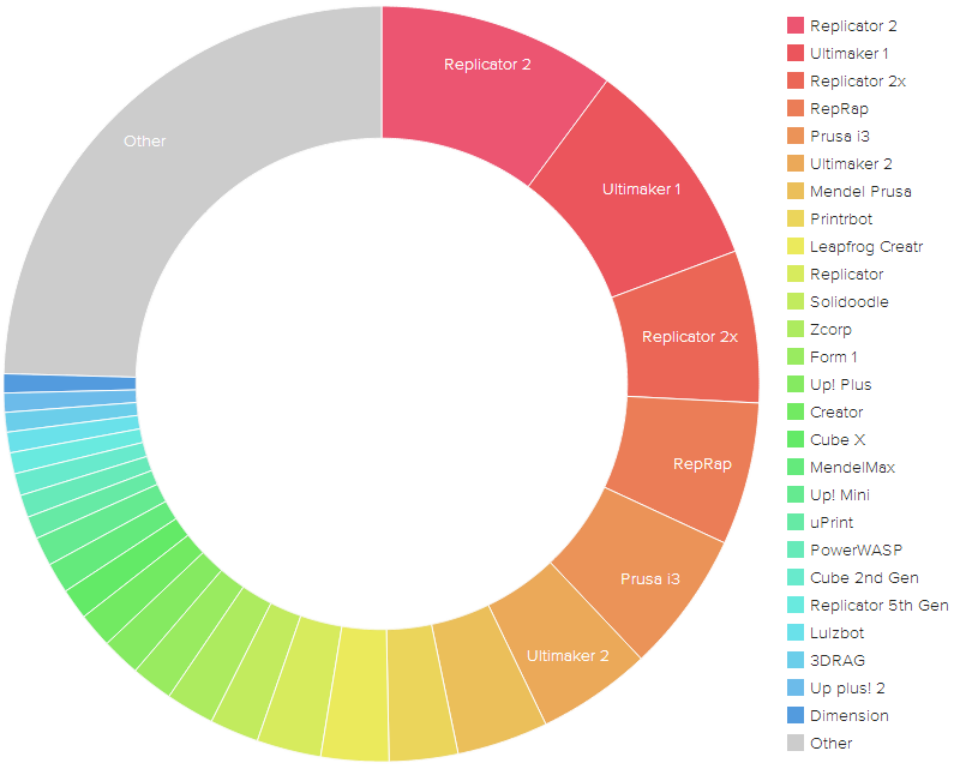

Figure 3: 3D Printer model breakdown from 3DHubs' June trend report[7].
With over 5000 printer listings, and the large majority filament-based systems, 3DHubs provides a listing service to allow Makers to connect with designers who wish to have their design printed.

1.1. Motivation

As new materials have entered the market for use in FFF 3D printers, the complexity and functionality built into the printed parts has increased dramatically (Figure 1). One of the most investigated types of materials are those that can conduct electricity, allowing the inclusion of 3D circuits in the printed part. While there have been some limited successes with polymer composites, such as carbomorph [8], a material made from carbon black, and more recently composites of PLA and graphene that have been released commercially [9], these materials have conductivities orders of magnitude

lower than the metal connections normally used in circuit applications. Another approach that has shown success in integrating electrical connections into 3D printed objects is to use highly conductive precious metal pastes, extruded from syringe-based systems[10]. While these are now showing promise in reaching the conductivities of normal metal interconnects, the price of the materials, in addition to the need for volatile solvents in the paste, as well as a separate delivery system, makes these materials less than ideal. The “Holy Grail” then is a filament that can be used in a standard extrusion system with minimal to no modification, which has the conductivity of a metal, but the extrusion characteristics of a polymer.

1.2. Objectives

To enable the integration of high current circuits into 3D printed objects, a much higher conductivity material needed to be developed for use in FFF based systems. To do this, a fundamental understanding of the systems used and how each of their components contributes to the printing process was required, therefore the first objective was to survey the different available designs and upgrades available for 3D printers, and select one which could serve as a test bed for the development of the new material. This printer needed to be easy to work on, so that any necessary modifications to enable the testing of the new material could be implemented. The second objective was the design and fabrication of the filament, beginning with a careful analysis of the materials available and their properties, followed by the fabrication of small samples of the filament for testing. The third objective was to identify and implement any modifications to the extrusion system needed for compatibility with the chosen material(s), as well as the optimization of the necessary print parameters needed for reliable printing of the new material. The final objective was to integrate the printed conductive material into a 3D object as a proof of concept.

1.3. Contribution

This work has expanded on, and laid new foundations for further improvements in low-melting alloys for FFF. While success was limited in some respects due to time

constraints, the demonstration of successful printing of several metal alloys was achieved, and a greater understanding of the underlying interplay between the material, the extrusion system, and the process parameters was gained.

1.4. Thesis Organization

This thesis is separated into three chapters related to work done during the Master's degree, in addition to an introduction and a conclusion which will attempt to also provide guidance to future improvements of this work. Chapter 2 covers the background information related to FFF 3D printing, including a brief history and a survey of the types of systems and components available and their applications and importance. Chapter 3 provides a record of the experimental equipment and procedures used and developed throughout this work, in addition to some analysis of the kinematics of the delta robot system. Chapter 4 begins with an introduction to low melting temperature alloys, and some of the research done with them, then moves onto the work done with them as part of this project. Finally, Chapter 5 summarizes the work done, and provides some guidance as to which avenues may be best to pursue in future work on this topic.

Chapter 2.
Filament-Based Additive Manufacturing (FAM) Systems

A filament-based 3D printer is composed of three major systems: the mechanical positioning system, the material deposition system, and the electronics and software used to control them. Each of these systems varies from printer to printer, and each variation provides opportunities for optimizations. In addition to the basic systems, each printer may feature additional accessories to improve print fidelity, speed, and/or add additional capabilities. After the print is completed, the printed part may undergo post-processing to remove support or improve the surface finish of the part. For a complete picture of the FAM process, part generation and processing software is also discussed in the context of FAM.

2.1. Mechanical Positioning System

The mechanical positioning system maneuvers the deposition system relative to the build platform in three-dimensions by moving one or both structures. Three major mechanical platforms, each of which provides unique advantages and challenges, have been used in 3D printer systems to date: Cartesian robot based systems, Delta robot based systems, and SCARA based systems. Most currently available systems use stepper motors to drive each axis, resulting in open loop control, which depends on a calibration step during startup to zero each axis, and step-counting to determine positioning. Servo control has also been utilized, but the added cost for high torque servomotors has made them much less common in low-end commercial systems.

2.1.1. Cartesian

Cartesian robots use a standard X-Y-Z system with three orthogonal linear actuators. Different arrangements are possible, with either the build plate or the nozzle moving in each of the axes. Since all movements of the actuators are directly proportional to movements in the principal axis, no complex kinematic relationships are required, reducing the processing power required to convert movement commands to motor commands. Configurations in which the build platform moves in X or Y require more torque to achieve rapid accelerations, requiring larger and more expensive motors; these also risk dislodging the print, especially when the printed object has a high mass to contact area ratio. A majority of the commercial printers available use a cartesian configuration due to its simplicity and proven reliability. Examples include the Makerbot Replicator, RepRap Mendel, Solidoodle, and Stratasys FDM systems (Figure 4 a,b). A more recent design in Cartesian-style printers is the H-Bot X-Y stage (Figure 4 c). This mounts both the X and Y motors onto the frame, and uses a single (or double) belt looped in an H configuration to drive the print head. The advantage of this configuration is that it allows the use of heavier higher torque motors without increasing the weight of the carriage, but the added belt length means that the belt tension must be increased to decrease backlash, which requires a more rigid frame.

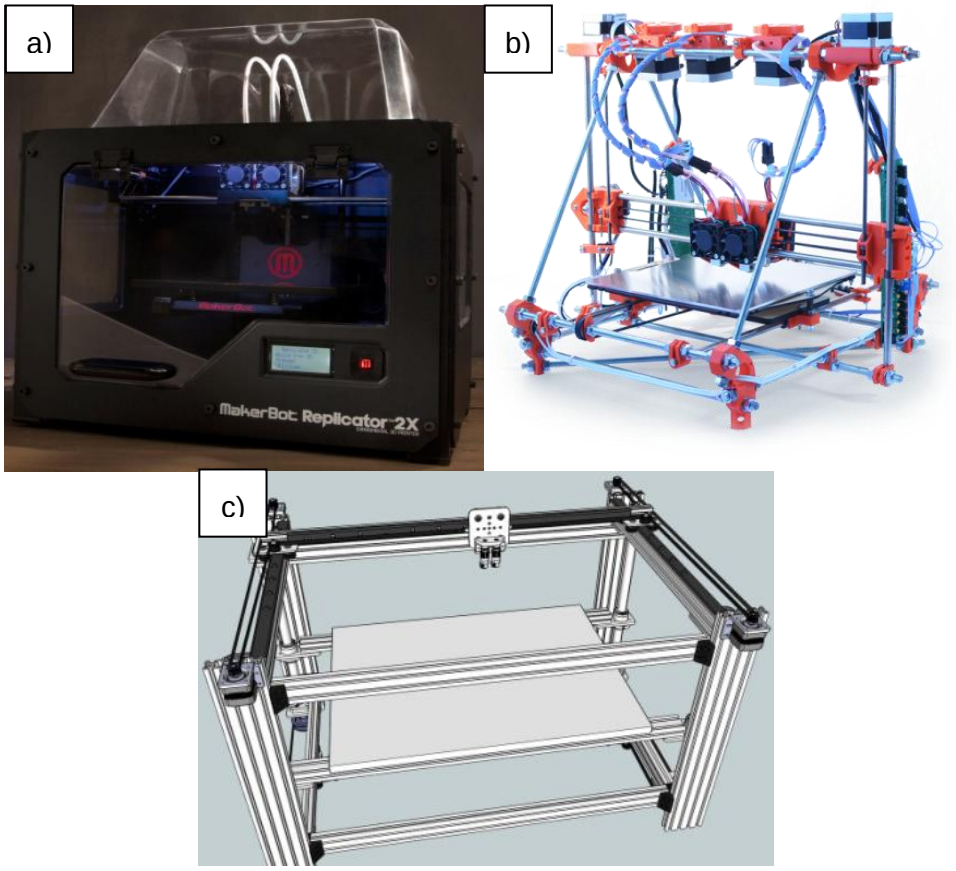

Figure 4: Cartesian coordinate 3D printers.
(a) Makerbot Replicator 2X[11] (b) RepRap Mendel Tricolor[12] (c) H-Bot based design[13].

2.1.2. SCARA

One of the newest entries into the mainstream RepRap project, the RepRap Morgan has been billed as a lower cost and easier to build alternative to the conventionally Cartesian RepRap printers[14] (Figure 5). An interim winner of the Gada Uplift prize[15], the Morgan design uses a coaxial drive system and arms in a parallelogram configuration for moving the hot end in the X and Y axes, and a vertical drive screw to move the bed in the Z axis. A Bowden configuration for the extruder system allows minimal weight on the end effecter further helping to reduce part complexity and weight.

Figure 5: RepRap Morgan[14].

2.1.3. Delta Robot

First designed for 3D printing by Johann C. Rocholl, the Rostock branch of the RepRap family uses a linear delta arm configuration[16] (Figure 6 a). This configuration uses three vertical towers with carriages that attach to the end effecter by two parallel rods with ball or U joints at each end, which constrains the effecter to a plane parallel to the build platform. Zero-backlash magnetic ball joints have also been employed to minimize the mechanical slop in the system[17], which can be detrimental to printer calibration, especially when multiple nozzles are used on the end effecter. The main advantages of this setup are that the parts for each arm are identical, simplifying the parts list, head positioning is rapid in all directions, and the build plate is stationary. Because the kinematics are more complex, involving more independent variables which require calibration[18], [19] (Figure 6 b), the system is very sensitive to minor defects in assembly and manufacture, and finding and fixing these defects can be difficult due to the complex geometry (see section 3.1.2 for more details on the kinematics). In addition, increased processing power requirements due to the more complex inverse kinematic relationships may result in lower print speeds on slower electronics, especially

in the case of complex details, but as more powerful control boards emerge this is becoming less of an issue.

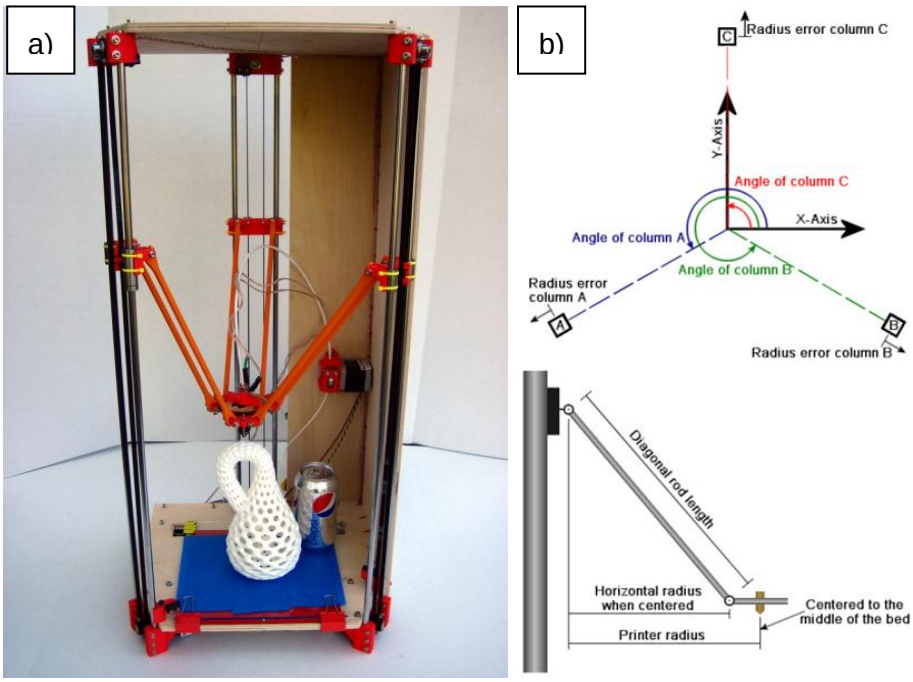

Figure 6: Rostock linear delta robot 3D printer[16].
a) Fully assembled Rostock printer b) Kinematic parameters for Rostock linear delta robot available in Repetier firmware[20].

2.2. Software and Electronic Control Systems

One of the most important aspects of FAM, especially from the perspective of the user, is the software that controls the printer. Creating a part using FAM requires a number of steps even before the printer begins to lay down the material(s) to produce the object. From the initial design, to plotting out the tool paths for the extruder to lay down material, to managing the print as it is occurring, there are a number of software systems needed to ensure that the final result is a high quality part which matches the needs of the user. Properly designing a part using 3D design software can save time and/or material during the printing stage. Using the proper slicing software settings will ensure that the part matches the required surface finish and strength, and prints properly. To visualize the tool paths to verify that there are no problems, and control the printer during the print requires an interface and control software commonly referred to as a host. Finally, to interpret the commands generated by the slicing software, and

convert them into control signals for the individual motors and heaters, a firmware embedded in the control board of the printer electronics is required.

2.2.1. 3D Design Software

Every 3D printed part begins as a 3D model generated by any one of a wide variety of design software available. While not always considered part of the additive manufacturing process, it is important to note a few aspects of 3D design which pertain specifically to FAM. Due to the extrusion-based nature of the deposition process, it is important not to have wall thicknesses less than the minimum extrusion width of your printer, and in fact thicknesses which work best are an integer multiple of extrusion width for walls less than four times this thickness. Sharp points also tend to produce artifacts in the final print and if possible should be rounded to a radius either one or two times the minimum extrusion width or clipped off at this thickness (Figure 7)[21]. Another consideration is overhangs. While many printers are capable of printing excellent support structures, sometimes it is desirable to design the part in such a way that it does not need these to improve surface finish or print time and minimize clean up. Parts can also be cut to circumvent the necessity of support, to reduce the amount of support needed, or to allow printing of parts larger than the build volume of the printer, which are then glued together after printing. Orienting a part properly can also have a huge impact on the amount of support needed, sometimes allowing complex parts to print with no support at all in the proper orientation[22]. Finally, taking into account the anisotropy of the final 3D printed part can be very important if the part will be used as the end product rather than as a prototype[23]. Generally, layer adhesion is weaker when compared to the layer's strength. This means that the part is weakest and most prone to breakage due to forces along the vertical axis (orthogonal to the printed layers) as a result of layer delamination. Paying attention to each of these aspects from an early design standpoint will help to produce high quality parts through FAM. The final step in part generation is to export the part to a compatible file format for the printer software. The de-facto standard for single material parts is currently the .stl format[2], and multiple .stl files can be combined together into an .amf file for multi-material/color printing. If there are problems with the exported model, mesh editing software such as Meshlab[24] or Netfabb[25] is used to repair any defects in the final .stl files. Mesh repair is especially

useful for files generated by 3D scanners or other reverse engineering techniques which create point clouds or can leave holes in the model[26].

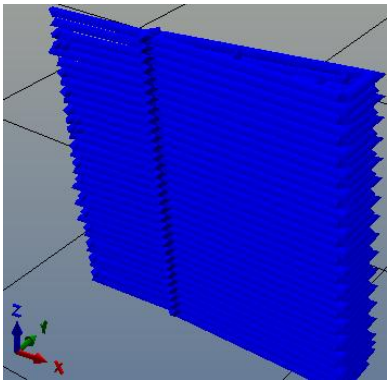

Figure 7: Slicing artifacts due to sharp angles.
A 10° wedge coming to a point was sliced using Slic3r assuming a 0.42mm extrusion width at 0.3mm layer height. Due to the quantization of paths used to generate the part, artifacts appear when the part dimensions approach line width dimensions.

2.2.2. Slicing Software

One of the most important pieces of software used during part generation is the program that generates the g-code to control the hardware. To deposit the material into the desired final shape accurately, the object is first sliced into thin cross sections, and then a tool path is generated to create each cross section. During this process, there are many things to take into consideration to ensure that the layer is successfully deposited. To make sure that the outside of the part is smooth, one or more perimeters are laid down to outline the shape of the layer. Next solid horizontal surfaces such as the top and bottom are detected and filled in. Depending on the infill settings, the part may be hollow, partially hollow, or solid. Different infill patterns are available, and one open source slicer program called Slic3r[27] has the following available: rectilinear, linear, concentric, hexagonal, Hilbert Curve, Archimedean Chords, and Octagram Spiral (Table 1). Infill allows the part to be partially hollow to save material and build time, while still maintaining a high structural integrity and allowing internal support for any flat top layers. Different infill patterns provide different levels of structural integrity as well as advantages to print speed and material usage. If there are parts of the layer which overhang beyond the previous layer, this necessitates the generation of support material to ensure that the perimeters will not sag. Additional perimeters or other internal

reinforcements can also be added to certain areas to ensure that there are no gaps in the final part due to perimeters of adjacent layers not completely overlapping.

A number of optimizations to layer and path generation algorithms have been suggested to improve the quality of the printed parts. Kulkarni and Dutta[28] proposed a method for determining optimum layer height of different regions in the print to decrease the surface roughness of the final part (Figure 8). It has also been proposed by Guduri et al.[29] and others, that slicing from the original CAD file will produce more accurate results as the process of exporting the design to the current standard of .stl files results in triangular approximations of the actual part geometry which can introduce errors into the final printed part. This also has the added advantage of integrating the design and slicing software into one package, reducing the number of different programs needed to prepare the designed part for printing. Ma et al.[30] combined these two processes and further improved print time by keeping infill at the maximum layer height, while adaptively changing perimeter layer heights to optimize for exterior print quality. One other issue with using tessellated file formats such as .stl is that the output .stl can sometimes greatly exceed the file size of the input CAD file, especially for complex curved shapes. An extreme case cited by Jamieson and Hacker was a 55Mb .stl file generated by a 4.5byte CAD file[31]. Large files like this can take up to eight hours to slice, whereas directly slicing the CAD data is much faster and less prone to artifacts due to the conversion to .stl. They introduce the Cranfield approach, which uses direct slicing in the CAD software Parasolid, to generate layer slices, with optional adaptive layer height optimization. As AM proliferates, the integration of design and slicing software will become more common, especially as 3D printers penetrate the home market and users expect fully integrated software suites.

Table 1: Different infill styles available in Slic3r.

Infill style	Cutaway	Single Layer	Filament used (mm)	Printed volume (cm^3)	Estimated print time
Rectilinear	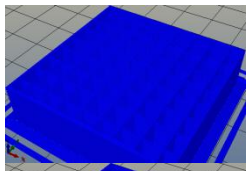	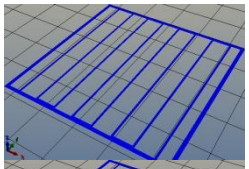	4944.6	11.9	1h:30m:55s
Linear	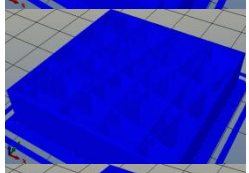	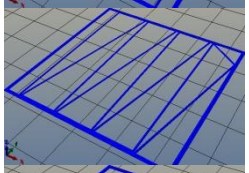	5105.6	12.3	1h:30m:58s
Concentric	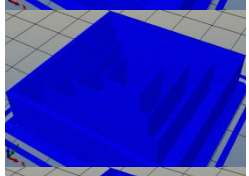	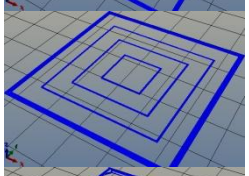	5204.4	12.5	1h:30m:54s
Honeycomb	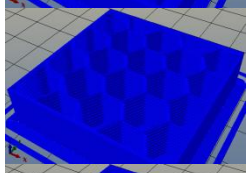	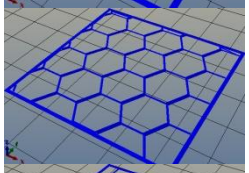	5490.6	13.2	1h:31m:32s
Hilbert Curve	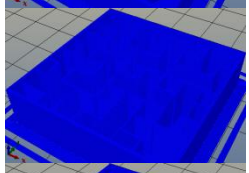	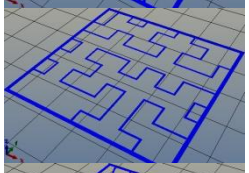	4592.4	11.0	1h:32m:1s
Archimedean Chords	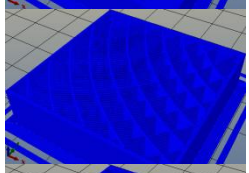	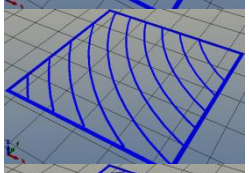	4725.3	11.4	1h:31m:45s
Octagram Spiral	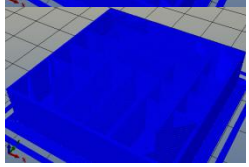	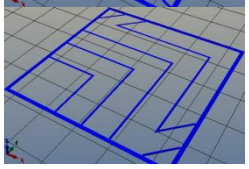	4086.6	9.8	1h:31m:22s

Each example was created from the same 4cm cube with a 0.3mm layer height and 10% infill with 2 perimeters and 3 solid bottom and top layers. A cross section was taken ~1/3 of the way from the bottom to show the long term structure of the infill, and a single layer, showing the path taken each layer, was also taken. Single layer patterns rotate on alternating layers to produce the final long-term structure, and increase the structural integrity of the part. Filament was set to 1.75mm dia.

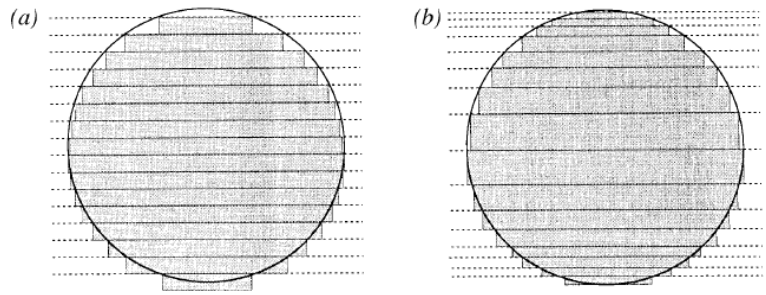

Figure 8: Adaptive Slicing for efficient layer height calculation.
(a) Uniform slicing and (b) adaptive slicing. (from Lee and Choi)[32].

2.2.3. Printer Host Software

The printer host software plays an important role in setup, maintenance and calibration of the printer, and in most cases is the main software visible to the user. The main role of the host is to send the compiled g-code from the slicer software to the printer, either line by line as the printer is running, or to the onboard memory of the printer. For printers with minimal or no integrated human interface, the host also acts as a remote interface for manually controlling the printer for such things as filament changes, purging and calibration. Host software may also include path visualization algorithms, to perform sanity checks on the output prior to printing, and gcode editing capabilities, providing manual post processing such as entering commands to pause at certain heights for a filament change to produce layer selective colored parts[33]. The host software may also include slicer software either internally or by calling it as a subprogram, reducing the number of programs the user needs to interact with to produce the finished part.

While commercial printers such as the Stratasys FDM systems, Makerbot Replicator and 3D Systems' Cube tend to come with their own unified software that integrates slicing and host into a single package, many of the open source printers derived from the RepRap project rely on open source packages. Repetier Host is one commonly used open source host package which integrates both Slic3r and Cura and provides the option for manufacturers of 3D printers to customize the software to work out of the box for their printers[20]. Some open source host/slicer software such as Cura are being developed by manufacturers of open source hardware 3D printers such as Ultimaker[34]. Many of the lower cost 3D printers have minimal if any interface

features; therefore, it is desirable to provide a networkable printer host, which can be accessed via an online interface. Octoprint is one such web-based host, and provides a robust web-enabled host capable of running on minimal hardware such as a Raspberry Pi[35].

2.2.4. Firmware and Printer Electronics

At the heart of the 3D printer lies the onboard computer, which interprets the G-Code commands generated by the slicer, and converts them into the movements of the 3D printer. As an embedded system with minimal computational requirements, a low cost microcontroller with preconfigured firmware generally powers it. For commercial systems, this software is generally proprietary and difficult to modify, and thus prevents easy user modification of the systems. In contrast to the commercial systems, which have fixed mechanical parameters, the RepRap project had to deal with the flexibility of users with different mechanical setups, leading to much more general-purpose firmware, which can be customized to fit any hardware configuration. With the introduction of the RepRap program, based on Arduino microcontrollers, and the release of open source firmware code, it became much easier for users to experiment with settings and modifications, allowing the users of the hardware to begin to modify and add additional features to their printers. As the RepRap project progressed, and newer printer designs and electronics were released, a number of different forks and reworks of the firmware have been released providing specific functionality, or supporting newer platforms such as 32bit microcontrollers based on the new Arduino Due[36], [37]. As printers begin to target home users, and low cost embedded electronics increase in computing capacity, many of the host software features are being built into the onboard electronics of the printer, providing Bluetooth and Wifi connectivity and simple interfaces for tablets and phones[38], [39].

2.3. Material Deposition (Extruder) System

The material deposition system in a filament-based 3D printer can be broken down into two subsystems: the hot end or liquefier, and the cold end, which receives the

filament feedstock and drives it into the hot end. Among the components of a FAM system, the material deposition system is the most likely to have problems, and as such there have been many designs attempting to increase the reliability and functionality of this system. Frequently the extruder system is also the limiting factor for increases in print speed, so understanding how to maximize extrusion speed is critical to increasing the print speed and overall performance of the FAM system.

2.3.1. Material Driver (Cold End)

The cold end is made up of a motor which rotates a knurled, hobbed or toothed pinch wheel against a bearing or pressure plate. There are three major designs that are commonly used: geared, direct, and parallel or screw drive. The geared extruder uses a small gear on the motor to drive a larger gear on a hobbed bolt, which is positioned perpendicular to the filament path, to drive the filament, taking advantage of the mechanical advantage to increase torque, as well as minimize the step effects of the stepper motors commonly used (Figure 9a). Many geared extruder designs have been released as part of the RepRap project, and many of these use 3D printed parts and homemade hobbed bolts, making them popular for use on homebrew printers. Direct drive extruders take advantage of high torque stepper motors to create a smaller footprint extruder by foregoing the gearing and directly attaching a hobbed nut onto the motor shaft (Figure 9b). Without the gear reduction, step size becomes an issue so proper calibration of the stepper microstepping is important. Use of a pre-geared stepper motor can alleviate this, and provide the benefits of a geared extruder, with only a small increase of the footprint of a direct drive extruder and a moderate increase in cost. The parallel drive extruder uses a worm gear positioned parallel to the filament such that as it spins, the filament is driven through the system (Figure 9c and Figure 10). The advantage of this system is that multiple teeth are in contact with the filament, reducing the chances of slippage, and the mechanical advantage provided by the worm gear allows the use of a lower powered motor. This design was used as one of the early prototypes in the RepRap Darwin and while successful, it was found to introduce a twist into the filament, which needed to be accommodated through a rotating filament holder[40]. The material properties of the filament used can also affect the design of the extruder, especially as new materials with lower elastic modulus have been introduced.

To minimize the chance of buckling, the driver needs to constrain the filament after the drive gear to ensure that the required extrusion force does not exceed the critical buckling load of the filament in the unsupported length (Equation 1). This has led to a number of designs for parts to upgrade existing extruder assemblies that can be manufactured by the printer itself, as well as off the shelf designs sold by printer manufacturers to improve filament support[41], [42].

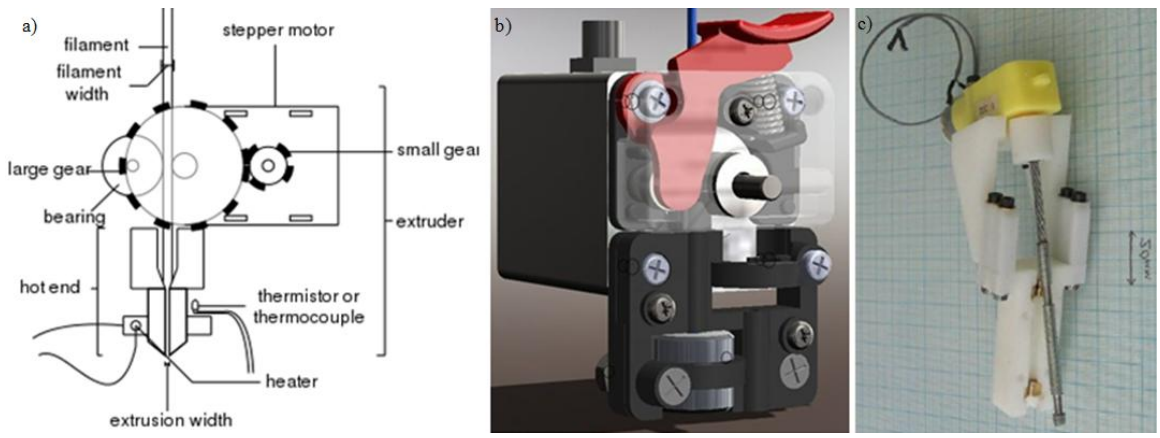

Figure 9: RepRap printer cold ends.
a)Geared "Wades like" extruder with hot end[43] b)SeeMeCNC EZStruder direct drive extruder shown with attached Bowden adaptor and filament guide[44] c)Screw drive extruder from early RepRap prototype, disassembled to show screw-based material driver[45].

$$F = \frac{\pi^2 EI}{(KL)^2}$$

Equation 1: Critical Load of a Column in Axial Loading.
E=elastic modulus, I=area moment of inertia (= $\frac{\pi}{2}\boldsymbol{r^4}$ for a cylindrical filament), K=column effective length factor (=1 for both ends free to rotate, =0.5 for both ends fixed), and L=Length.

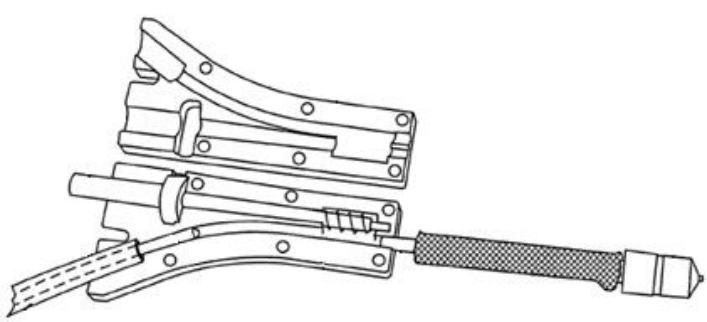

Figure 10: Integrated filament delivery and extrusion system for consumable system[46].

To reduce the weight and size of the printer head, some designs, such as the the RepRap Morgan (Figure 5) and Rostock (Figure 6), separate the material drive from the liquefier by using a flexible Bowden cable. This relegates the heavy extruder motor to a hard mount on the printer chassis, while the lightweight nozzle system remains on the head, reducing the load on the positioning motors[47]. Commercial systems have also developed smaller, lighter extrusion systems (Figure 10), and integrated them into the consumable filament reel. This has the added benefit of replacing the nozzle each time the feedstock is changed, reducing the serviceable parts and allowing replacement of the filament canister should a nozzle blockage occur[46].

Multi-nozzle FAM systems provide the capability to use soluble support systems, as well as to produce multi color and multi material parts. A number of different material driver configurations have been used in multi nozzle systems, with the simplest comprised of two or more extruder assemblies attached directly to the print head, with a known offset used to switch between them (Figure 4a). While this works for two direct drive extruders, the added weight and space requirements of more and/or larger extruders creates added work for the mechanical systems which move the print head and will require larger head travel to accommodate the large offsets. Multiple extruders connected via Bowden cables, such as in the RepRapPro tricolor Mendel (Figure 4b), allows the nozzles to be spaced closer together and places less mass on the printer head. Another way to reduce the weight, as well as the number of motors needed, is to use a single drive shaft with a switching mechanism to select between multiple filament paths. Stratasys patent US20070228590 A1 (Figure 11a) describes an implementation of a dual extruder using a single drive motor and a switching system to rotate the desired filament into contact with the drive shaft. As an added benefit of this design, the out of service nozzle is lifted up slightly, reducing the risk of it crashing into the part during production[48]. Another approach originally proposed by Thingiverse user Fritzgutten, and since improved upon by others, uses a cam based system to select from multiple filament paths leading to separate nozzles[49], [50] (Figure 11c). RepRap users have also suggested a turret style extruder with multiple nozzles, allowing separate colors or materials to be selected by indexing the desired material path to the drive shaft[51], [52] (Figure 11b). A major advantage of this approach is that the active nozzle will always be in the same position, removing the requirement for offsets that add to the required

positioning volume for a given build volume. Unfortunately, with the low precision of 3D printed parts, achieving reliable repositioning of the nozzles may prove a challenge. The author has suggested an improvement to the design, wherein a Geneva mechanism is used for nozzle indexing, and spring loaded nozzles are pushed down into a guide bracket by the locking portion of the Geneva gear. This would provide the added benefit of effectively raising inactive nozzles from the build plane, preventing them from fouling the part. A nozzle wiping/capping mechanism could also be integrated into the park positions of the inactive nozzles, preventing them from oozing while not in use, but kept hot for rapid material switching[53].

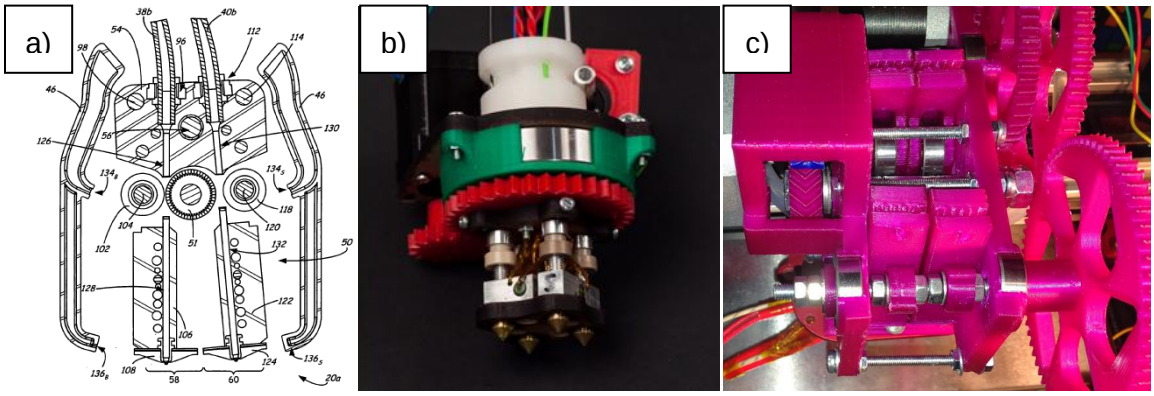

Figure 11: Multi nozzle single drive motor designs.
a)Dual nozzle extruder with single filament drive motor[48] b)Quad nozzle turret with indexing extruder[52] c)Cam based quad filament driver[50].

2.3.2. Liquifier (Hot End)

To deposit thermoplastic materials in FAM, the filament is extruded through a heated nozzle by pressure applied to the filament by the cold end of the extruder assembly, with the unmelted portion of the filament serving as a continuous plunger. The final nozzle diameter determines the minimum width of the extruded path, which determines the minimum feature size on the build plane. The geometry of the filament path through the heated portion of the nozzle is very important to the performance of the extruder; especially considering the limitations of the materials used, and will affect the print speed, reliability of the system, and the print quality. Since most of the materials used in FAM are soft polymers with smooth surfaces, and the material driver must bite into the material to push it into the liquefier, there is a limit to the force it can apply before the material begins to fail and the driver begins to strip material off of the filament rather

than move it. If the extruder gear does not slip, failure can also occur by buckling of the filament due to the back pressure being greater than the critical buckling load of the material[54]. Filament diameter has a key effect as smaller diameter filament will be able to achieve higher pressure using less extruder force and will accommodate sharper curves in the filament delivery path, but will be more prone to buckling if unsupported due to its lower area moment of inertia (Equation 1). Early RepRap liquifiers were designed to work with 3mm filament as plastic welding rod in this diameter was readily available[55]. As designs matured and material manufacturers began offering filament for 3D printers specifically, 1.75mm diameter filament became more common and has become the de-facto standard.

A good measure of the extrusion characteristics of the liquefier is the backpressure generated during extrusion at a fixed rate, since this is in direct opposition to the force being applied on the filament by the material driver. Modeling of the fluid dynamics in the liquefier has shown that minimizing the melt zone length reduces the back pressure in the system, resulting in lower torque requirements for the extruder motor, or higher material extrusion rates for a given pressure which translates to faster print speeds[45], [56], [57]. Early liquefier designs for Stratasys FDM systems used a curved filament path with a long melt zone (Figure 12a). While this system worked well in early models, the print speed was very slow and later models switched to an improved design using a much shorter straight filament path (Figure 12b)[57]. Similarly, RepRap hotends have progressed rapidly through many iterations of design[58], beginning with a simple PTFE heatbreak and brass nozzle heated by a length of nichrome heater wire wrapped around it[45]. The heatbreak was identified early on as a critical part of the hotend design, allowing the use of low melting temperature (T_m) printed polymer parts to be used for the cold end, and preventing the filament from softening in the material driver. High T_m polymers, such as PTFE and PEEK, were initially chosen due to their low thermal conductivity and easy machinability, allowing home users to produce their own hotends without access to expensive metal working equipment. This worked well with the low T_m polymer feedstocks used in early RepRap based printers, but as higher T_m polymers were introduced, and performance increases were sought, a gradual shift to all-metal designs has occurred. By using a thin-walled stainless steel tube as a

heatbreak between the hot nozzle and an actively cooled heatsink, the operating temperatures can be increased, allowing the use of higher T_m polymer feedstock.

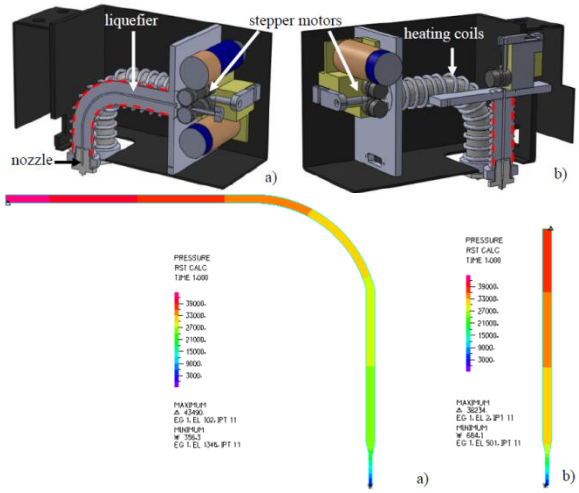

Figure 12: Early Stratasys liquifier designs demonstrating the improvement in extrusion pressure when switching to a shorter and more direct melt path.

a)Early model curved path and accompanying pressure gradient model b)Improved straight design with shorter heated region and lower extrusion pressure[57].

The nozzle tip design also offers opportunity for innovation and performance improvements. Because the narrow orifice diameter results in a constricted flow channel at the tip, which contributes the majority of the backpressure to the system (Figure 12 b) because of the inverse relationship between the pressure drop and d^4 (Equation 2), minimizing the length of this section is critical to reducing extrusion force, especially for smaller orifice nozzles. E3D has recently upgraded their nozzle design to use a hierarchical structure of decreasing diameter channels in their smaller orifice nozzles, providing a more gradual change in diameter and reducing the smallest diameter channel length substantially (Figure 13), which has resulted in substantially decreased backpressure in their systems[59]. Another interesting innovation in nozzle tip design is the dual path-width design patented by Stratasys (Figure 14). This design uses an annular groove surrounding the tip to allow two path-widths of extrusions to be produced, while still maintaining good line edge roughness of the paths. This allows smaller paths to be used on the perimeter of the part, allowing smaller features to be produced, while allowing larger paths to be used in the infill of the part, which increases the strength of the part.

$$\Delta P = \frac{128\mu L Q}{\pi d^4}$$

Equation 2: Hagen Poiseuille equation for viscous flow in a cylindrical pipe.
μ is the viscosity of the fluid, ΔP is the pressure drop, L is the length, Q is the flow, and d is the diameter.

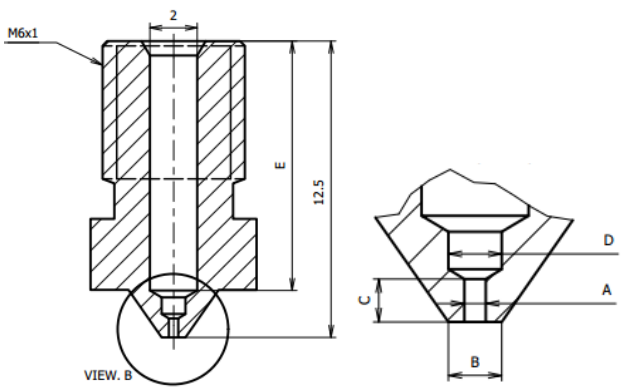

NOZZLE GEOMETRIES				
A	B	C	D	E
0.25	0.63	0.50	1.0	10.8
0.30	0.75	0.60	1.0	10.7
0.35	0.88	0.70	1.0	10.6
0.40	1.00	0.80	1.5	10.5
0.60	1.50	1.20	2.0	N/A
0.80	2.00	1.60	2.0	N/A

Figure 13: Hierarchical design in E3D nozzles[60].

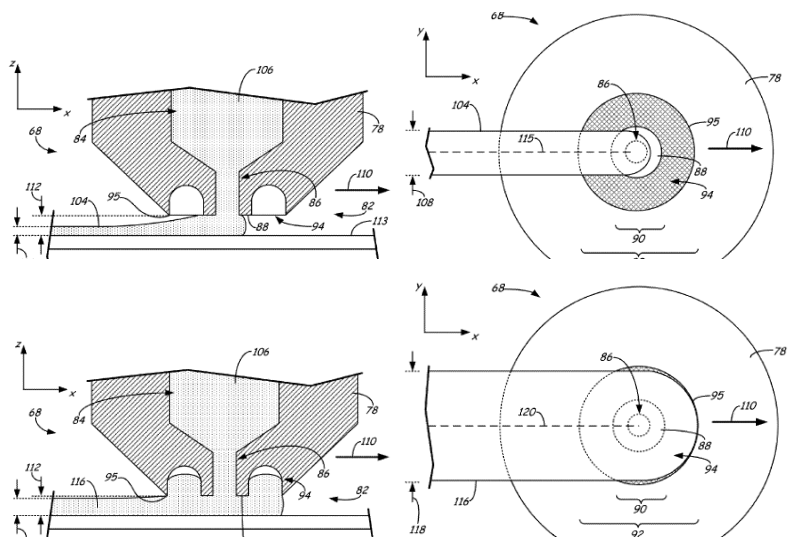

Figure 14: Dual path-width print nozzle[61].

Special hotend designs have also been produced which allow multiple materials to be extruded from a single nozzle, circumventing the need for careful nozzle alignment and calibration for multi-material and multi-color prints, as well as allowing mixing of different colors.

2.4. Accessories

In addition to the main systems required for printing, a number of optional accessories may be present or added by the user to improve the printing experience and/or performance of the machine. Ensuring proper adhesion of the part to the bed is critical, so various materials and treatments have been developed to promote optimum part adhesion. Heating the build chamber can help reduce warping of the part during the print to increase part fidelity. Cooling fans are also important to manage heat buildup within both the machine and the part. Ensuring that the bed is level relative to the motion of the print head is critical to first layer adhesion, and part adhesion to the print bed overall and as such a number of auto calibration methods have been developed. Finally, ensuring smooth feeding of the feedstock material through filament management systems helps prevents print failure from interruptions to the free flow of material.

2.4.1. Printer Bed

Depending on what material(s) the printer is using, the printer bed must be compatible to ensure proper adhesion and prevent premature delamination, leading to edge warping and potentially print failure. Conversely, the print must be removed after printing, so the adhesion must either be controllable, usually through the application of heat, or weak enough that the part can be removed relatively easily. A number of different materials have been used, and the optimum material is dependent on what material is being printed and whether or not the printer has a heated bed and/or build chamber. In addition, some users opt for a sheet of plain window or borosilicate glass, then coat this with adhesion promoters such as PVA or hair spray.

2.4.2. Build Chamber

In addition to providing a safety feature to prevent accidental harm to the user and/or the machine, an enclosed build chamber also provides protection from thermal gradients which can exacerbate warping during the print. By providing an enclosed heated environment, the build chamber can keep the material already deposited at or above the glass transition temperature of the material, therefore allowing creep in the

material to compensate for residual stresses due to thermal contraction. Other features of the build chamber can also include a nozzle wiper, to help clean the nozzle before starting the print, which is generally coupled with a purge area which is used to prime the nozzle prior to the start of a print, and in multi-nozzle systems when switching between nozzles.

2.4.3. Cooling Systems

Due to the high temperatures used in FAM, thermal management is critical to ensuring high quality part production. While the deposition nozzle needs to remain at high temperatures to ensure proper material flow, the material delivery path needs to be kept cool to prevent deformation of the filament, which would result in a jam and subsequent interruption to material deposition. Creating a sharp thermal transition between the heated nozzle and the rest of the filament path is critical to both preventing jams and reducing the pressure needed to extrude the material[57]. Active cooling of the system above the nozzle has been employed successfully in a number of designs, and popular designs include high surface area heat sinks and cooling fans, or a water-cooled cooling block such as those in E3D's all-metal hotends[62]. After deposition of the material, it is important that the material rapidly cool below its glass transition temperature to prevent any slumping of the part, especially while printing overhangs or bridges. Fan ducts are commonly used to direct air from a cooling fan attached to the print head assembly to the area directly surrounding the nozzle[63]. With the great diversity of printers and hotends now on the market, many users have taken to designing custom fan ducts to fit their configurations, demonstrated by a quick search on Thingiverse providing over 900 results for "fan duct"[64]. With the capabilities to modify the firmware and hardware of open source printers, comes the ability to exceed their recommended operating specifications. To compensate for over driving stepper motors or electronics, it is important to install cooling systems onto these systems to prevent damage.

2.4.4. Filament Management

To ensure that there are no interruptions to the feedstock material, a number of different systems have been devised to ensure that filament is delivered reliably to the extruder system. The simplest form of filament management is a spool holder which holds a reel of filament above the extruder and relies on the natural flexibility of the material to accommodate motion of the extruder assembly. While this works well in open systems such as the RepRap Mendel, as the filament path becomes more constrained, and to improve the aesthetics of the system, filament guides such as the PTFE tubes in the Makerbot Replicator (Figure 4) can be used to route the filament from the spool. These also have the advantage of providing mechanical support to brittle filaments such as PLA, preventing kinks that can result in filament breakage and print failure. Many of the plastics used for FAM are substantially hygroscopic, or even water soluble in the case of PVA support material. Absorbed moisture in the filament can adversely affect the print quality due to rapid vaporization during printing, creating bubbles in the part. To prevent this, filament is normally sold in sealed bags with desiccant. While this prevents absorption prior to use, after filament is loaded onto the printer many printers leave the reel exposed to ambient conditions. A number of ad-hoc solutions have been developed by the RepRap community, and some printer manufacturers sell filament in pre-packaged airtight containers which interface directly to their machines[65]. While the reliability of the feedstock delivery system is important, the filament reel represents a finite resource, and at some point, the end of the filament will be reached. When this occurs, it is important for the machine to cease printing and notify the user that a replacement needs to be inserted to continue printing. In commercial systems this functionality is sometimes built into the proprietary filament cartridges used by the printer, while in RepRap based printers this functionality has been added by users to some firmwares to work with custom sensors mounted in the filament delivery path [66], [67].

Chapter 3.
Experimental Equipment, Modifications, and Procedures

For the successful completion of this work, several systems were needed to enable the production and printing of the metal alloy filament in combination with standard thermoplastic filaments. A RepRap FFF 3D printer was chosen due to the ease of modification, and open source nature that provides a community of other makers working with, and providing support and upgrades on, similar machines. Several printer systems were investigated, and after careful consideration of the available options, the Rostock Max kit from SeeMeCNC was purchased. In addition to the printing platform, it was decided early on that multiple extrusion systems would be used to enable multi-material 3D printing. In addition to the printer system, a filament fabrication system was needed. Initially a Filastruder filament extruder was purchased for the creation of custom filaments; however, as the metal alloy was not compatible with the system, a different approach was taken to create experimental samples for testing using a casting method. This chapter provides a record of the equipment used during this work, as well as any modifications made or analysis performed of the systems used. It also covers the procedures used to produce the metal alloy filament.

3.1. Rostock Max

The Rostock Max platform was selected for this project because it offered a good balance between precision and accuracy, and upgradeability, as well as because it had the option of coming with a dual or triple extrusion system which would enable automatic co-deposition of different materials. In addition, the open frame of the design allows easy access to the parts for modification. This printer uses a parallel upright linear delta configuration (see section 3.1.2 for the basic kinematics), with the three actuator carriages controlled by stepper motor driven belts. The body is composed of laser cut

melamine coated MDF, with extruded t-slot aluminum rods serving as both the rails for the carriages and the vertical structural towers. The printable volume is cylindrical, with a diameter of 280mm and a height of 375mm.

3.1.1. Configuration and Modifications

Initially, the system was assembled with a single extruder for setup and calibration. In this configuration the nozzle was positioned very close to, and at the center of, the end effector platform. When the system was upgraded with a dual extruder configuration, it was discovered that a small amount of play in the universal joints used on the arms was resulting in the end effector not remaining level as it moved away from the center of the build area (Figure 15). Because the nozzles were no longer at the center of the end effector, this caused the extruder nozzles to deviate from the build plane, resulting in the lower nozzle binding on the material being printed by the higher nozzle. To remove this play, a set of carbon fiber rods with zero-backlash ball joints was purchased from tricklaser[68].

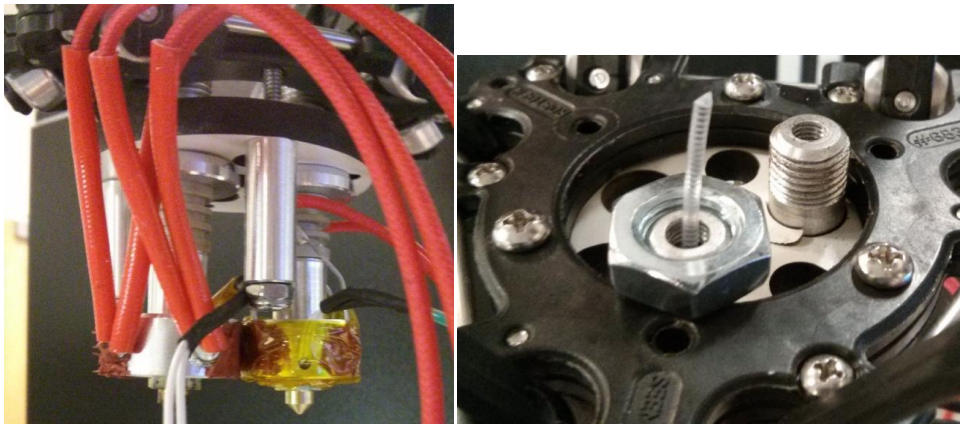

Figure 15: Dual nozzle configuration of the Rostock Max.
The large vertical displacement from the end effector platform greatly exacerbated minute rotations of the platform due to tolerances in the arms.

Kraken Quad Extrusion System

Shortly after the printer was purchased, E3D-Online released the Kraken quad-extruder system, which could be integrated onto the Rostock Max platform, and was purchased to expand the material printing capabilities to 4 simultaneous deposition

systems. This system is composed of four identical hot-end assemblies, consisting of a nozzle, a heater block, and a stainless steel heat break. The smooth shaft of the heat breaks slide into a water-cooled aluminum heat sink, and can be independently adjusted in height via set screws. PTFE tubes serve as Bowden delivery tubes from the pinch-wheel drivers mounted on the sides and top of the printer. In addition to increasing the number of material deposition systems, the kraken also enables the use of higher melting point thermoplastics, as there are no PTFE or PEEK components in the hot-end which cannot withstand temperatures above ~250°C. The design also reduces the melt transition zone length, which improves extrusion characteristics (see section 2.3.2).

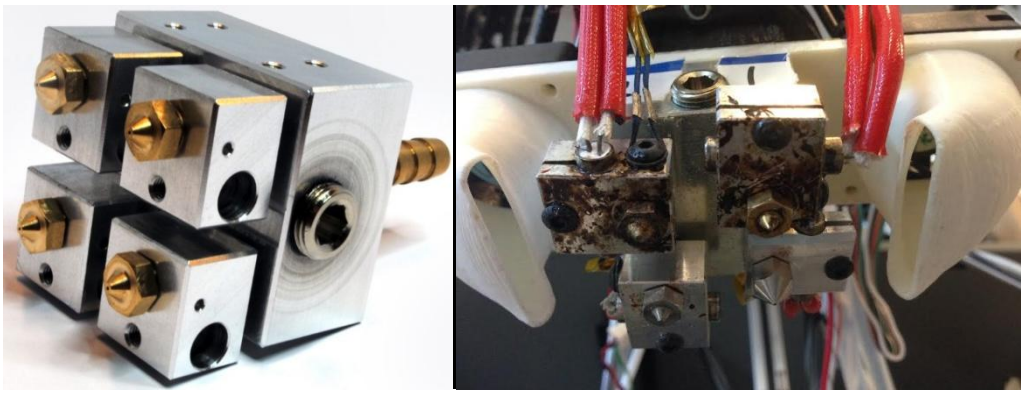

Figure 16: Kraken quad nozzle system.
The system includes 4 individually configurable nozzles, mounted into a solid aluminum water-cooled heat-sink (left)[62]. The system as assembled on the Rostock Max with part-cooling ducts (right).

Printer Control Board and Software

The motherboard included in the Rostock Max kit was a RepRap Arduino-compatible Mother Board (RAMBo)[69]. This board was designed to provide a single, integrated control board for 3D printer systems based on the Atmel ATMega2560 8-bit microcontroller. It features five integrated stepper drivers, 6 PWM DC outputs for hotends or other accessories, and supports min and max end stops as well as up to four thermistors. When the number of extruders was increased to four, the RAMBo was deemed insufficient to power the printer, so a new motherboard was installed. The board chosen was the Azteeg X3 Pro, which supports up to eight stepper drivers using standard pololu-style breakout boards, and 8 PWM outputs for hotends or other accessories. To accommodate the increase in extruder systems, as well as the other

modifications to the printer, the firmware had to be upgraded. There are several different branches of RepRap compatible firmware available, but the one chosen was Repetier[20] due to the ease of customization, the excellent documentation, and the authors prior familiarity. In addition to the firmware, to accommodate the use of multiple nozzles and materials in the printed parts, two different slicer softwares were evaluated: Cura and Slic3r. It was found that while Cura was simpler to use, and the wipe and prime feature was useful for multi-material printing, the overall increase in user configurable parameters in Slic3r provided more controllable results, especially when different materials were used.

Custom Nozzle Fabrication

Because the metal alloy developed erodes the standard brass nozzles used in the extruder system, several different custom nozzle materials were investigated. While a set of stainless steel nozzles was purchased from E3D, the remaining materials of interest were not available, and as such had to be custom made. Because the design of the E3D extruder is open source, the design documents were available, and compatible nozzles could be produced in the metal shop at SFU (see Appendix C for schematic). Aluminum nozzles were produced from both 2011 and 6061 alloys. Hard Coat anodizing was performed on the fabricated nozzles by Spectral Finishing. The electroless nickel coated nozzles were purchased from P3D, but were not compatible with the stock E3D heater blocks, so a custom heater block was created which allowed their use with the extrusion system (Appendix D).

3.1.2. Delta Robot Kinematics

While working with the Rostock Max, it was found that properly calibrating the system was critical to getting reliable prints. To better understand how to troubleshoot problems with calibration, a basic analysis of the kinematics of the system was performed, based on previous analysis of a similar system[70]. To begin analyzing the system, the system was first decomposed into its simplest kinematic elements. The complete system consists of three identical kinematic chains, actuated along parallel vertical towers, and connected to a central end effector by identical parallel rods (Figure 17a). Each arm assembly consists of a vertically actuated carriage with two identical

rods with universal and/or ball joints at each end (Figure 17b). By examining this setup, it can be seen that the position of the end effector can be modeled by three rigid rods with one end of each constrained to a vertical axis, and the other end connected to the two other rods' non-constrained ends. This virtual model can then be easily analyzed and important kinematic parameters' optimized values extracted.

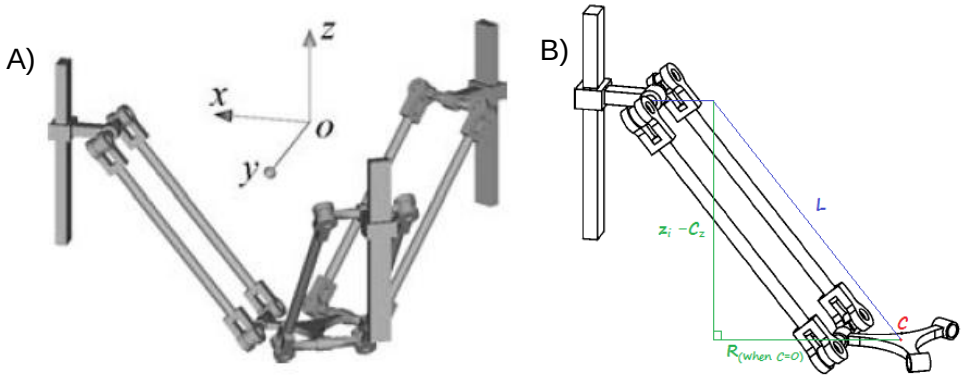

Figure 17: 3D render of the complete PULD system and diagram of a single arm.

A) Complete system B) Single arm with kinematic variables labeled. (Modified from Liu[70])

3D Model and Variable Definitions

To visualize the movement and kinematic variables of the system, a 3D model of the simplified system was created (Figure 18). The three actuation-axes, represented by large rods, are situated on a circle of radius R around the origin **O**, with the first on the X_0-axis, and the others at angles θ_2 and θ_3 around the Z_0 axis from the first. The intersection of the arms, of length L, with the actuation axes are $\mathbf{P}_i$ (i=1,2,3), and the point of connection of the opposite ends is **C** (Table 2).

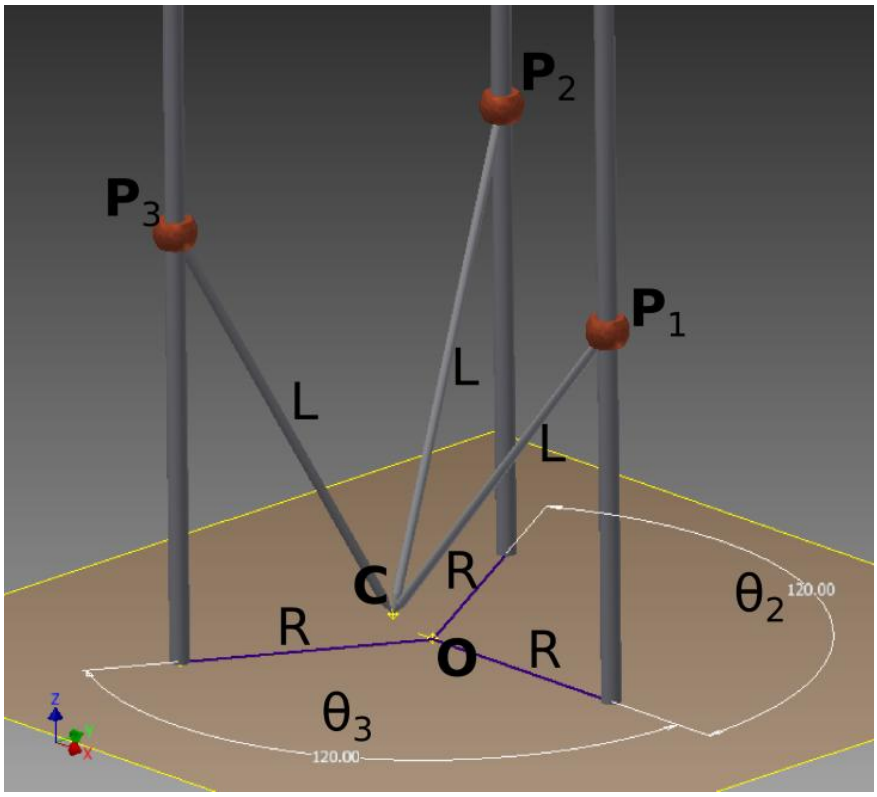

Figure 18: Render of the simplified kinematic system.

Table 2: Kinematic variable definitions

Variable	Definition
L	Arm length from ball joints on linear actuator to ball joints on carriage (all arms equivalent for this analysis)
R	Radius of circle contacting all 3 virtual actuation axis in simplified model (Also the length of the projection of the arm on the X_0Y_0 plane when the end effector is at the origin)
θ_i	Angle from the X_0 axis to the line connecting O_0 to the origin of the axis of actuation of the ith vertical linear actuator (held constant at [0,2π/3,4π/3] for this analysis)
C	Vector position of the end effector in the build space $(x,y,z)^T$
$\mathbf{P_i}$	Vector position of the ith linear actuator $(x_i,y_i,z_i)^T$
$\mathbf{z_i}$	Vertical position of the ith linear actuator

Inverse Kinematics Problem

To derive the inverse kinematics of the simplified system, each variable was generalized for use in matrices, with *i* representing the tower in question. Given that the rods are rigid, the distance between the end effector position and the position of actuator I is

$$\left|\left|\boldsymbol{P_i} - \boldsymbol{C}\right|\right| = \boldsymbol{L}, \ \ (\boldsymbol{i} = \mathbf{1}, \mathbf{2}, \mathbf{3}) \tag{1}$$

Expanding and rearranging leads to

$$(\boldsymbol{x} - \boldsymbol{x_i})^2 + (\boldsymbol{y} - \boldsymbol{y_i})^2 + (\boldsymbol{z} - \boldsymbol{z_i})^2 = \boldsymbol{L}^2, \ \ (\boldsymbol{i} = \mathbf{1}, \mathbf{2}, \mathbf{3}) \tag{2}$$

Substituting in the constant values of $\mathbf{P_i}$ as a function of R yields

$$(\boldsymbol{x} - \boldsymbol{Rcos}(\boldsymbol{\theta_i}))^2 + (\boldsymbol{y} - \boldsymbol{Rsin}(\boldsymbol{\theta_i}))^2 + (\boldsymbol{z} - \boldsymbol{z_i})^2 = \boldsymbol{L}^2, \ \ (\boldsymbol{i} = \mathbf{1}, \mathbf{2}, \mathbf{3}) \tag{3}$$

Solving for the actuator position, z_i results in the inverse kinematic equation

$$\boldsymbol{z_i} = \boldsymbol{z} \pm \sqrt{\boldsymbol{L}^2 - (\boldsymbol{x} - \boldsymbol{Rcos}(\boldsymbol{\theta_i}))^2 - (\boldsymbol{y} - \boldsymbol{Rsin}(\boldsymbol{\theta_i}))^2}, \ \ (\boldsymbol{i} = \mathbf{1}, \mathbf{2}, \mathbf{3}) \tag{4}$$

A physical analysis of the system as configured (Figure 18) shows that the ± in the equation will be a + for this setup.

Jacobian Matrix

To determine the Jacobian, the velocity relationship between the actuators and the end effector must first be found. By differentiating equation 4 with respect to time, the velocity relationship can be determined, leading to

$$(\boldsymbol{z} - \boldsymbol{z_i})\dot{\boldsymbol{z}}_{\boldsymbol{\iota}} = (\boldsymbol{x} - \boldsymbol{x_i})\dot{\boldsymbol{x}} + (\boldsymbol{y} - \boldsymbol{y_i})\dot{\boldsymbol{y}} + (\boldsymbol{z} - \boldsymbol{z_i})\dot{\boldsymbol{z}}, \ \ (\boldsymbol{i} = \mathbf{1}, \mathbf{2}, \mathbf{3}) \tag{5}$$

Which, rearranged to solve for $\dot{z}_i$, yields

$$\dot{\boldsymbol{z}}_{\boldsymbol{i}} = \frac{(\boldsymbol{x} - \boldsymbol{x_i})}{(\boldsymbol{z} - \boldsymbol{z_i})}\dot{\boldsymbol{x}} + \frac{(\boldsymbol{y} - \boldsymbol{y_i})}{(\boldsymbol{z} - \boldsymbol{z_i})}\dot{\boldsymbol{y}} + \dot{\boldsymbol{z}}, \ \ (\boldsymbol{i} = \mathbf{1}, \mathbf{2}, \mathbf{3}) \tag{6}$$

Because the system is mechanically limited to only translational movement, the Jacobian is only comprised of this velocity relationship, which in matrix form is

$$\boldsymbol{J} = \begin{bmatrix} \frac{(\boldsymbol{x} - \boldsymbol{x_1})}{(\boldsymbol{z} - \boldsymbol{z_1})} & \frac{(\boldsymbol{y} - \boldsymbol{y_1})}{(\boldsymbol{z} - \boldsymbol{z_1})} & \mathbf{1} \\ \frac{(\boldsymbol{x} - \boldsymbol{x_2})}{(\boldsymbol{z} - \boldsymbol{z_2})} & \frac{(\boldsymbol{y} - \boldsymbol{y_2})}{(\boldsymbol{z} - \boldsymbol{z_2})} & \mathbf{1} \\ \frac{(\boldsymbol{x} - \boldsymbol{x_3})}{(\boldsymbol{z} - \boldsymbol{z_3})} & \frac{(\boldsymbol{y} - \boldsymbol{y_3})}{(\boldsymbol{z} - \boldsymbol{z_3})} & \mathbf{1} \end{bmatrix} \tag{7}$$

Substituting for the values of x_i, y_i, and z_i yields

$$\boldsymbol{J} = \begin{bmatrix} \frac{\boldsymbol{Rcos}(\boldsymbol{\theta_1}) - \boldsymbol{x}}{\sqrt{\boldsymbol{L}^2 - (\boldsymbol{x} - \boldsymbol{Rcos}(\boldsymbol{\theta_1}))^2 - (\boldsymbol{y} - \boldsymbol{Rsin}(\boldsymbol{\theta_1}))^2}} & \frac{\boldsymbol{Rsin}(\boldsymbol{\theta_1}) - \boldsymbol{y}}{\sqrt{\boldsymbol{L}^2 - (\boldsymbol{x} - \boldsymbol{Rcos}(\boldsymbol{\theta_1}))^2 - (\boldsymbol{y} - \boldsymbol{Rsin}(\boldsymbol{\theta_1}))^2}} & \mathbf{1} \\ \frac{\boldsymbol{Rcos}(\boldsymbol{\theta_2}) - \boldsymbol{x}}{\sqrt{\boldsymbol{L}^2 - (\boldsymbol{x} - \boldsymbol{Rcos}(\boldsymbol{\theta_2}))^2 - (\boldsymbol{y} - \boldsymbol{Rsin}(\boldsymbol{\theta_2}))^2}} & \frac{\boldsymbol{Rsin}(\boldsymbol{\theta_2}) - \boldsymbol{y}}{\sqrt{\boldsymbol{L}^2 - (\boldsymbol{x} - \boldsymbol{Rcos}(\boldsymbol{\theta_2}))^2 - (\boldsymbol{y} - \boldsymbol{Rsin}(\boldsymbol{\theta_2}))^2}} & \mathbf{1} \\ \frac{\boldsymbol{Rcos}(\boldsymbol{\theta_3}) - \boldsymbol{x}}{\sqrt{\boldsymbol{L}^2 - (\boldsymbol{x} - \boldsymbol{Rcos}(\boldsymbol{\theta_3}))^2 - (\boldsymbol{y} - \boldsymbol{Rsin}(\boldsymbol{\theta_3}))^2}} & \frac{\boldsymbol{Rsin}(\boldsymbol{\theta_3}) - \boldsymbol{y}}{\sqrt{\boldsymbol{L}^2 - (\boldsymbol{x} - \boldsymbol{Rcos}(\boldsymbol{\theta_3}))^2 - (\boldsymbol{y} - \boldsymbol{Rsin}(\boldsymbol{\theta_3}))^2}} & \mathbf{1} \end{bmatrix} \tag{8}$$

From **7**, it can be seen that if $z=z_i$, a singularity will occur in the Jacobian. This is mechanically the case when an arm is in the horizontal position, fully extended away from the actuation tower, and means that small changes of the position of the actuator will no longer contribute to changes in the end effector position. Another interesting case occurs when $x=x_i$ and $y=y_i$, which is the case when the arm is parallel to its actuation tower, and x-y motion of the end effector becomes independent of that actuator. The final thing of note is that the Z position of the end effector is a unit function of all three actuators, indicating that any kinematic relationships in the build volume will be uniform along the vertical axis, and can be represented by the cross section at the $Z_0=0$ plane, greatly simplifying further analysis.

Condition Number and Local Conditioning Index

To estimate the relationship between the error in actuation input and the resultant error in end effector position, the condition number of the Jacobian matrix can be used[70]. To do this, a matlab program was used (Appendix A) which generated a 1000x1000 element matrix representing the X_0-Y_0 plane, and the Jacobian and its condition number were calculated at each position. The local conditioning index is then the reciprocal of the condition number, and should be kept above a threshold to maintain a good conditioned workspace. Because the limits of the arms' range are circles centered at the virtual actuator position, the maximal workspace shape is the intersection of these three circles, and so a valid result is only generated for these positions in the matrix. A contour plot of the matrix then shows the distribution of the LCI over the surface of the workplane (Figure 19), which can be used to determine the maximum size of a given shape of good conditioned workspace by inscribing it within the desired contour. For simplicity, a circle was chosen, for which it can be seen the radius will be the point on the line $y=0$ and $x<0$ with the minimum desired LCI.

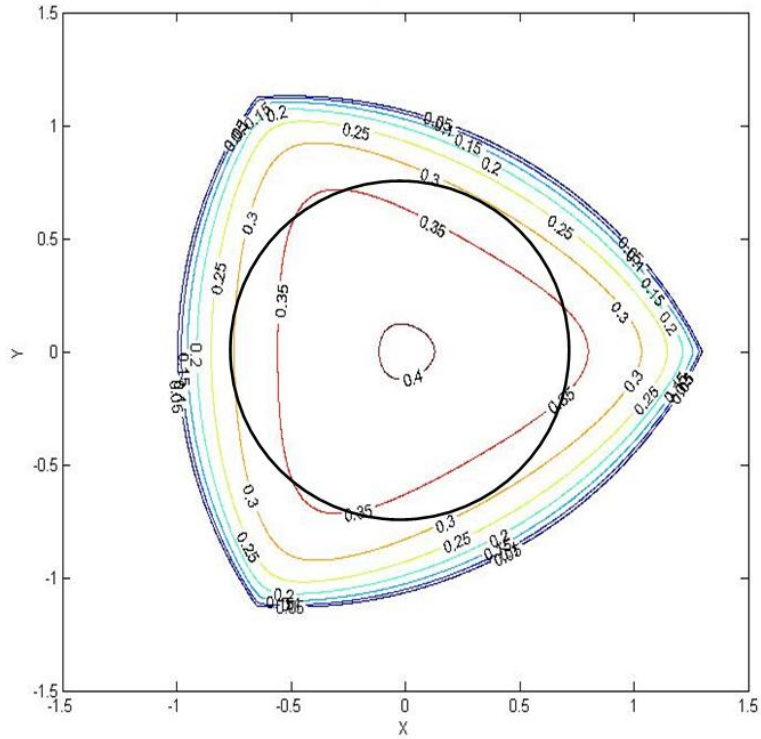

Figure 19: Contour lines of the Local Conditioning Index across the maximal workspace of a PULD system with L=2R=2.

The circle inscribed in the LCI=0.3 contour represents the good conditioned workspace used in further analysis.

Optimization of Link Length

To optimize the relative sizes of the arm length L and tower radius R, a normalized arm length *l* and normalized tower radius *r* were created such that

$$\boldsymbol{l} = \frac{\boldsymbol{2L}}{\boldsymbol{L+R}} \text{ and } \boldsymbol{r} = \frac{\boldsymbol{2R}}{\boldsymbol{L+R}} \qquad (9)$$

Examining the feasible values for *l* and *r*, it can be seen that since L must be larger than R for the system as specified to function

$$\lim_{L\to\infty \text{ or } R\to 0} \boldsymbol{l} = \boldsymbol{2} \quad \text{and} \quad \lim_{R\to L} \boldsymbol{r} = \boldsymbol{1} = \lim_{R\to L} \boldsymbol{l} \qquad (10)$$

So the normalized arm length can only have values between 1 and 2. Graphing the size of the radius of the maximum inscribed good conditioned workspace circle for LCI≥0.3 versus the normalized arm length provides a means to determine the optimum relative sizes of these elements (Figure 20). The highest point on the curve is then the optimum normalized arm length, and corresponds to a value of 1.342. Practically, this means that

the ratio of the arm length to the tower radius should be ~2.04 to ensure good conditioning over the largest possible build area.

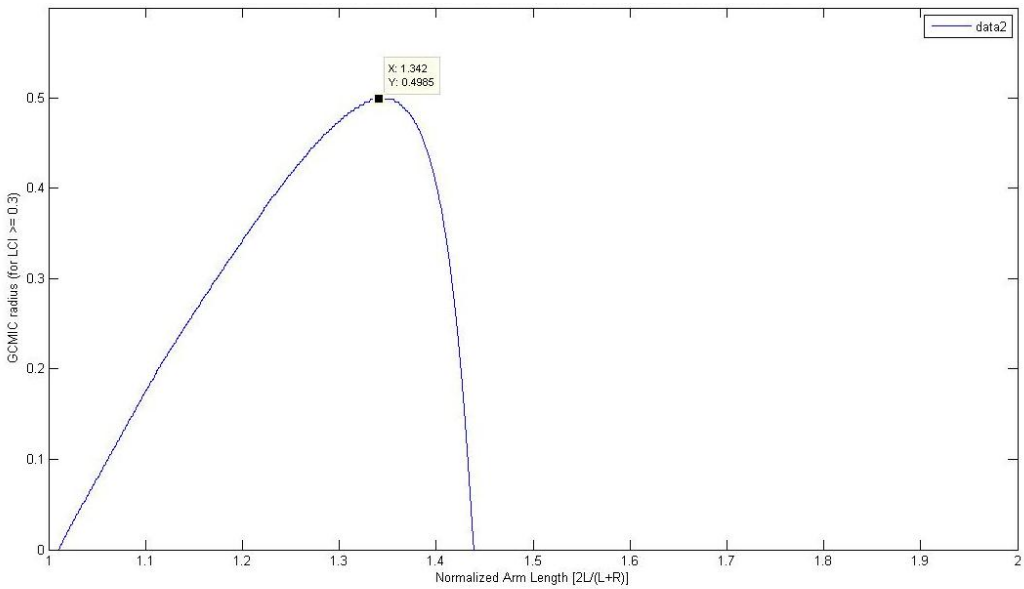

Figure 20: Good conditioned maximum inscribed circle radius vs. normalized arm length (LCI≥0.3).

3.2. Fabrication of Low-melt Alloy Filament

In addition to the FFF system, a method was needed to produce custom filament. At first, an automatic filament extruder system was investigated, and a Filastruder kit was utilized. This system is based on an open-source design for home filament extrusion, such as the Lyman filament extruder [71]. While this system proved useful for other filament materials, it was determined that it would not be suitable for metal filament fabrication due to the risk of alloying with parts, as well as the large volume of material needed to reliably produce filament. Metal casting was then considered, as previous work had demonstrated it to be effective for producing test samples[72]. A bottom casting melting pot, commonly used for bullet casting, was used for alloy mixing and dispensing. To provide more accurate temperature control, the melting pot was modified by adding a thermocouple probe in contact with the bottom of the pot, which was used for feedback to a PID controller (REX C100) which controlled the power delivered to the pot.

3.2.1. Production of Molten Alloy

Alloy components were added to the pot under ambient conditions, and a graphite rod was used to stir the mixture and skim off excess dross. Initially all components were added simultaneously, and the temperature was increased to just above the expected liquidus temperature of the composition. This worked well for the plain tin-bismuth alloys, but when the silver was added, it was found that the silver was not dissolving into the solution well. To address this, the tin was first melted with the silver at a higher temperature to bring it into solution, then the temperature was reduced and the bismuth was added. This resulted in all of the silver going into solution, while minimizing dross production. Adding the silver to the bismuth may be better, as its reactivity is lower, so the higher oxidation rate due to higher temperatures will be somewhat mitigated (Appendix E). Once the alloy was thoroughly mixed and molten, it was cast either directly into a filament mold, or into an interim mold to form an ingot for later use. Any residual material in the pot was scraped out; however it was impossible to remove all of it, so some minor contamination of the samples was expected.

3.2.2. Production of Alloy Metal Filament

Several different techniques were investigated for producing test samples of metal alloy filament. The first, and simplest, was trying to cast the alloy directly into 2mm ID PTFE tubing from the melting pot. Unfortunately, this was not successful, as the metal quickly cooled and plugged the tube, limiting the useful length produced to only a few centimeters. Larger tubing was also used, followed by drawing of the filament using a wire drawing plate; however any minor defects in the cast, such as voids or contaminants, would cause the wire to break, making this process unsuccessful for large lengths. During this testing, PTFE tubing was eliminated as a casting mold, as the temperatures needed to maintain the alloy in a liquid state were sufficiently high to substantially soften the PTFE tubing, resulting in uneven casting results. A search for other suitable materials resulted in a switch to a high temperature silicon tubing commonly used for masking parts during high temperature coating processes. To keep the alloy from solidifying in the tubing, the whole process was then attempted inside of a heated oven, however it was discovered that the new tubing was substantially

hygroscopic, resulting in offgassing during the casting process, with the resulting filament having many voids along its surface. To mitigate this, the tubing was heated prior to casting for several hours under vacuum to remove the majority of the absorbed moisture. As a result of this process, the tubing changed from a milky translucent to crystal clear, indicating the removal of the absorbed moisture. It was found that the tubing would return to the milky color within a day or two if left out, so the pre-treatment was needed before each casting to prevent bubbles forming in the molten alloy.

Initial tests in the oven using gravity to feed the material into the tubing proved less than satisfactory, and after several unsuccessful attempts, it was found that using suction on the opposite end of the tubing, which was fed out of the oven, to pull the molten alloy into the tubing while the whole system was heated inside the oven was the most effective method of casting. For small amounts of filament, a syringe was used, while larger lengths were created by attaching the end of the tubing to a vacuum pump (Figure 21). The cold section of tubing outside the oven served as a stop for the filament, as it would freeze as soon as it reached the point where the tubing exited the oven. After the molten alloy had been drawn into the tubing, it was removed from the oven to cool, and then carefully extracted from the tubing. It was found that extraction was facilitated by allowing the tubing to reabsorb moisture from the air prior to attempting to remove the filament, as this reduced the adhesion of the tubing to the filament, allowing it to more easily slide from the tubing, and making it possible to recover the tubing for reuse.

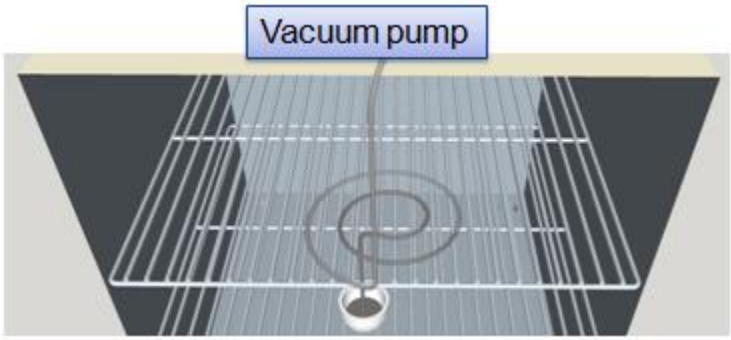

Figure 21: Filament Casting Setup.

3.2.3. Filament Joining and Storage

After the filament was removed from the tubing, it was rolled onto a spool for storage, as well as to test for defects along the length of the filament, which might result in the filament breaking during use. To test the filament integrity, it was wrapped around a large mandrel, ~100mm in diameter. In addition to testing for defects, this also served to coil the filament for storage. Breaks in the filament could be repaired by inserting the broken ends into a length of tubing with a hole cut in the center, coating a small amount of soldering flux onto the ends, and applying extra molten material with a soldering iron to fuse the two pieces back together (Figure 22). Subsequent trimming and polishing returned the material to its original shape. This method could also be used to attach multiple pieces of cast material into longer lengths for testing, which was vital due to the long length of the Bowden material delivery tube for the Rostock Max printer. Once the filament was finished being tested and had been fused into a single continuous length, it was transferred onto a spool for storage and use on the printer (Figure 23).

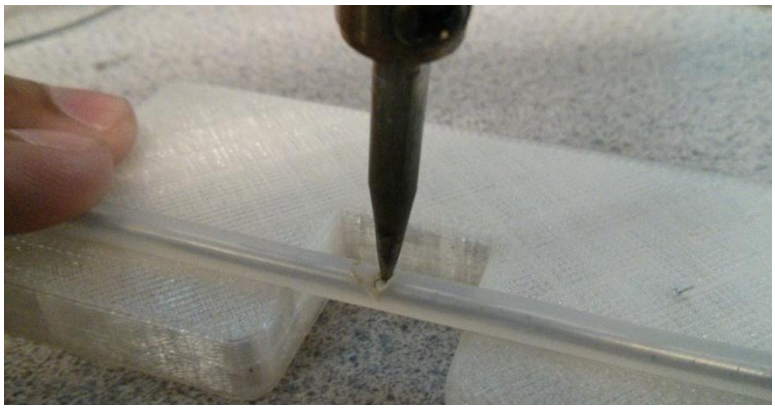

Figure 22: Filament joining jig.
When two pieces of filament needed to be joined together to produce a continuous length for printing, the ends were filed flat, inserted into the silicone tubing in the jig, and soldering flux was applied through the hole. Subsequent heating of the joint, and addition of extra material if needed, fused the ends together. After removal, the joint was cleaned of flux and any extra material was filed off.

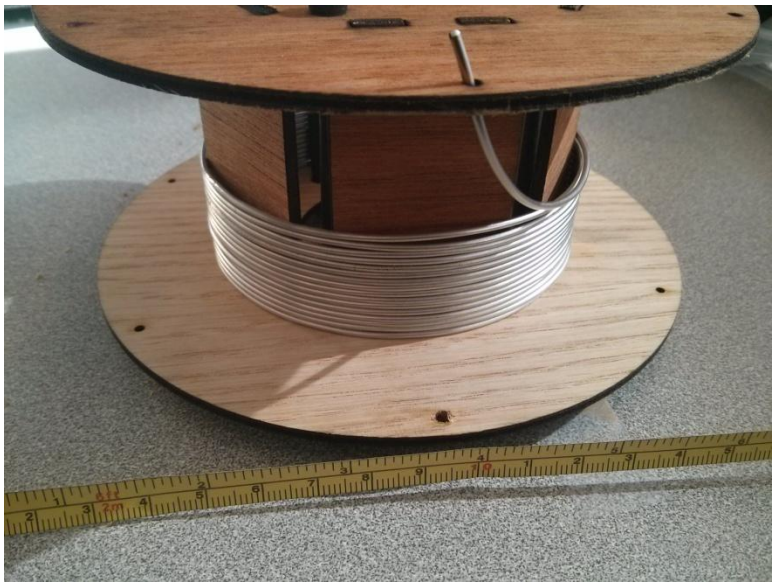

Figure 23: Filament stored on spool, ready for 3D printing.

Chapter 4.
Design and Analysis of Low-melting Metal Alloy Filament

As the popularity of Fused Filament Fabrication (FFF) has grown, more exotic materials have emerged which have expanded the applications for which 3D printed parts can be used. In addition, the possibility of combining multiple materials with very different properties into a single print drastically increases the fabrication capabilities of the system, and would allow the production of parts with unique properties. Of these materials, electrically conductive and metallic materials are an area of interest, both in research facilities, and the general public. In fact, one of the most common questions the author has received while demonstrating his 3D printer at public events has been whether or not it is possible to print metal objects. Unfortunately, most of the research to date on electrically conductive materials for 3D printing applications has focused on using direct writing of expensive nano-material inks, which often require post-processing by thermal curing[73]. While there have been some successes, such as the Voxel8 3D printer [10], the high cost of the materials used, and the different deposition systems needed to combine them will be an impediment to widespread use. To overcome this, it would be desirable to have a filament which could be used on a standard FFF system, which is able to achieve the high conductivities needed for electrical systems, but does not contain expensive materials.

Several attempts have been made to develop composite materials, using additives such as carbon black[8], and graphene[9], and while substantially conductive materials have been demonstrated, the resistivity of the materials exceed that of metals by several orders of magnitude. One way to overcome this is to use embedded metal wires, which are integrated into the print by heating them, causing them to melt the surface of the part, and embed [73]. While this overcomes the issue of conductivity, it is difficult to connect the wires across layers or to components in the device. Although the

high melting temperature for most metals preclude them from use with the thermoplastic polymers used in FFF, recent efforts to find new solder materials, due to the banning of lead in Europe[74], has resulted in a renewed interest in low melting point alloys.

This chapter covers the work done on optimizing a metal alloy for FFF 3D printing, and subsequent integration into a multi-material FFF 3D printer. Previous works done on this subject have focused on a single material, with little to no analysis of the various materials optimizations possible. In addition, the recent shift from lead based to lead free solders due to new regulations prohibiting the use of lead in consumer products has meant that there has been a renewed interest in developing and studying new low melting temperature alloys to develop replacement solder alloys.

This chapter can be broken down into four sections:

- A review of the literature concerning solder alloys and additive manufacturing of low melting alloys, which was used as a starting point to determine potentially useful materials and combinations. Because of the renewed interest in solder alloys, more details are now available about the effect of various metals on low melting point alloys, providing the details needed to optimize the alloy composition.

- A materials selection and analysis process was then undertaken to determine potential candidate alloys. Starting with a base alloy, the composition and the effect of doping was studied.

- Several sample filaments were produced and tested. Microstructure was examined prior to printing to understand the possible impacts on printing parameters, and afterwards to understand the effect on the final properties of the printed material. Also, melting behaviour and some mechanical properties were analyzed.

- Finally, the filaments were tested on the 3D printer with various nozzle setups to determine the optimum print settings for producing multi-material 3D objects.

4.1. Background

To better understand the available materials and their effects on the alloy, a survey of the available literature on low melting temperature alloys was conducted.

Because of international pressure to remove lead from consumer products, there has been a recent surge in the research on lead-free alloys to find suitable replacements of the commonly used Sn63Pb37 solder. In addition, and partially as a result, several databases of lead-free solder components and their phase diagrams have become available [75], [76]. The mechanical properties of a broad range of mixtures has also been evaluated, providing data for optimization of the composition to specific applications[77]. While most of this information is tailored towards electronics applications, the trends and dopant effects can also be applied to other applications of low-melting alloys such as additive manufacturing. In addition to the materials, the effect of using a low melting alloy with a substantially non-eutectic composition was investigated, as previous work has shown this to be a promising way to control the viscosity of the material during deposition [78], [79], which is critical to ensuring that the material will maintain its shape during the deposition process. Finally, a survey of other work on additive manufacturing of low melting alloys was conducted, and the alloys, as well as the processes used to deposit them, were examined.

4.1.1. Solder alloy background

As a greater awareness of the environmental impact of the materials and processes used in the manufacturing of consumer goods has become more popular, there has been pressure to remove toxic components. One such component is the lead-based solder commonly used in electronics assembly. To help find a suitable replacement for this material, a number of research institutes, including the National Institute of Standards and Technology (NIST) and the National Physical Laboratory (NPL) have released databases of low-melting alloy properties and phase diagrams to help promote the development of these next generation solders[75], [76]. These databases provided an invaluable resource for the investigation of the melting behaviour of two and three component systems, as well as the effect of adding small amounts of other components for specific improvements, such as strengthening, or reducing the oxidation rate of the material. Several different systems were examined, with the most promising being the SnBi system due to its ideal melting range, and reasonable cost of components. With silver being commonly used in solder alloys in small amounts to improve the mechanical properties of the material, the SnBiAg system was also studied

to determine if the addition of a small amount of silver would be beneficial to the alloy. The addition of silver also has an interesting effect in the microstructure, as it readily forms Ag_3Sn intermetallics in the form of needles. This behavior was especially interesting for extrusion applications, as there is a possibility of having thixotropic behaviour due to the needle structures remaining solid in the melt [80], [81].

4.1.2. Eutectic vs. Non-Eutectic

For most soldering applications, the preferred alloy compositions are generally at or near the eutectic composition. This is to ensure that the material quickly changes from the liquid to the solid phase allowing rapid connection of soldered parts, and reducing the risk of cracks forming due to movement of the parts while the solder is solidifying. While this is ideal for forming a small connection between two solid parts, it would not work well for additive manufacturing as the high surface tension of the material would dominate the liquid's properties[82], resulting in beading of the material, as well as making it difficult to attach new material to old without either melting the entire structure, or having poor attachment. In contrast to eutectic alloys, non-eutectic alloys are composed of both the eutectic phase, and another phase which is rich in the excess material. Because of the difference in composition of the two phases, their melting points are not the same, and as such the material will not have a single melting temperature, but instead has a melting range where the material first enters a slurry-state composed of the solid phase and the liquefied eutectic phase, before the higher melting phase eventually dissolves into solution at the upper melting temperature, referred to as the liquidus. The concentrations of the alloy which produce this can be determined by examining a phase diagram, such as that of the SnBi system (Figure 24). This provides a tool to determine the melt profile of any combination of the two elements, by examining a vertical line at the given concentration. Upon crossing the solidus, and entering the liquid+solid region, the approximate ratio of liquefied material to solid can be determined using the lever rule, in which the ratio of the sizes of each side of a horizontal line intersecting the vertical concentration line at the given temperature and ending at the liquid and solid phases respectively is the ratio of solid to liquid, with the size of the opposite side corresponding to the concentration of each.

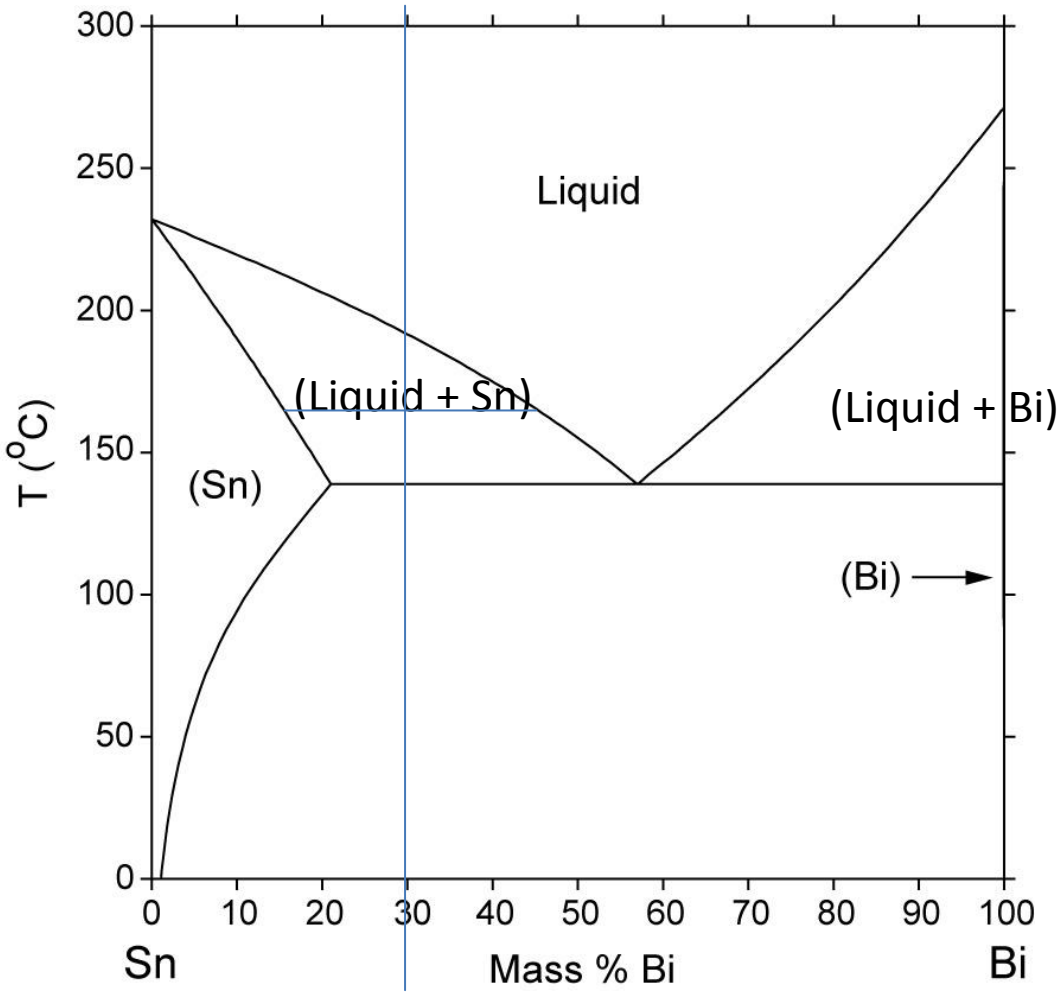

Figure 24: Phase diagram of Tin Bismuth binary alloy system.
Vertical line shows the 30% Bi composition, with the horizontal line denoting the temperature where the alloy will be composed of 50% solid Sn-rich phase and 50% liquid. Modified from [76].

4.1.3. Prior Arts on 3D Printing of Low-melting Alloy

Metal parts have traditionally been created using casting, forging, or subtractive techniques. While these methods have been highly developed and can be excellent for mass production, they suffer from serious limitations in the range of parts that can be created, and/or the need for creating expensive dies or molds. With recent advances in additive manufacturing of metals such as selective laser sintering/melting (SLS/SLM), the possibility to create complex shapes, and the ability to directly create an object from a computer model have become a reality. Unfortunately these techniques are limited to single materials, and require the use of expensive powdered materials and high-

powered laser systems. The development of metal fabrication systems which are compatible with multi-material deposition systems is therefore desirable. Due to their compatibility with polymer materials, low melting temperature alloys are an obvious choice, and as such additive systems have been developed which use these materials.

As the size of circuitry has shrunk, the need for accurate deposition of solders at high resolutions has become critical. By harnessing piezoelectric inkjet systems designed to work at elevated temperatures, molten alloys have been deposited with droplet sizes as small as 25-125μm, with rates as high as 1000 s^{-1} [83]–[85]. These systems are currently being commercialized primarily for use in flip chip manufacturing, but the possibility of integrating these with current inkjet-based 3D printers is an exciting prospect. For extrusion based systems, the focus has been on semi-solid non-eutectic alloys, as these allow for control of the viscosity of the material during deposition [81]. Materials have been developed for metal injection molding, as well as solid free-form fabrication [78]. Early systems used a large volume of semi-solid slurry, which was kept agitated to ensure precipitates did not condense, causing the system to clog. Later developments used filament-based delivery, with the material melting only in the nozzle [72], [86]. These later systems were integrated into FFF or FDM systems, with the goal of enabling multi-material 3D Printing.

4.2. Materials Space Evaluation

To determine which materials would be suitable for inclusion in a low-melting alloy filament, a survey was conducted of the materials used in solders, and other low melting alloy applications such as Babbitt bearings and low-melting casting alloys such as pewter. The predominant base metal in these alloys is tin, which has a melting point of 232°C, which is in the range of temperatures normally used in FFF 3D printers. By alloying tin with other metals, the melting point can be adjusted, as well as the melt behaviour. Surface tension and viscosity effects are also critical to the deposition process, but many of the metals do not have good data for surface tension available. In lieu of this, the surface energy of the solid was considered, as it correlated to the values of surface tension that were available, and has been well studied [87]. Thermal conductivity is an important consideration for the successful extrusion of the material,

and should be minimized in order reduce the rate of unwanted heat transfer from the nozzle to the part. In addition, the electrical conductivity of the final alloy should be maximized, so this was also considered. Oxide formation was also a worry, so an activity series for metals was consulted (Appendix E). Finally, the overall cost of the alloy is important, as the purpose of this material is to be suitable for hobby and home use, so rare and expensive materials were considered only as a last resort, and in small quantities for their dopant properties.

Table 3: Materials considered and their relevant properties.

Material	Melting point (°C)	Surface energy (J/m^2)	Thermal conductivity (W/m*K)	Cost/lb	Electrical resistivity (nΩ*m) @20°C
Gallium	29.8	0.661-1.1	40.6	125	270
Indium	156.6	0.488-0.700	81.8	300+	83.7
Tin	231.9	0.611-0.709	66.8	10.5	115 @0°C
Bismuth	271.5	0.489-0.537	8	10.5	1290
Zinc	419.5	0.99	116	.93	59
Antimony	630.6	0.535-0.659	24.4	4.5	417
Aluminum	660	1.143-1.347	237	0.8	28.2
Silver	961.8	1.172-.250	429	19.6	15.9
Copper	1084.6	1.790-2.237	401	3	16.8
Nickel	1455	2.011-2.450	90.9	8.37	69.3
PLA	170-200	0.0407			

In lieu of surface tension data, which was not found for all materials, the surface energy[87] of the solid was compared as this correlates well for most materials. PLA was added for reference[88].

After compiling the list of potential materials, phase diagrams for as many combinations of binary systems as could be found were collected (samples of some are available in Appendix E) [75], [76], [89]. In addition, several ternary phase diagrams were available as well, and provided invaluable information about the effect of dopants.

4.2.1. Melting Range Optimization

Because the alloy will be used with thermoplastic polymers with melting points near 200°C, the designed melting range of the material was set around this point. In addition, because of the need for a variable viscosity in the alloy during extrusion, non-eutectic alloys were selected, which have melting ranges dependent on the concentration of the constituent components. To determine the expected behaviour of the various alloys studied, phase diagrams for as many binary and ternary systems as could be found were collected (See Appendix E for samples). Online repositories of metallurgical data provided by the NIST Material Measurement Laboratory [76], as well as by MTDATA [75] were invaluable as references, and provided the data needed to predict the basic behaviour of various compositions. In the end however, the behaviour proved more complex than expected, so these tools only provided a starting point for optimization.

4.2.2. Thermal and Electrical Conductivity

Initial analysis of the system concluded that the thermal conductivity of the material would be an important factor for controlling the viscosity of the material. If the conductivity was too high, then depositing material onto previous layers would result in high thermal transfer, causing them to melt, and preventing the structures from being self supporting. It was thus important to try to minimize the thermal conductivity of the final alloy if at all possible. With this in mind, Bismuth was considered an excellent choice for the alloy due to its low thermal conductivity. Unfortunately this expected processing improvement comes at the cost of the electrical conductivity of the material, as Bismuth has a very low electrical conductivity in comparison to other metals (Table 3). Antimony was also considered to be a good choice for the reduction of the thermal conductivity, but the higher melting point in comparison to bismuth, as well as the lack of information on ternary systems containing antimony made it a less appealing choice. The high conductivity of silver makes it a good candidate for increasing the conductivity, while also increasing the mechanical strength.

4.2.3. Dopant Effects

In addition to the tin bismuth binary system that serves as the base of the alloy, other dopant materials were considered to provide additional benefits such as lower surface tension, lower cost, reduced oxidation rate, lower melting point, and increased conductivity. Phosphorous [90] and cerium [91] have been shown to improve the oxidation resistance of tin-based solders by producing a thin oxide shell on the surface of the melt that serves as a barrier to further oxidation. It is important to note that the oxidation resistance imparted by dopants can be concentration dependent, and in some cases small amounts of a dopant can increase the oxidation rate, while larger amounts drastically reduce it [92]. Unfortunately, phosphorous can interfere with the conductivity of the material, so the addition of iron may be necessary to counteract it, producing iron phosphide particles [93]. This has been found to have the added benefit of providing nuclei for grain growth, producing a finer grained alloy which increases the mechanical strength. Zinc and antimony were considered due to their lower cost, and a tin-zinc system was even tested briefly, but the high oxidation rate of zinc makes it a poor candidate for use in molten alloy extrusion as a major component of the alloy (Appendix I). Two common dopants found in lead-free solders are silver and copper, which help to increase the strength of the material, as well as other mechanical properties [94]. In addition, it was noticed that the silver-tin crystals in the alloy were rod shaped, which presented the possibility of having a thixotropic, or shear thinning, melt behavior, which would be desirable for better extrusion control and the mechanical stability of the semi-liquid deposited material [80], [81].

4.3. Filament Analysis

To understand how the filament behaves in the extrusion system, several analysis techniques were applied to the filament samples to characterize their properties. To determine the melting profile of the alloys, Differential Scanning Calorimetry (DSC) measurements of samples were taken. DSC provided data on the melting temperature range, as well as quantitative data on the energy needed to melt the various phases present in the material. Cross sections of the filament were taken, and after careful polishing and etching, the microstructure of the material was visualized

under light and scanning-electron microscopy. As part of the SEM analysis, the compositions of the different phases present in the crystal structure were determined by energy dispersive x-ray spectroscopy (EDXS). A crude measurement of the conductivity of the chosen alloy was also made using a length of extruded material.

4.3.1. DSC

DSC was used to measure the melting behaviour of the alloys. A ramp profile was used, which slowly increases the temperature at a set rate, while monitoring the energy needed to increase the temperature of the sample. Phase transitions, such as melting, require additional energy, and since different phases have different melting points, the heat of fusion of each phase in the material can be determined by plotting the energy deposition against the temperature (Appendix G). By studying the curve, the optimum printing temperatures can be gleaned. In addition, the specific heats of the phase transitions was measured, and by comparing their relative magnitudes and temperatures, the approximate concentration of the phases can be calculated (Table 4).

Table 4: Melting parameters of the sample alloys determined by DSC.

Sample	$T_{solidus}$	$T_{liquidus}$	Specific heat of melting of eutectic phase (J/g)	Specific heat of melting of remainder (J/g)
Sn80Bi20	138.8	210	6	34
Sn70Bi30	139.4	208.8	7.6	47.2
Sn76Bi20Ag4	137.9	201.8	9.1	68.4
Sn66Bi30Ag4	137.9	187.9	14.1	36.6

Further DSC data showing cooling results in addition to heating could provide further insight into the behaviour of the metal, especially the range in which the alloy can

be supercooled, and would be invaluable to better understanding and optimizing the printing behaviour.

4.3.2. Cross Section Optical Images

To investigate the microstructure of the alloys, cross sections of each filament were taken and the surfaces polished and etched for direct observation of the crystal structure. Polishing was accomplished using small sections of various grit sandpapers and diamond lapping pads attached to glass plates to ensure a flat surface. The sample was held using a 3D printed jig, and then carefully polished by hand on each progressively finer grit surface. When using the diamond lapping films, which have monocrystalline particle sizes of 15, 3, 0.5, and 0.1 μm, an etching step with Nital etchant was used before the 15, 3, and 0.5 μm films to remove any recrystallized material from the surface. This was necessary due to the low melting alloys having recrystallization temperatures near ambient, which allowed the heat from polishing to recrystallize the surface of the samples. After a final polish and etch, the samples were observed under a reflected light microscope, and bright-field images were taken (**Figure 25**). The images show that the alloys are composed of two to four different phases, which have different etch rates with the selected etchant, Nital. Later analysis of the different phases showed that the etchant is preferential to tin-rich areas, leaving the more bismuth rich eutectic phase smoother, and therefore more reflective, while rapidly pitting the Sn rich phase causing it to scatter more light, and appear darker in the image. In addition to the two SnBi phases, the samples containing silver showed clear evidence of the Ag_3Sn intermetallic phase, which formed needle-like structures that were extremely resistant to damage from the etchant, and due to their highly polished surface, appear white in the images. In addition to the metal phases, evidence of the polishing abrasives was also seen embedded in the surface of the material. This is a known problem with soft and easily recrystallized alloys such as this one, and was in part due to the manual polishing process used. With a more automated polishing process, these defects can be mitigated.

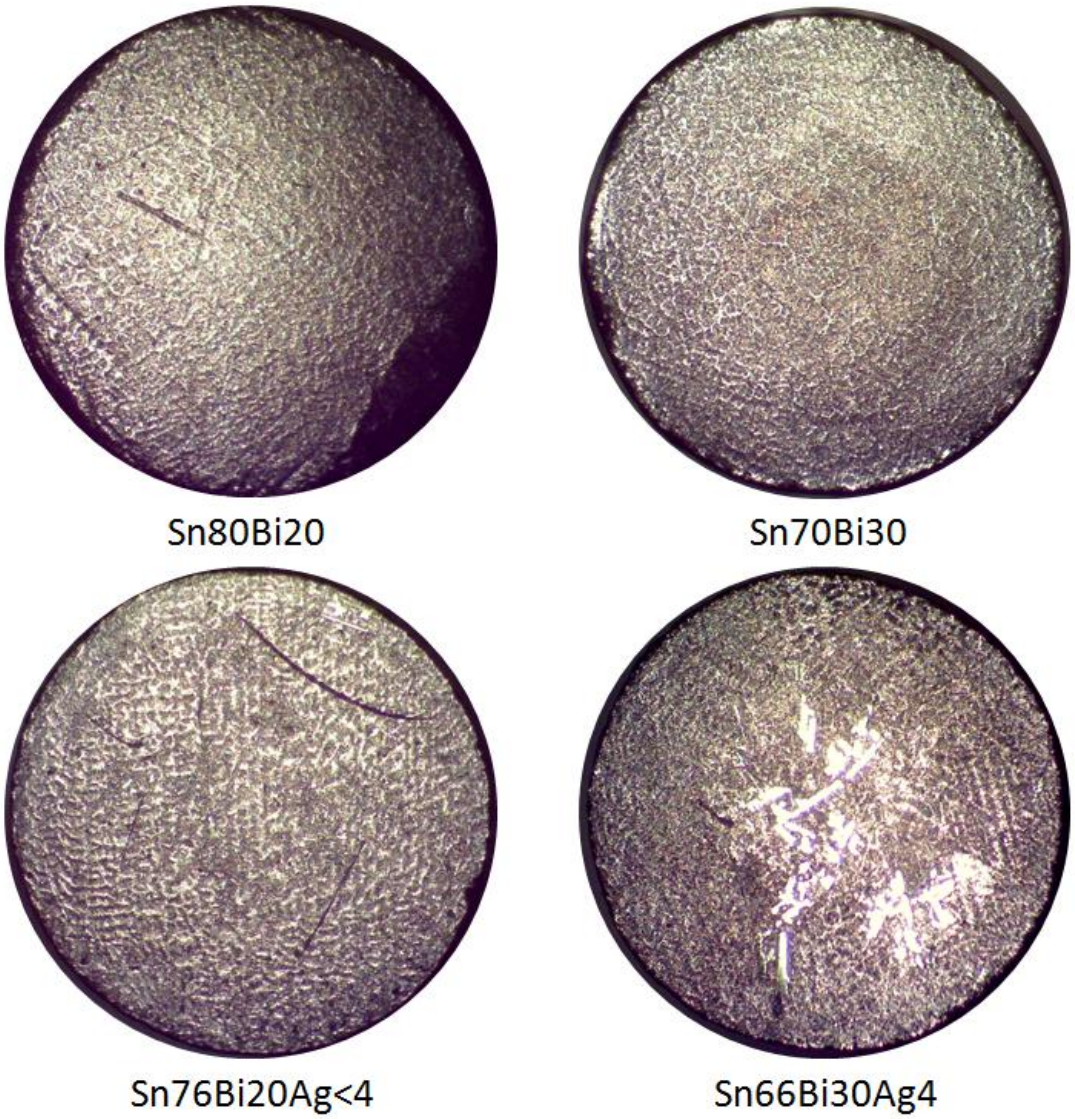

Figure 25: Optical microscope images of cross sections of filament.
Samples were polished with progressively finer grit paper down to 100nm diamond, with Nital etchant used between the last stages to ensure recrystallization was minimized. Filament diameter is 1.65mm.

4.3.3. SEM/EDS

To determine the composition of the different phases present in the microstructure of the samples, Scanning Electron Microscopy (SEM) imaging, coupled with Energy Dispersive X-ray Spectroscopy (EDXS/EDS) was used. Polished and etched samples were imaged using the secondary electron detector, followed by

subsequent spot EDS of each phase visible in the image. Quantitative data was also obtained from each point, however no calibration was performed, and the somewhat rough surface of the samples means that the data is not necessarily accurate (Appendix H). Increasing the concentration of bismuth from 20% (Figure 26) to 30% (Figure 27) shows a corresponding increase in the bismuth rich eutectic phase, and the addition of 4% silver results in the formation of Ag_3Sn intermetallic needles (Figure 28).

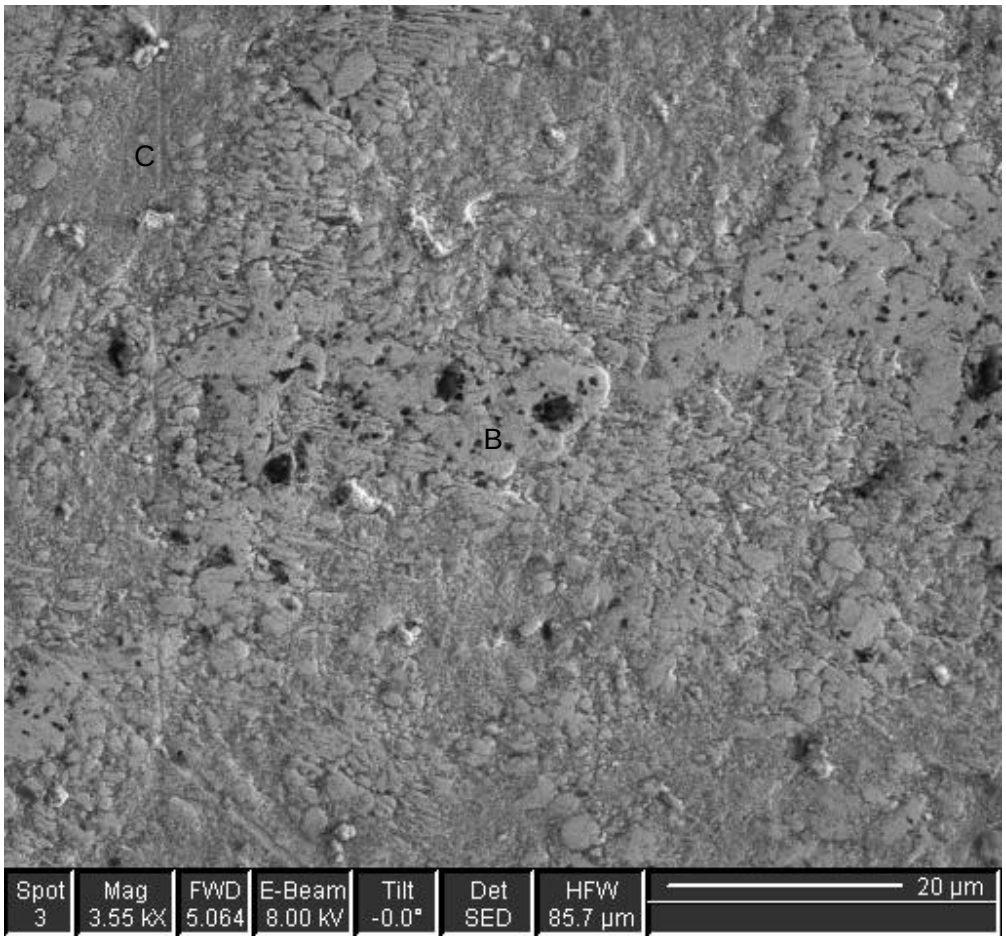

Figure 26: SEM image of cross section of Sn80Bi20 filament.
The presence of distinct phases is visible, which in order from lightest to darkest are: Eutectic (B), and Sn rich (C). Black dots are the result of embedded abrasive grit.

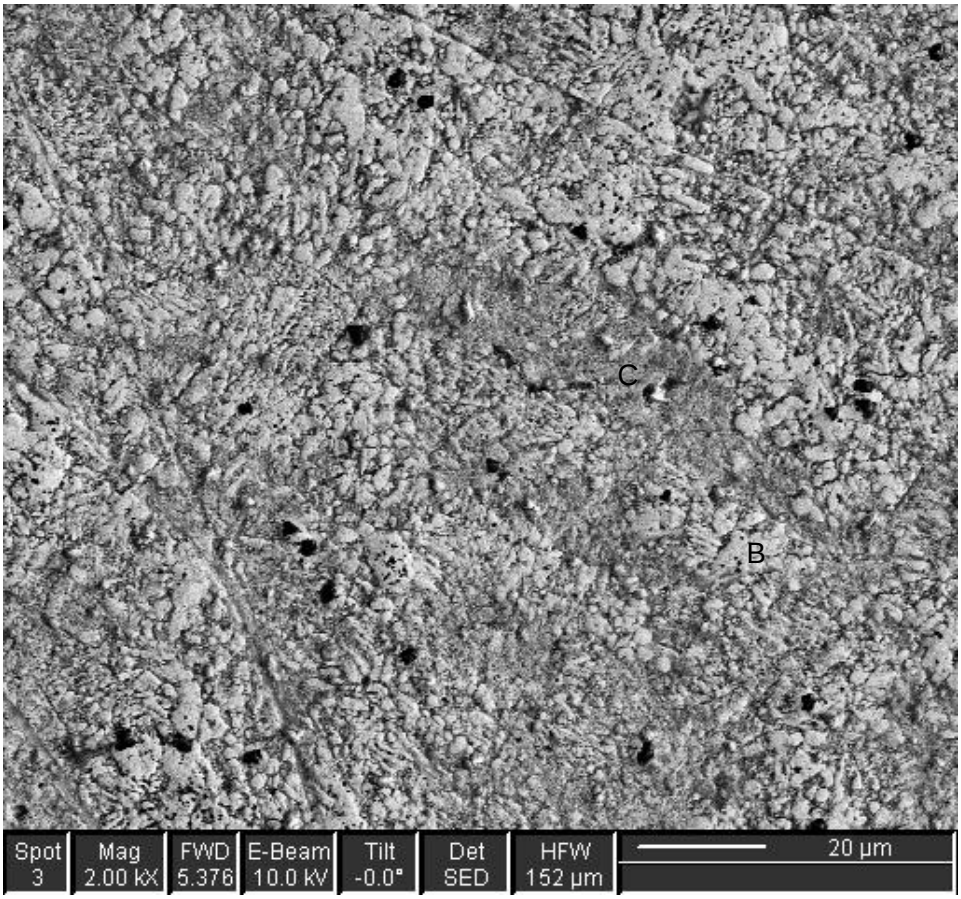

Figure 27: SEM image of cross section of Sn70Bi30 filament.
The presence of distinct phases is visible, which in order from lightest to darkest are: Eutectic (B), and Sn rich (C). Black dots are the result of embedded abrasive grit.

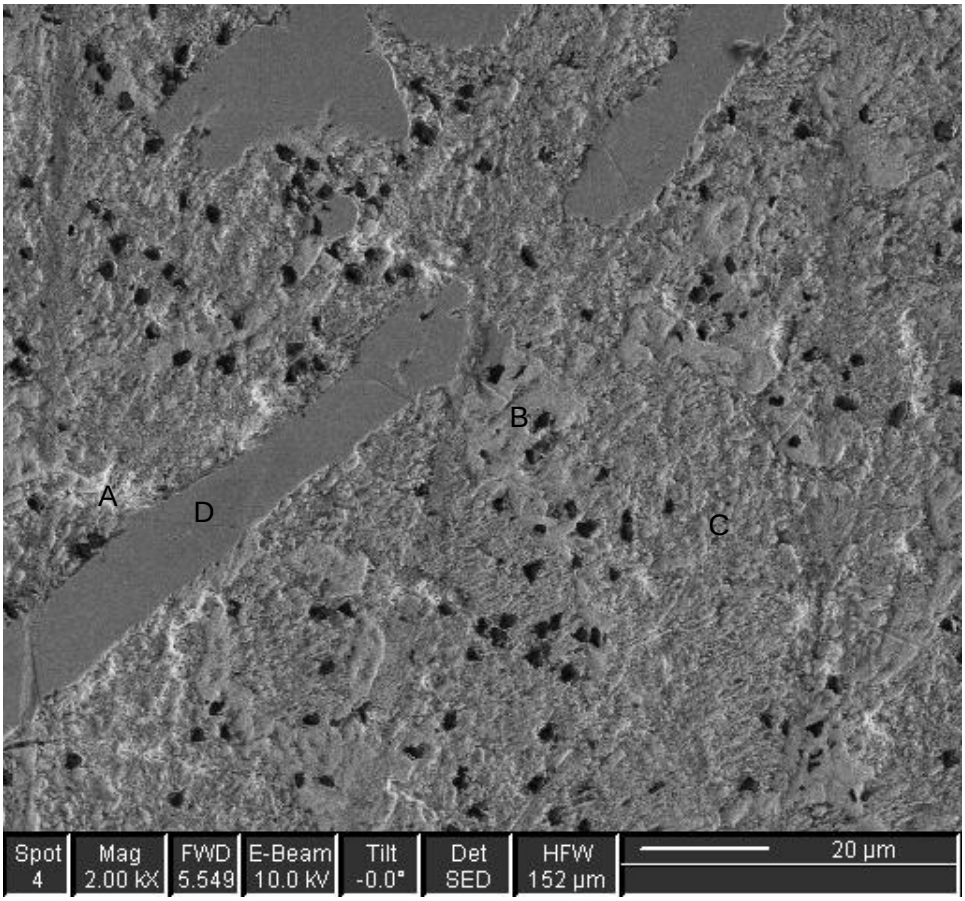

Figure 28: SEM image of cross section of Sn66Bi30Ag4 filament.
The presence of distinct phases is visible, which in order from lightest to darkest are: Bi rich (A), Eutectic (B), Sn rich (C), and Ag3Sn intermetallic rods (D). Black dots are the result of embedded abrasive grit.

4.3.4. Conductivity

To determine the resistivity of the material, the clips from an Agilent 16089B Kelvin Clip attached to an Agilent E4980A Precision LCR meter were clipped on the sample spaced 2m apart. The sample's resistance was measured at 20Hz in R-Z mode, and then the diameter of the filament was measured at several locations using a micrometer to determine an average diameter. Because only the Sn70Bi30 and Sn66Bi30Ag4 produced samples of sufficient length and quality for reliable measurement, and the addition of silver was of particular interest, these were the only samples measured (Table 5). The Sn70Bi30 sample had a diameter of 1.65mm, and a measured resistance of 240mΩ, resulting in a calculated resistivity of 257nΩm. The Sn66Bi30Ag4 sample had a diameter of 1.5mm, and a measured resistance of 260mΩ,

resulting in a calculated resistivity of 230nΩm. The replacement of some of the tin with silver provides a slight reduction in the resistance of the material as expected.

Table 5: Resistance measurements of metal alloy filaments

Material	Diameter	Resistance of 2m sample	Resistivity	Conductivity
Sn70Bi30	1.65mm	0.24 Ω	257 nΩm	38.9 kS/cm
Sn66Bi30Ag4	1.5mm	0.26 Ω	230 nΩm	43.4 kS/cm

4.3.5. Mechanical Properties

While no quantitative mechanical tests were made, the filament production process used subjected the filament to a relatively high tensile stress during the extraction process. It was found that when the process resulted in fully solid wire, the strength and flexibility of the material was high enough to survive extraction, which is in contrast to pure tin which would neck almost immediately or pure bismuth which would fracture easily. Due to contamination of the material with bubbles or other foreign particles, the material would often fracture during extraction, or while spooling the filament onto a storage reel. Of the materials tested, the Sn66Bi30Ag4 seemed to be the strongest, with the least fractures during removal. As a result of the inherent unreliability of the casting process, determining whether this was the result of a more uniform cast or the material's inherent strength was impossible.

4.4. Fused Filament Fabrication of Metal Alloys

As the ultimate goal of the development of these alloys was the use in FFF, the printing characteristics were of tantamount importance. In addition to the behavior of the metal alloy, the interactions between the alloy and the extrusion system were critical to reliable printing. One of the biggest problems was the risk of the molten metal dissolving

the material of the nozzle, and so several different nozzle materials were tested to determine the optimum material. The printing conditions and slicing parameters were also found to be of critical importance to reliable deposition, as a balance had to be struck between the surface tension, viscosity, and cooling rate of the material. Initial tests were conducted by creating free standing single wall structures, which provided good samples for interlayer bonding as well as samples for microstructural testing of the effect of the various parameters involved. Finally, integrating the printing of metal alloys with traditional FFF of plastic materials was tested.

4.4.1. Nozzle Optimization

Several different nozzle materials and configurations were tested for compatibility with the new alloy filament to determine which would be the best suited for printing (Table 6). Initial tests were conducted with a stainless steel nozzle purchased from E3D (Figure 29), however the poor thermal conductivity of the material caused the alloy to harden at the orifice and clog when lower temperatures were used, but higher temperatures resulted in cyclic filling and emptying of the melt chamber, resulting in intermittent extrusion (Appendix J). To improve the thermal transfer, two grades of aluminum were tested, Al 6061 and Al 2011. These nozzles proved to have excellent printing characteristics, but the nozzles rapidly eroded due to alloying of the nozzle material with the molten filament alloy (Figure 30). A small section of stainless steel hypodermic needle was inserted into one nozzle to test if erosion was limited to the orifice, but internal erosion still occurred, and similar problems to the all stainless nozzles were encountered (Figure 31). A passivation layer of Al_2O_3 was applied to a set of Al 6061 nozzles through hard coat anodizing, which dramatically improved the performance of the nozzles; however due to a combination of thermal cycling fatigue on the interface between the two materials, which have disparate thermal expansion coefficients, and diffusion of the alloy through the anodized layer, the coating began to crack and flake off, exposing the underlying metal to attack from the molten alloy (Figure 32). The last nozzle tried was made from brass with an electroless nickel coating applied to the surface. This nozzle exhibited excellent deposition properties, but the coating failed after several prints, causing the orifice to expand and the first layer height to lose calibration (Figure 33).

Table 6: Nozzles tested with metal alloy system

Material	Coating	Design	Comments
Stainless Steel	None	E3D v6	Poor thermal conductivity caused clogging at lower temperatures, and thermal cycling at higher temperatures
Aluminum 6061	None	E3D v6	Good printing characteristics but rapidly eroded
Aluminum 6061	SS tip	E3D v6	SS tip clogged if cooled due to poor thermal conductivity, Al base metal quickly eroded
Aluminum 2011	None	E3D v6	Good printing characteristics but rapidly eroded
Aluminum 6061	Hard Coat Anodized	E3D v6	Good printing characteristics but rapidly eroded once coating was damaged or material diffused through, causing lift-off
Aluminum 6061	Hard Coat Anodized	E3D Volcano	Large melt zone caused difficulty in maintaining extrusion at higher temperatures due to gravity overcoming other forces, causing uncontrolled release of material, followed by no extrusion
Brass	Electroless Nickel	P3D-4N1 (Makerbot MK8)	Good printing characteristics, slow erosion caused the tip to raise and the orifice to expand. Erosion increased rapidly when temperature was increased above ~220C

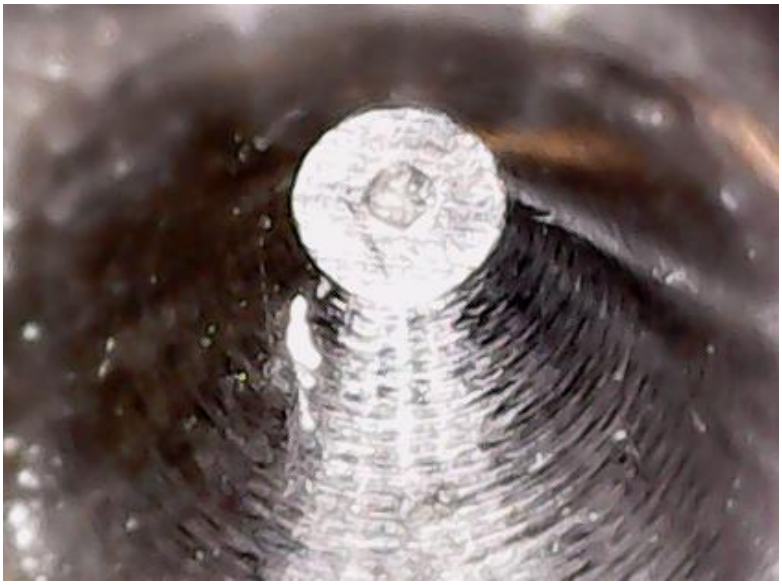

Figure 29: Stainless Steel nozzle after printing with metal alloy filaments. No evidence of erosion is visible, suggesting good compatibility of the nozzle material with the extrusion of low-melting alloys.

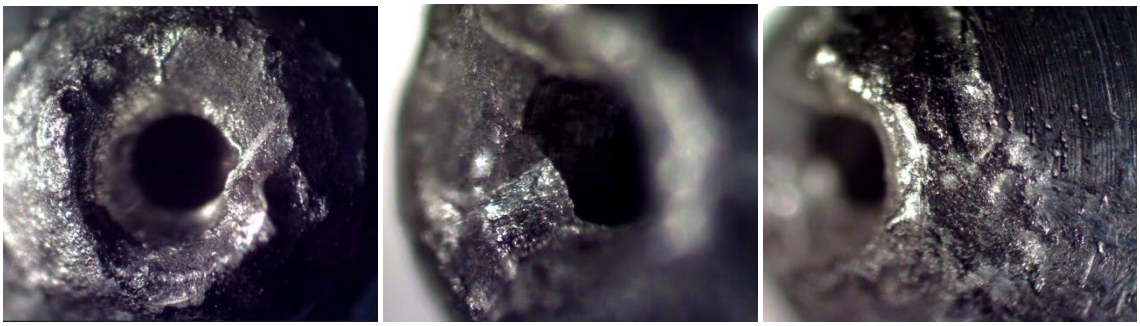

Figure 30: Images of Al 2011 nozzle orifice erosion after printing with SnBi alloy.

Image of orifice damage from a directly head on view does not differentiate between build-up of material or erosion. An angled view shows clear evidence of erosion into the nozzle, but only present at the orifice. Further into the hole, the machined structure appears to be in better shape suggesting that erosion occurs faster in the presence of air/oxides. The outer surface of the nozzle shows clear wetting behavior and erosion

Figure 31: Al 6061 nozzle with stainless steel nozzle-tip insert.

A freshly machined Al 6061 nozzle was retrofitted with a short length of 0.4mm ID stainless steel hypodermic needle to produce a non-reactive tip (top left). After testing, it was found that the metal alloy filament was dissolving the inside of the nozzle (right) and the outside of the aluminum nozzle (bottom left).

Figure 32: Al 6061 nozzle with hard anodized coating.
While the coating showed excellent extrusion properties, with a very high contact angle, it cracked upon heating of the nozzle due to the thermal expansion mismatch between the Al_2O_3 coating and the metal. Prolonged contact with the molten alloy resulted in lift off and flaking of the coating, resulting in exposure of the base metal beneath, which was then rapidly attacked by the alloy.

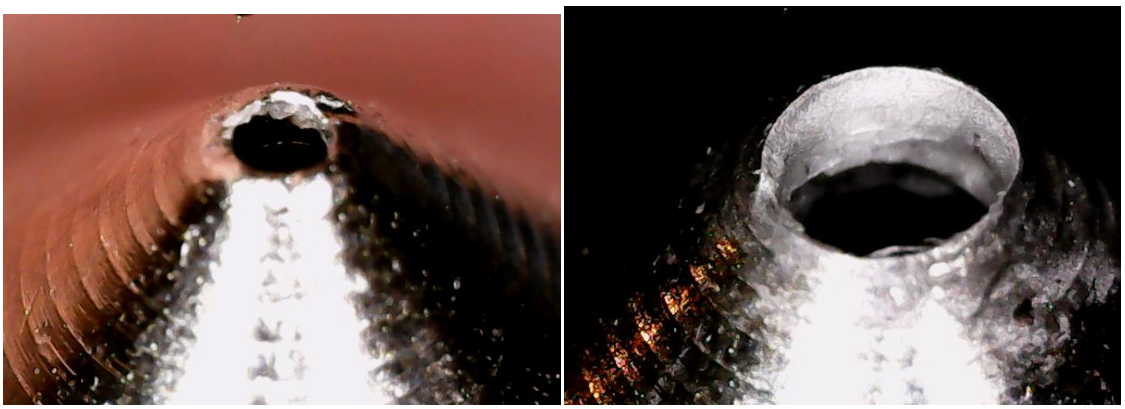

Figure 33: Electroless Nickel coated brass nozzle prior to, and after use with metal alloy filament.
Original nozzle orifice was 0.4mm ID, but expanded to nearly 1mm ID due to erosion.

4.4.2. Optimizing print parameters

In addition to optimizing the material and nozzle for printing, the process parameters such as temperature, speed, cooling, extrusion width, and layer height need to be optimized for the material. Unlike polymers, which have a broad temperature range over which their viscosity is suitable for deposition, the metal alloy has a relatively narrow range of temperatures over which the viscosity can be controlled. In addition, the high thermal conductivity of the material further reduces the effective window size by accelerating the cooling/heating process. To further confound the issue, the design and materials of the nozzle were found to significantly impact the print parameters. Thus,

each time a new system was tested, it was necessary to repeat the optimization process.

The first successful print was made using an aluminum nozzle (previous experiments had shown difficulty working with stainless steel nozzles) with a 0.5mm orifice. The nozzle was machined from 2011-T3 Al alloy, and the material was Sn79Bi21. Sample 1 (Figure 34) was produced after substantial calibration of flow rate, first layer height, and temperature. Nozzle temperature was 220°C, bed temp 100°C, and the print speed was 2.5mm/s with a single continuous spiral 1mm width extrusion with a layer height of 0.3mm. Layers are relatively even, with only minor evidence of blobbing from surface tension effects. Unfortunately, as the testing progressed, the nozzle height on the first layer kept going up due to erosion of the orifice (Figure 30), and the extrusion width had to be increased. Sample 1 was the final print performed before the nozzle was removed for analysis. Subsequent samples were produced using the remainder of this sample of filament using a stainless steel nozzle (Figure 35, Figure 36, Figure 37, and Figure 38). One of the more interesting results from these tests was the ability to produce long bridging strands. If this could be replicated and controlled, it could be used to produce overhanging, or even arbitrary structures. One of the more important factors in the success and finish of the printed parts was found to be the cooling rate of the deposited material, which was controlled by the application of a fan system to the printed material. Without sufficient cooling, the material would bead up and/or overheat the previously deposited material, causing it to begin to slump (Figure 39). While this could be used to slightly improve the surface finish of the part, the thin margin of error makes this a difficult prospect. The most successful prints were made with a fresh Al 6061 hard anodized nozzle, with the Sn66Bi30Ag4 filament, which produced reliable extrusion with excellent surface finish down to extrusion widths of 0.6mm (Figure 40).

Figure 34: Sample 1 - The first object successfully printed using the Rostock Max from a low melting temperature SnBi alloy filament.

Figure 35: Sample 2 - Made using the same settings as Sample 1, but with a stainless steel nozzle with aluminum foil wrapped around the base of the tip, and a slightly elevated temperature of 225°C.

There is clear evidence of blobbing from temperature fluctuations, and the extrusion quickly stalled after a few layers, so the print was cancelled.

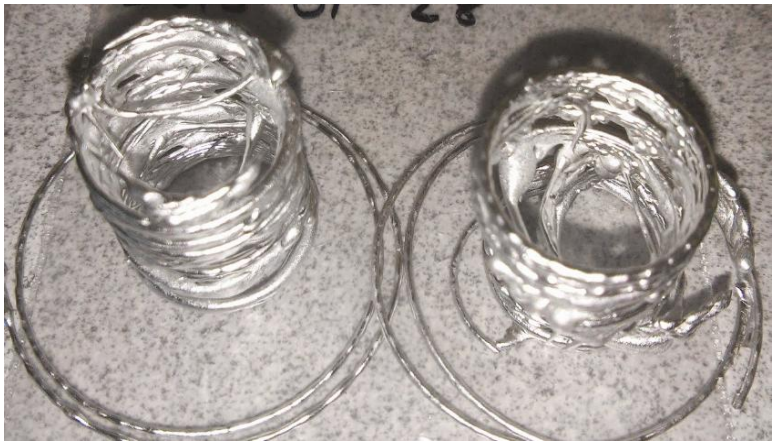

Figure 36: Sample 3 - Made using the same settings as Sample 2, but with an increase in the nozzle temp to 230°C.

Intermittent extrusion quickly became evident, with short sections of over-extruded layers, with evidence of thermal transfer from the stainless steel nozzle (softening of previous layers), followed by an interruption in the extrusion. No evidence of excessive back pressure (Extruder motor skipping) suggested that the failure was purely a thermal effect.

Figure 37: Samples 4&5 - Made with the same settings as sample 2, but elevated temperatures of 235°C and 240°C respectively.

While extrusion did appear to improve slightly, intermittent failures still occurred, resulting in blobbing and unprinted layers. Again, thermal effects were suspected, as no evidence of filament slippage or stepper skipping was witnessed, and prior to extrusion interruption, the printed layers showed evidence of high thermal and material transfer to the part.

Figure 38: Overview of samples.

After switching to an anodized aluminum nozzle, more successful prints were made, and the effect of cooling on the print was examined (Figure 39). It was found that cooling played a critical role in the fidelity of the print, and the surface finish could be controlled by adjusting the rate of cooling of the material. This would also have ramifications towards the overall mechanical integrity of a free-standing part, as too little cooling may result in the part melting, and sagging, while too much could affect the layer adhesion.

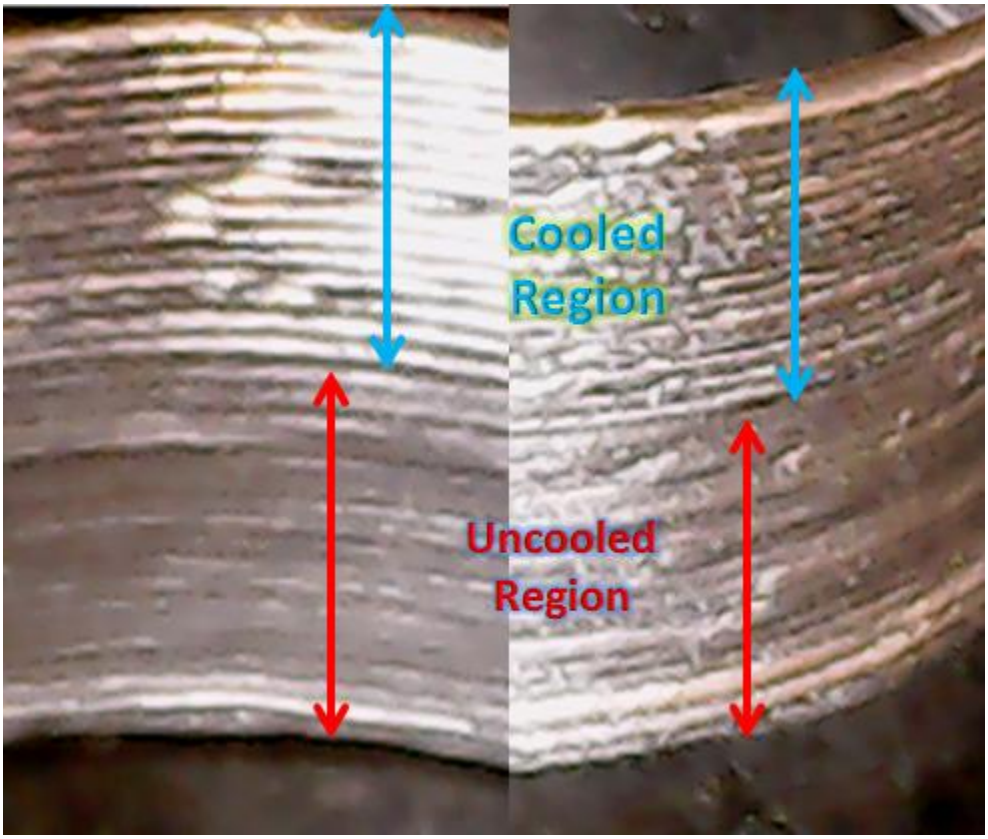

Figure 39: Effect of part-cooling fan on print quality.
A constant extrusion rate spiralized-cylinder structure was printed, with a part-cooling fan enabled for the second half of the print. Latent heat in the previously printed layer in the uncooled region causes the printed material to fully fuse, creating a smooth outer surface, whereas the cooled region shows distinct layer lines.

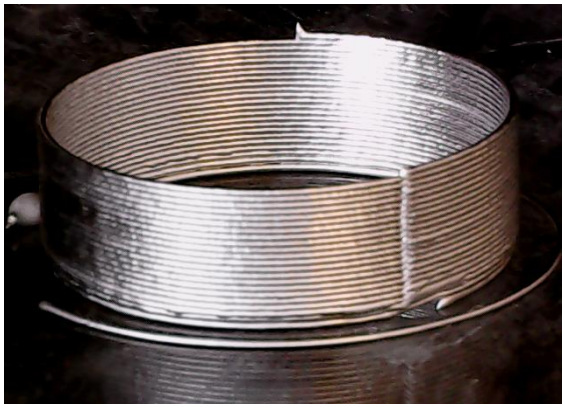

Figure 40: Sn66Bi30Ag4 printed with Al6061 hard anodized nozzle.
This combination of alloy and nozzle produced the best results in terms of even extrusion and surface finish. In addition, it also had the smallest extrusion width of any of the samples at 0.6mm.

4.4.3. Printed material analysis

The degree to which subsequently deposited material fused to previous layers was of great interest, as this has been found to be a critical parameter in the structural integrity of FFF parts, and is expected to be just as critical to the conductivity between layers of metal alloy FFF printed paths. Varying the printer parameters was expected to have an effect on this, but excellent interlayer bonding was observed for all of the parts that were successfully printed. Images of an etched cross section of a single wall SnBi sample show that the interface between subsequent depositions was minimal, with only minor differences in the crystal structure appearing at the interfaces (Figure 41).

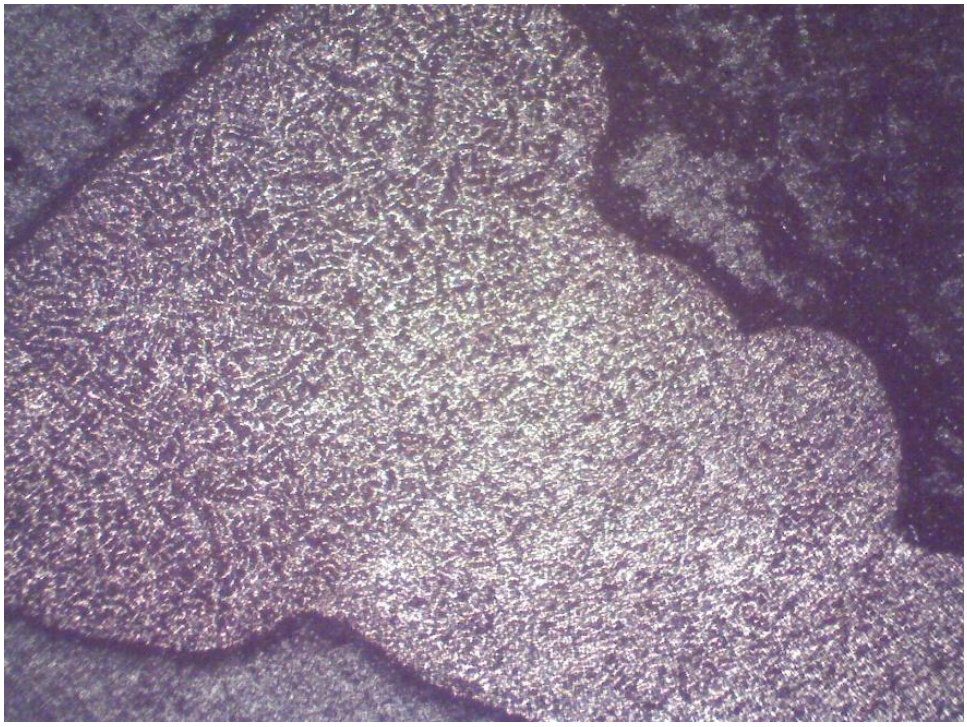

Figure 41: Etched cross section of printed SnBi printed layers showing the lack of a clearly defined interface between subsequent depositions.
The first layer was deposited directly onto glass, and was of a larger cross-section (From top left). Because of this, it has a slightly different crystal structure than the subsequent layers, and the interface to the second layer can be seen.

The effect of the addition of silver to the material was of particular interest, as it was hypothesized that the Ag_3Sn intermetallic needle structures would line up along the axis of deposition. To examine this, two cross sections of a printed sample of Sn66Bi30Ag4 were made, one transverse to the direction of deposition, one tangential

(Figure 42). Surprisingly, very little of the Ag_3Sn intermetallic was observed in the printed samples and a subsequent investigation of the nozzle used to print them showed a large buildup of Ag3Sn intermetallic crystals in the nozzle. While this was disappointing in regards to the attempted print, the possibility that the Ag3Sn intermetallic crystals can remain solid during extrusion suggests that they can be used to control the viscosity of the material through thixotropy.

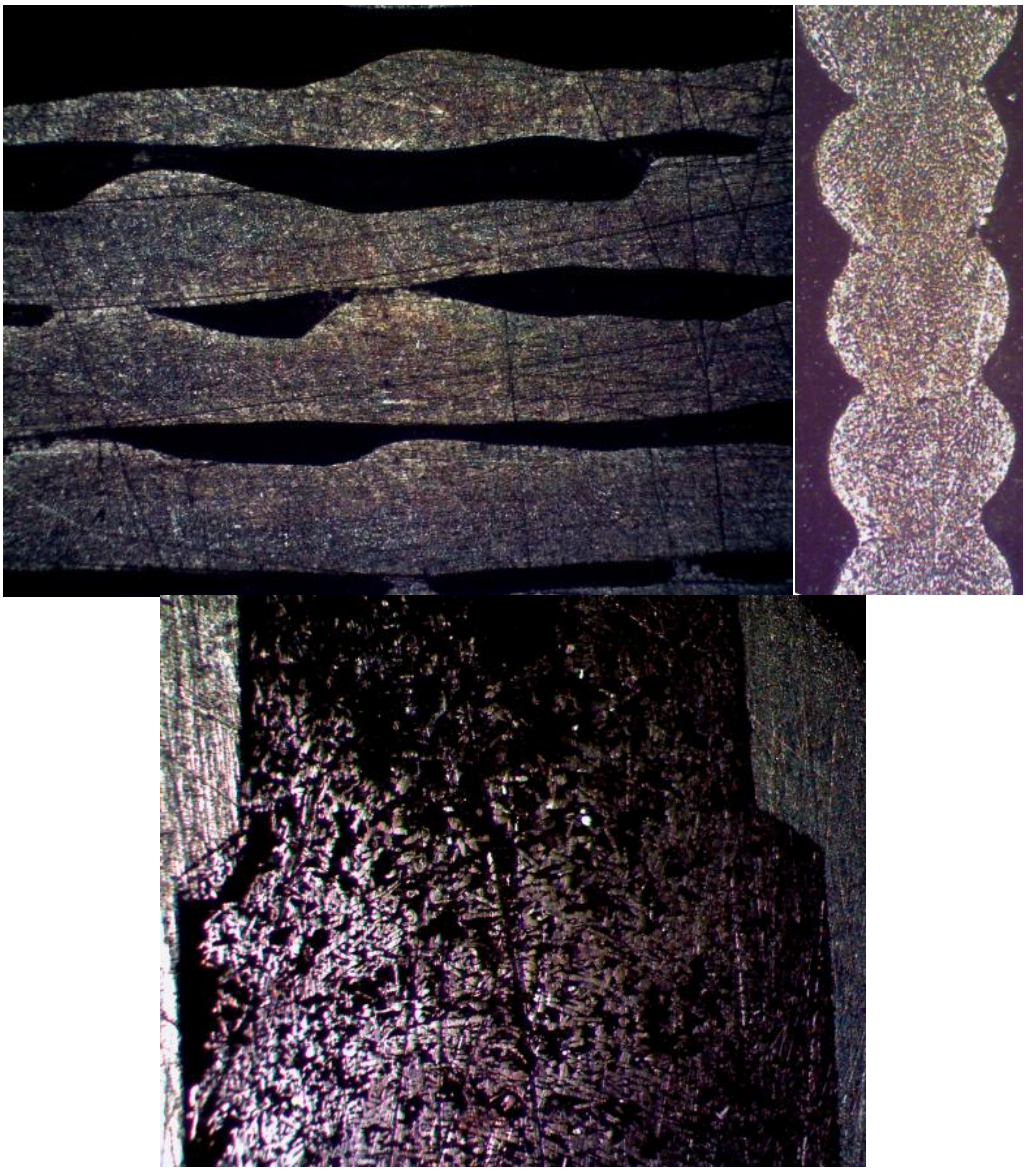

Figure 42: Cross Sections of Sn66Bi30Ag4 prints and nozzle.
Printed samples show no presence of Ag3Sn intermetallics, which appear to have been left in the nozzle.

4.4.4. Multi-material printing

The ability to combine different materials is one of the most promising emerging applications of additive manufacturing. With the development of a printable metal filament, the possibility to embed high conductivity electrical circuits within a 3D printed object is now becoming a reality. While the individual systems have been optimized for printing independently, combining the printing of multiple materials introduces its own set of challenges. Due to the close proximity of the inactive nozzle to the printed part, thermal transfer can occur, and with the stainless steel nozzles, this resulted in part contamination and oozing as a result of heating of the nozzle tip dropping the viscosity of the material (Figure 43). Later tests using the anodized aluminum nozzles were able to produce good quality traces in PLA channels, however issues with start and stop settings are still present when switching nozzles automatically (Figure 44).

Figure 43: Part contamination resulting from heating of inactive nozzle due to zero clearance.

As a result of the coplanar configuration of the nozzles, the inactive metal-dispensing nozzle comes into contact with the just-printed plastic from the other nozzle, resulting in heat transfer to the metal filament and a subsequent reduction in viscosity. This causes oozing from the inactive metal-dispensing nozzle, resulting in contamination of the part and uncontrolled deposition.

Figure 44: Printed traces in PLA channels.
Metal alloy FFF was used to produce metal traces in channels printed in PLA and either left exposed (left), or covered with subsequent layers of material (middle and right).

Chapter 5.
Conclusion and Opportunities for Future Work

With the democratization and rapid, distributed development of 3D printing technologies enabled by the creation of the RepRap project, the capabilities of Fused Filament Fabrication (FFF) systems have quickly expanded. Combined with the proliferation of low cost systems, this has resulted in a demand for new filament materials to further push the limits of what can be produced using these devices. This impetus to design new materials for use in FFF systems has led to the development and commercialization of many new filaments, including some which are electrically conductive. Combining these materials with advances in extrusion system design has enabled the production of functional parts with integrated circuitry; however, the low conductivity of these materials has severely limited their applications. As a result, there has been considerable interest in finding other materials more suitable for these applications, one such possibility being low-melting alloys. The work done for this thesis demonstrates the possibility of integrating a low-melting alloy into a FFF system, and that the material system chosen is suitable for this purpose. While the work was able to achieve a proof of concept level of work, further optimization is still needed to ensure that reliable results can be achieved.

5.1. Conclusions

Low-melting alloys provide a unique opportunity for integrating new functionalities into FFF additive manufacturing (AM). The developed alloys show high electrical conductivity, can be combined with standard thermoplastic extrusion materials, and are compatible with existing filament extrusion systems, albeit with some modifications to the nozzle. This work focused on the tin-bismuth system, in the tin-rich non-eutectic region, which demonstrated good extrusion characteristics due to its viscous nature between its solidus and liquidus. For optimization of the composition, small samples need to be prepared and tested, so a process for reliably producing useable samples was

developed and described in detail. In addition to the base alloy, the contribution of a number of different dopants was considered, and their possible effects summarized. The addition of silver changes the microstructure of the resulting filament, forming Ag_3Sn needle structures, which is believed can be used to improve the extrusion characteristics of the material by introducing thixotropy, and also slightly reduces the resistivity of the material.

Achieving reliable deposition of the metal alloy proved to be a challenge due to the incompatibility of the alloy with the nozzle in the extrusion system, and the need to carefully control the temperature of the material before, during, and after extrusion. Of the materials tested, only the stainless steel nozzle was able to withstand prolonged exposure to the molten alloy; however, the design of the nozzle proved to be poorly optimized for extrusion of the alloy, resulting in non-uniform deposition. Using the hard-anodized aluminum nozzles, good extrusion results were achieved, until the alumina coating failed. During these tests, it was discovered that by properly cooling the extruded material through the use of fans, extrusion profiles closely matching those of thermoplastic materials could be produced, allowing the production of free-standing 3D structures such as walls and even unsupported bridges. Cross sections of the printed material show the excellent fusion of the newly deposited material to the previous layer. Finally, co-deposition of the alloy into 3D printed PLA structures shows the compatibility of the material with current FFF thermoplastic materials.

5.2. Opportunities for Future Work

Metal alloy FFF brings into sharp relief the balancing act performed by the material deposition system, requiring careful optimization of all of the parameters in play. The main balance is between the capability to extrude the material, and the extruded material's ability to maintain its shape after extrusion, and most importantly, bond to the previously deposited layer to form a continuous 3D object. With thermoplastic polymers, the system is much more stable, due to the broad range of viscosities available, as well as the ease of solidifying the material by cooling and then reheating it to fusion temperatures through deposition of the next layer. This is also facilitated by the relatively low thermal conductivity of the material enabling heating to remain localized to

the material being deposited and the upper surface of the previous layer. Unfortunately, it is much more difficult with the metal alloys studied. Because of the sharp, and drastic change in viscosity with temperature, and the high thermal conductivity, the range of process parameters which can be used shrinks rapidly, requiring careful optimization of the system. Thermal conductivity of the deposition system itself also becomes an issue due to the need for non-dissolvable materials, which can have much lower values. In addition, oxidation of the material becomes a problem at higher temperatures, further limiting the possible parameters. Careful modelling of the system during deposition would be beneficial for improving the printing characteristics, by modelling the thermal transfer between the nozzle, the molten material, and the previously deposited material.

Further optimization of the material is also possible, with the addition of other components to address shortcomings in the current system, as well as optimization of the current alloy composition. In this work, the addition of silver was studied, and the differences in microstructure and their possible effects on extrusion were speculated upon, however, a quantitative analysis of the costs and benefits of this addition was not undertaken, and would be useful for determining if it is in fact a beneficial additive. For any materials tested, determining the mechanical properties of both the filament and the printed structures would also be very important, as these are of great interest when deciding if they are suitable for a given application. With prolonged use, the possibility of oxide build up is a real concern, so trace addition of rare earth metals such as Cerium and Indium could provide protection. In addition, control of the nucleation rate and/or crystal structure during filament production offers the possibility of optimizing the semi-solid melt's extrusion characteristics by controlling the size of the unmelted crystals. Viscosity measurements of the alloys over their melting range could also provide valuable data on how to optimize the material for extrusion. Finally, optimization of the path generating algorithms may be necessary to compensate for any differences in extrusion behaviour between the alloy and thermoplastics.

References

[1] J.-P. Kruth, M. C. Leu, and T. Nakagawa, “Progress in Additive Manufacturing and Rapid Prototyping,” *CIRP Ann. - Manuf. Technol.*, vol. 47, no. 2, pp. 525–540, 1998.

[2] D. I. Gibson, D. D. W. Rosen, and D. B. Stucker, “Development of Additive Manufacturing Technology,” in *Additive Manufacturing Technologies*, Springer US, 2010, pp. 36–58.

[3] R. Jones, P. Haufe, E. Sells, P. Iravani, V. Olliver, C. Palmer, and A. Bowyer, “RepRap–the replicating rapid prototyper,” *Robotica*, vol. 29, no. 01, pp. 177–191, 2011.

[4] “IBM Sees Exponential Growth of 3D Printing Industry,” *On 3D Printing*. [Online]. Available: http://on3dprinting.com/2013/03/21/ibm-sees-exponential-growth-of-3d-printing-industry/. [Accessed: 19-Jun-2014].

[5] “The Peachy Printer - The First $100 3D Printer & Scanner,” *The Peachy Printer - The First $100 3D Printer & Scanner*. [Online]. Available: http://www.peachyprinter.com/. [Accessed: 17-Jun-2014].

[6] “OneUp 3D Printer Complete Kit - Quintessential Universal Building Device - 3D Printers and Accessories Store.” [Online]. Available: http://store.quintessentialuniversalbuildingdevice.com/product.php?id_product=144. [Accessed: 17-Jun-2014].

[7] “Trend Report June,” *3D Hubs*. [Online]. Available: http://www.3dhubs.com/trends. [Accessed: 19-Jun-2014].

[8] S. J. Leigh, R. J. Bradley, C. P. Purssell, D. R. Billson, and D. A. Hutchins, “A Simple, Low-Cost Conductive Composite Material for 3D Printing of Electronic Sensors,” *PLoS ONE*, vol. 7, no. 11, p. e49365, Nov. 2012.

[9] “Conductive Graphene Filament,” *www.blackmagic3d.com*. [Online]. Available: http://www.blackmagic3d.com//ProductDetails.asp?ProductCode=GRPHN%2D175. [Accessed: 18-Jun-2015].

[10] “Voxel8,” *Voxel8: 3D Electronics Printing*. [Online]. Available: http://www.voxel8.co/. [Accessed: 18-Jun-2015].

[11] “Makerbot,” *Replicator 2X*. [Online]. Available: http://www.makerbot.com/.

[12] “RepRapPro » Tricolour Mendel.” .

[13] “OpenBuilds - H-Bot based 3D Printer by swe3tdave - Thingiverse.” [Online]. Available: http://www.thingiverse.com/thing:153461. [Accessed: 09-Jul-2014].

[14] Q. Harley, “RepRap Morgan,” *RepRap Wiki*, 28-Oct-2013. [Online]. Available: http://reprap.org/wiki/RepRap_Morgan.

[15] “Prize Specifications,” *The Uplift Prize*. .

[16] J. Rocholl, “Rostock,” *RepRap Wiki*. [Online]. Available: http://reprap.org/wiki/Rostock.

[17] “DIY 3D Printing: BerryBot Delta 3d printer and thermal containment unit.” .

[18] S. Graves, “Rostock Delta Kinematics.” .

[19] J. Arena, “Design considerations for a reconfigurable delta robot,” M.S., University of Illinois at Urbana-Champaign, 2014.

[20] “Repetier Software - The software driving your 3d printer,” *Repetier Software*. [Online]. Available: http://www.repetier.com/. [Accessed: 18-Jun-2014].

[21] D. I. Gibson, D. D. W. Rosen, and D. B. Stucker, “Extrusion-Based Systems,” in *Additive Manufacturing Technologies*, Springer US, 2010, pp. 160–186.

[22] K. Thrimurthulu, P. M. Pandey, and N. Venkata Reddy, “Optimum part deposition orientation in fused deposition modeling,” *Int. J. Mach. Tools Manuf.*, vol. 44, no. 6, pp. 585–594, May 2004.

[23] S.-H. Ahn, M. Montero, D. Odell, S. Roundy, and P. K. Wright, “Anisotropic material properties of fused deposition modeling ABS,” *Rapid Prototyp. J.*, vol. 8, no. 4, pp. 248–257, Oct. 2002.

[24] “MeshLab.” [Online]. Available: http://meshlab.sourceforge.net/. [Accessed: 19-Jun-2014].

[25] “netfabb Software - Software for 3D Printing - 3D Software for STL files - fixing, repair, editing, merge STL data for Rapid Manufacturing - STL Viewers and STL repair.” [Online]. Available: http://www.netfabb.com/. [Accessed: 19-Jun-2014].

[26] D. I. Gibson, D. D. W. Rosen, and D. B. Stucker, “Introduction and Basic Principles,” in *Additive Manufacturing Technologies*, Springer US, 2010, pp. 20–35.

[27] “Slic3r - G-code generator for 3D printers.” [Online]. Available: http://slic3r.org/. [Accessed: 23-Jun-2014].

[28] P. Kulkarni and D. Dutta, “An accurate slicing procedure for layered manufacturing,” *Comput.-Aided Des.*, vol. 28, no. 9, pp. 683–697, Sep. 1996.

[29] S. Guduri, R. H. Crawford, and J. J. Beaman, “A method to generate exact contour files for solid freeform fabrication,” in *Proceedings of Solid Freeform Fabrication Symposium*, Austin, Texas, 1992, vol. 3–5, pp. 95–101.

[30] W. Ma, W.-C. But, and P. He, “NURBS-based adaptive slicing for efficient rapid prototyping,” *Comput.-Aided Des.*, vol. 36, no. 13, pp. 1309–1325, Nov. 2004.

[31] R. Jamieson and H. Hacker, “Direct slicing of CAD models for rapid prototyping,” *Rapid Prototyp. J.*, vol. 1, no. 2, pp. 4–12, Jun. 1995.

[32] K. H. Lee and K. Choi, “Generating Optimal Slice Data for Layered Manufacturing,” *Int. J. Adv. Manuf. Technol.*, vol. 16, no. 4, pp. 277–284, Mar. 2000.

[33] RichRap, “Reprap development and further adventures in DIY 3D printing: Layer selective colour 3D printing.” .

[34] “Home - Ultimaker.” [Online]. Available: https://www.ultimaker.com/. [Accessed: 19-Jun-2014].

[35] “OctoPrint.org.” [Online]. Available: http://octoprint.org/. [Accessed: 19-Jun-2014].

[36] “List of Firmware - RepRapWiki.” [Online]. Available: http://reprap.org/wiki/List_of_Firmware. [Accessed: 26-Jun-2014].

[37] “Arduino - ArduinoBoardDue.” [Online]. Available: http://arduino.cc/en/Main/arduinoBoardDue. [Accessed: 26-Jun-2014].

[38] “Printeer - a 3D printer for kids & schools,” *Kickstarter*. [Online]. Available: https://www.kickstarter.com/projects/2001363001/printeer-a-3d-printer-for-kids-and-schools. [Accessed: 26-Jun-2014].

[39] admin, “Cube® 3,” *www.3dsystems.com*, 05-Jan-2014. [Online]. Available: http://www.3dsystems.com/3d-printers/personal/cube-3. [Accessed: 26-Jun-2014].

[40] “RepRapOneDarwinThermoplastExtruder - RepRapWiki.” [Online]. Available: http://reprap.org/wiki/RepRapOneDarwinThermoplastExtruder. [Accessed: 26-Jun-2014].

[41] “Flexystruder Tool Head.” [Online]. Available: https://www.lulzbot.com/products/flexystruder-tool-head. [Accessed: 02-Jul-2014].

[42] “Replicator Extruder for FLEXIBLE materials - Mk8 by FD_Engineer - Thingiverse.” [Online]. Available: http://www.thingiverse.com/thing:169086. [Accessed: 02-Jul-2014].

[43] “File:Extruder lemio.svg - RepRapWiki.” [Online]. Available: http://reprap.org/wiki/File:Extruder_lemio.svg. [Accessed: 27-Jun-2014].

[44] “File:70780 EZStruder perspective.jpg - RepRapWiki.” [Online]. Available: http://reprap.org/wiki/File:70780_EZStruder_perspective.jpg. [Accessed: 27-Jun-2014].

[45] M. Roxas and S. Ju, “Fluid dynamics analysis of desktop-based fused deposition modeling rapid prototyping,” Thesis: Bachelor of Applied Science, University of Toronto, Toronto, 2008.

[46] W. J. Swanson, “Consumable assembly for use in extrusion-based layered deposition systems,” US8403658 B2, 26-Mar-2013.

[47] E. Sells, “RepRap: Blog: Bowden extruder concept.” .

[48] J. LaBossiere, B. Dunn, T. McDonough, and M. Eshelma, “Single-motor extrusion head having multiple extrusion lines,” US20070228590 A1, 04-Oct-2007.

[49] “multiple filament bowden extruder drive by fritzgutten - Thingiverse.” [Online]. Available: http://www.thingiverse.com/thing:16429. [Accessed: 28-Jun-2014].

[50] Coherent, “Coherent’s Reprap Blog: Introducing the Coherent Extruder: A 4 Color, 2 Motor Cold End.” .

[51] “Multiple Extruder design for 3D printer.” [Online]. Available: http://www.lateral-i.com/a-multiple-extruder-on-a-rotating-turret-ide-for-fff-fdm-3d-printers/. [Accessed: 25-Jun-2014].

[52] “Multicolor-extruder - RepRapWiki.” [Online]. Available: http://reprap.org/wiki/Multicolor-extruder. [Accessed: 27-Jun-2014].

[53] “Screw/ Worm drive filament extruder Bowden by GadgetGuru314 - Thingiverse.” [Online]. Available: http://www.thingiverse.com/thing:209136/#comments. [Accessed: 02-Jul-2014].

[54] B. V. Reddy, N. V. Reddy, and A. Ghosh, “Fused deposition modelling using direct extrusion,” *Virtual Phys. Prototyp.*, vol. 2, no. 1, pp. 51–60, 2007.

[55] “RepRap: Blog: April 2005.” .

[56] H. S. Ramanath, C. K. Chua, K. F. Leong, and K. D. Shah, “Melt flow behaviour of poly-ε-caprolactone in fused deposition modelling,” *J. Mater. Sci. Mater. Med.*, vol. 19, no. 7, pp. 2541–2550, Jul. 2008.

[57] J. Mireles, D. Espalin, D. Roberson, B. Zinniel, F. Medina, and R. Wicker, “Fused deposition modeling of metals,” presented at the Solid Freeform Fabrication Symposium, University of Texas, 2012.

[58] reifsnyderb, “J-Head Nozzles: Hot-end Collection.” .

[59] “E3Dv6 Release Announcement & Design Details.” [Online]. Available: http://e3d-online.com/index.php?route=extras/blog/getblog&blog_id=21. [Accessed: 26-Jul-2014].

[60] “E3D-v6 All Metal HotEnd Documentation.” [Online]. Available: http://e3d-online.com/E3D-v6-Documentation. [Accessed: 15-Jul-2014].

[61] W. J. Swanson, D. F. Mannella, K. C. Johnson, and R. G. Schloesser, “Print head nozzle for use with additive manufacturing system,” US20140048969 A1, 20-Feb-2014.

[62] “E3D Online.” [Online]. Available: http://e3d-online.com/. [Accessed: 30-Jun-2014].

[63] J. J. Fong, “Cooling techniques in solid freeform fabrication,” US7011783 B2, 14-Mar-2006.

[64] “Search Thingiverse - Thingiverse.” [Online]. Available: http://www.thingiverse.com/search/?q=fan+duct&sa=. [Accessed: 26-Jun-2014].

[65] W. J. Swanson, M. A. Popa, P. W. Turley, W. R. P. Jr, P. E. Hopkins, S. Brose, D. I. Kimm, D. L. Pollard, and A. M. Hahn, “Filament cassette and loading system,” US6776602 B2, 17-Aug-2004.

[66] T. L. Taatjes, P. W. Turley, M. G. Zalusky, and T. P. Paul, “Filament guide mechanism for filament spool container,” US7938351 B2, 10-May-2011.

[67] “[WIP] Out of Filament Alarm - Auto-Pauses/Heater Shutoff when Idle (Page 1) — Hacks & Mods — SoliForum - 3D Printing Community.” [Online]. Available: http://www.soliforum.com/topic/2516/wip-out-of-filament-alarm-autopausesheater-shutoff-when-idle/. [Accessed: 19-Jun-2014].

[68] “Carbon Fiber Tube Arms with Metal Ball Rod Ends.” [Online]. Available: http://www.tricklaser.com/Carbon-Fiber-Tube-Arms-with-Metal-Ball-Rod-Ends-for-Rostock-MAX-RM-ARM-CFTX.htm. [Accessed: 09-Jun-2015].

[69] “Rambo - RepRapWiki.” [Online]. Available: http://reprap.org/wiki/Rambo. [Accessed: 09-Jun-2015].

[70] X.-J. Liu, “Optimal kinematic design of a three translational DoFs parallel manipulator,” *Robotica*, vol. 24, no. 02, pp. 239–250, 2006.

[71] “LYMAN FILAMENT EXTRUDER V4.1 by Hlyman.” [Online]. Available: http://www.thingiverse.com/thing:265375. [Accessed: 22-Jun-2015].

[72] R. O. Jones and web-support@bath.ac.uk, “Additive Manufacturing of Functional Engineering Components,” phd, University of Bath, 2013.

[73] D. Espalin, D. W. Muse, E. MacDonald, and R. B. Wicker, “3D Printing multifunctionality: structures with electronics,” *Int. J. Adv. Manuf. Technol.*, vol. 72, no. 5–8, pp. 963–978, May 2014.

[74] E. U. Parliament and E. U. Council, “Directive 2002/95/EC on the restriction of the use of certain hazardous substances in electrical and electronic equipment,” *J Eur Union*, vol. 46, pp. 19–23, 2003.

[75] “Group.” [Online]. Available: http://resource.npl.co.uk/mtdata/periodictableSolders.htm. [Accessed: 22-Jun-2015].

[76] “Solder Systems in Phase Diagrams & Computational Thermodynamics.” [Online]. Available: http://www.metallurgy.nist.gov/phase/solder/solder.html. [Accessed: 22-Jun-2015].

[77] T. Siewert, “Properties of lead-free solders,” Colorado School of Mines, 2002.

[78] C. S. Rice, P. F. Mendez, and S. B. Brown, “Metal solid freeform fabrication using semi-solid slurries,” *JOM*, vol. 52, no. 12, pp. 31–33, 2000.

[79] C. S. Rice, “Solid freeform fabrication using semi-solid processing,” Massachusetts Institute of Technology, 1995.

[80] H. A. Barnes, “Thixotropy—a review,” *J. Non-Newton. Fluid Mech.*, vol. 70, no. 1–2, pp. 1–33, May 1997.

[81] H. V. Atkinson, “Modelling the semisolid processing of metallic alloys,” *Prog. Mater. Sci.*, vol. 50, no. 3, pp. 341–412, Mar. 2005.

[82] J. Lee, W. Shimoda, and T. Tanaka, “Surface Tension and its Temperature Coefficient of Liquid Sn-X (X=Ag, Cu) Alloys,” *Mater. Trans.*, vol. 45, no. 9, pp. 2865–2870, 2004.

[83] Q. Liu and M. Orme, “High precision solder droplet printing technology and the state-of-the-art,” *J. Mater. Process. Technol.*, vol. 115, no. 3, pp. 271–283, Sep. 2001.

[84] R. E. Marusak, “Picoliter Solder Droplet Dispensing,” in *Proceedings of the Solid Freeform Fabrication Symposium, The University of Texas at Austin, Texas*, 1993, pp. 81–85.

[85] J. M. Waldvogel and D. Poulikakos, “Solidification phenomena in picoliter size solder droplet deposition on a composite substrate,” *Int. J. Heat Mass Transf.*, vol. 40, no. 2, pp. 295–309, Jan. 1997.

[86] J. Mireles, H.-C. Kim, I. Hwan Lee, D. Espalin, F. Medina, E. MacDonald, and R. Wicker, “Development of a Fused Deposition Modeling System for Low Melting Temperature Metal Alloys,” *J. Electron. Packag.*, vol. 135, no. 1, pp. 011008–011008, Feb. 2013.

[87] L. Vitos, A. V. Ruban, H. L. Skriver, and J. Kollár, “The surface energy of metals,” *Surf. Sci.*, vol. 411, no. 1–2, pp. 186–202, Aug. 1998.

[88] V. Khoshkava and M. R. Kamal, “Effect of Surface Energy on Dispersion and Mechanical Properties of Polymer/Nanocrystalline Cellulose Nanocomposites,” *Biomacromolecules*, vol. 14, no. 9, pp. 3155–3163, Sep. 2013.

[89] “ME 581 Homework Five Fall 09.” [Online]. Available: http://oregonstate.edu/instruct/me581/Homework/F09/ME581Hmwk5.html. [Accessed: 22-Jun-2015].

[90] A.-P. Xian and G.-L. Gong, “Oxidation Behavior of Molten Tin Doped with Phosphorus,” *J. Electron. Mater.*, vol. 36, no. 12, pp. 1669–1678, Nov. 2007.

[91] S. Wan Cho, K. Han, Y. Yi, S. J. Kang, K.-H. Yoo, K. Jeong, and C.-N. Whang, “Thermal Oxidation Study on Lead-free Solders of Sn-Ag-Cu and Sn-Ag-Cu-Ge,” *Adv. Eng. Mater.*, vol. 8, no. 1–2, pp. 111–114, Feb. 2006.

[92] K. Hauffe, “The mechanism of oxidation of metals and alloys at high temperatures,” *Prog. Met. Phys.*, vol. 4, pp. 71–104, 1953.

[93] “Innovations: Phosphor Bronze: Teaching an Old Dog New Tricks.” [Online]. Available: http://www.copper.org/publications/newsletters/innovations/2001/06/phosphor_bronze.html. [Accessed: 29-Oct-2014].

[94] D. R. Frear, J. W. Jang, J. K. Lin, and C. Zhang, “Pb-free solders for flip-chip interconnects,” *JOM*, vol. 53, no. 6, pp. 28–33, Jun. 2001.

[95] “Activity Series of Metals and Nonmetals 2,” *Docstoc.com*. [Online]. Available: http://www.docstoc.com/docs/113129835/Activity-Series-of-Metals-and-Nonmetals-2. [Accessed: 22-Jun-2015].

Appendix A:

Matlab code for LCI plot over build space

```
R=1;
L=2*R;
n=1000;
x=linspace(-1.5*R,1.5*R,n);
y=linspace(1.5*R,-1.5*R,n);
z=0;
theta=[0;2/3*pi;4/3*pi];
xi=R*cos(theta);
yi=R*sin(theta);
zi=zeros(n,n,3);
J=zeros(n,n,3,3);
K=zeros(n,n);
for i=1:n
   for j=1:n
      for k=1:3
         zi(i,j,k)=sqrt(L.^2-(x(j)-xi(k)).^2-(y(i)-yi(k)).^2)+z;
      end
      for k=1:3
         if isreal(zi(i,j,1)) && isreal(zi(i,j,2)) && isreal(zi(i,j,3))
            J(i,j,k,1)=(x(j)-xi(k))/(z-zi(i,j,k));
            J(i,j,k,2)=(y(i)-yi(k))/(z-zi(i,j,k));
            J(i,j,k,3)=1;
         else
            J(i,j,k)=0;
         end
      end
      if J(i,j,k)~=0
         K(i,j)=cond([J(i,j,1,1),  J(i,j,1,2),  J(i,j,1,3);  J(i,j,2,1),  J(i,j,2,2),  J(i,j,2,3);  J(i,j,3,1),  J(i,j,3,2),
J(i,j,3,3)] );
      else
         K(i,j)=Inf;
      end
   end
end
LCI=1./K;
```

Appendix B:

Matlab code for normalized arm length optimization

```
n=1000;
L=linspace(1.001,1.999,n);
R=2-L;
x=linspace(-3,0,n);
y=0;
z=0;
theta=[0;2/3*pi;4/3*pi];
zi=zeros(1,n,3);
J=zeros(1,n,3,3);
K=zeros(1,n);
LCI=zeros(n,n);
i=1;
for u=1:n
   xi=R(u)*cos(theta);
   yi=R(u)*sin(theta);
   for j=1:n
      for k=1:3
         zi(i,j,k)=sqrt(L(u).^2-(x(j)-xi(k)).^2-(y-yi(k)).^2)+z;
      end
      for k=1:3
         if isreal(zi(i,j,1)) && isreal(zi(i,j,2)) && isreal(zi(i,j,3))
           J(i,j,k,1)=(x(j)-xi(k))/(z-zi(i,j,k));
           J(i,j,k,2)=(y-yi(k))/(z-zi(i,j,k));
           J(i,j,k,3)=1;
         else
           J(i,j,k)=0;
         end
      end
      if J(i,j,k)~=0
        K(i,j)=cond([J(i,j,1,1),  J(i,j,1,2),  J(i,j,1,3);  J(i,j,2,1),  J(i,j,2,2),  J(i,j,2,3);  J(i,j,3,1),  J(i,j,3,2),
J(i,j,3,3)] );
      else
        K(i,j)=Inf;
        end
   end
   LCI(u,:)=1./K;
end
 rgcmic=zeros(2,n);
for u=1:n
   rgcmic(1,u)=L(u);
   for i=1:n
      if LCI(u,i)>=0.3
         rgcmic(2,u)=-x(i);
         break
      end
   end
end
```

Appendix C:

E3D Nozzle Design Document

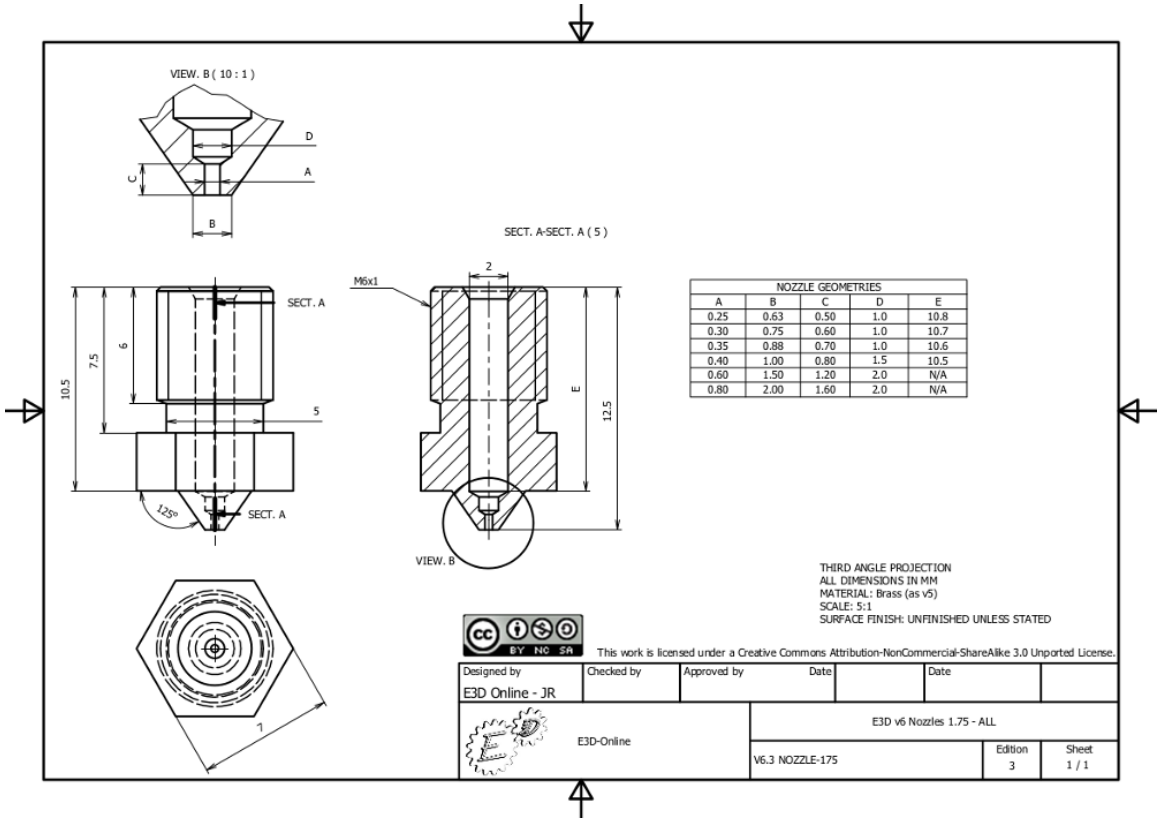

NOZZLE GEOMETRIES				
A	B	C	D	E
0.25	0.63	0.50	1.0	10.8
0.30	0.75	0.60	1.0	10.7
0.35	0.88	0.70	1.0	10.6
0.40	1.00	0.80	1.5	10.5
0.60	1.50	1.20	2.0	N/A
0.80	2.00	1.60	2.0	N/A

Appendix D:

Modified E3D Heater Block for P3D Nozzles

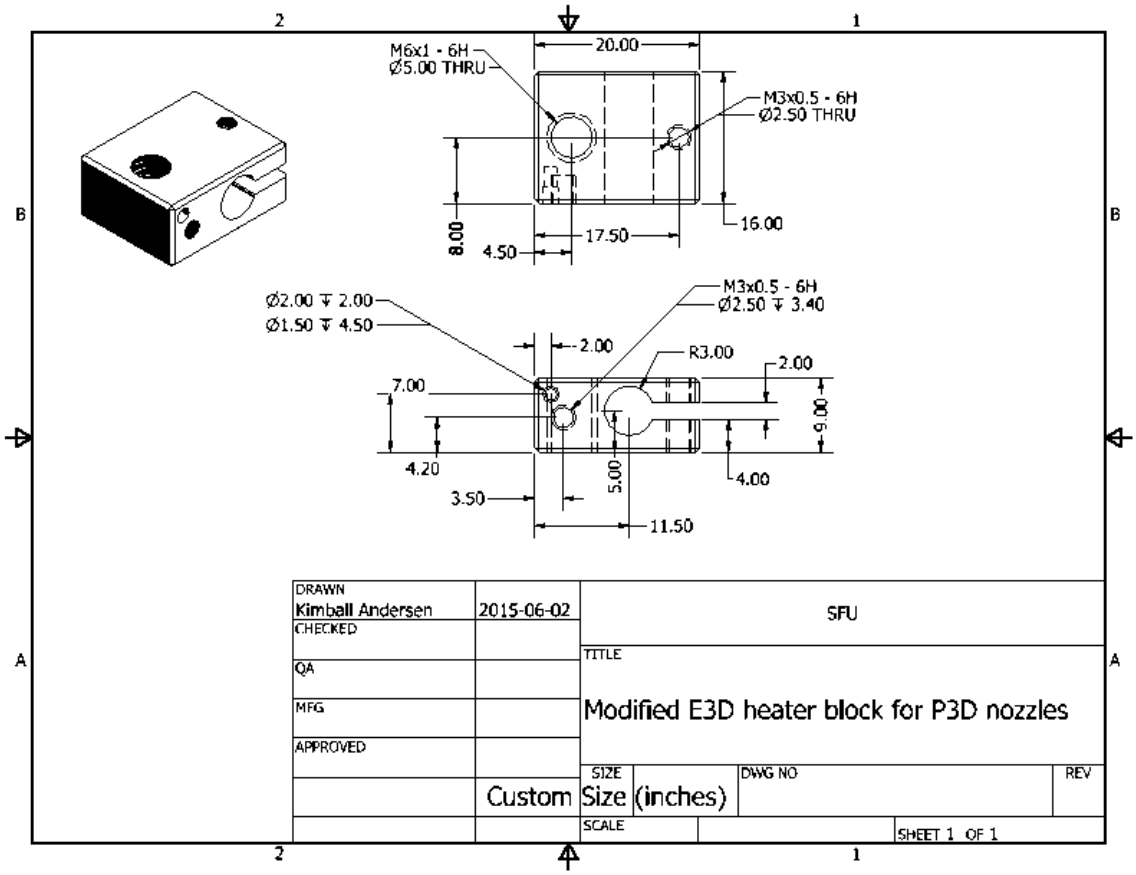

Appendix E:

Phase diagrams of binary and ternary alloy systems

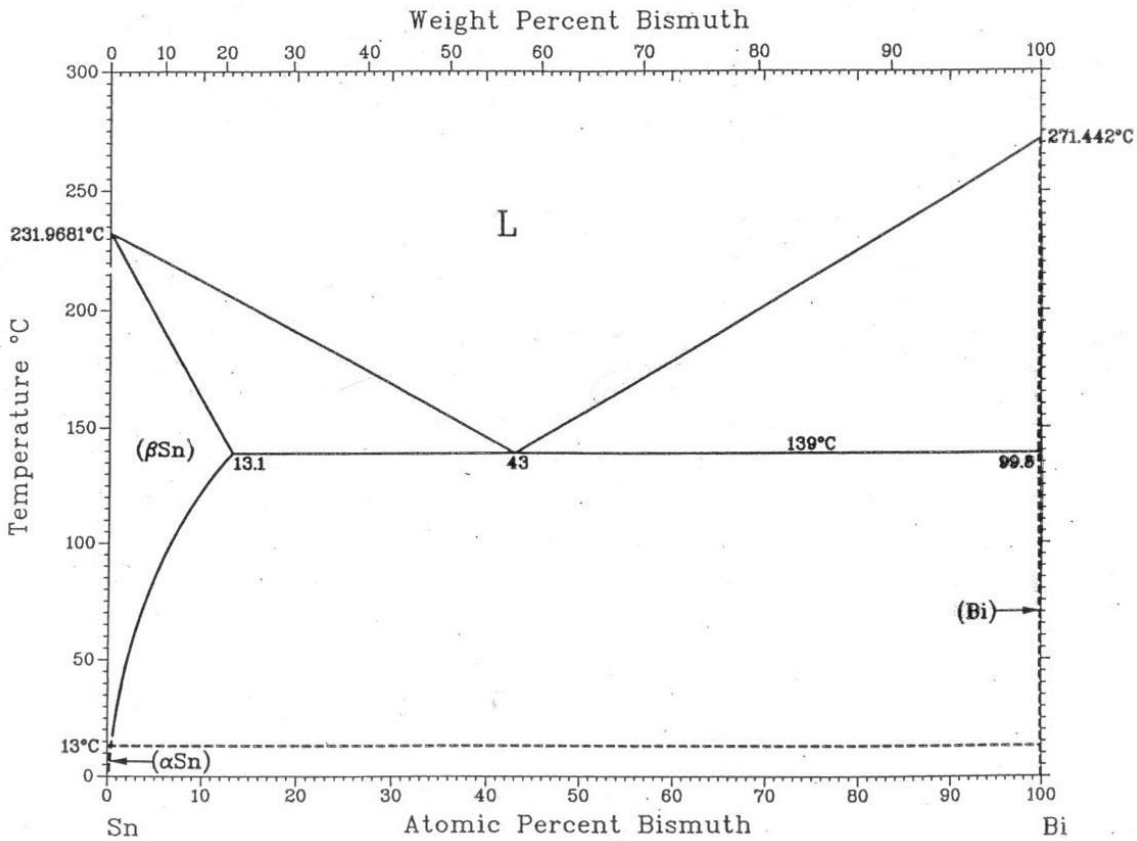

From [89]

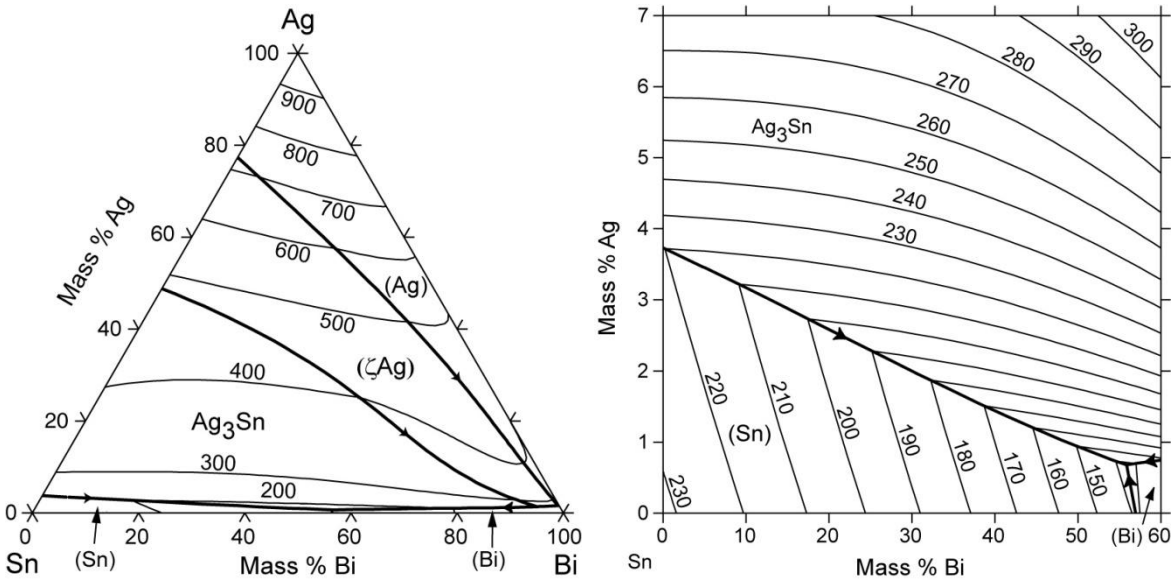
Ag
100
900
80
800
700
60
600
(Ag)
Mass % Ag
40
500
(ζAg)
400
20
Ag3Sn
300
200
0
0
20
40
60
80
100
Sn
(Sn)
Mass % Bi
(Bi)
Bi
7
6
5
4
3
2
1
0
300
290
280
270
260
250
240
230
Ag3Sn
220
210
200
190
180
170
160
150
(Sn)
230
0
10
20
30
40
50
(Bi) 60
Sn
Mass % Bi

From [76]

Appendix F:

Activity series of metals

Public domain image [95].

Activity Series of Metals

The rule: From this Activity Series, any element in its free state will replace any element beneath it that is in a compound.

lithium	Li	React with water to replace and release H_2 gas
potassium	K	
barium	Ba	
strontium	Sr	
calcium	Ca	
sodium	Na	
magnesium	Mg	React with acids to replace and release H_2 gas
aluminum	Al	
manganese	Mn	
zinc	Zn	
chromium	Cr	
iron	Fe	
cadmium	Cd	
cobalt	Co	
nickel	Ni	
tin	Sn	
lead	Pb	
hydrogen	H	
copper	Cu	
arsenic	As	
bismuth	Bi	
antimony	Sb	
mercury	Hg	
silver	Ag	
platinum	Pt	
gold	Au	

Appendix G:

DSC data for metal alloy samples tested

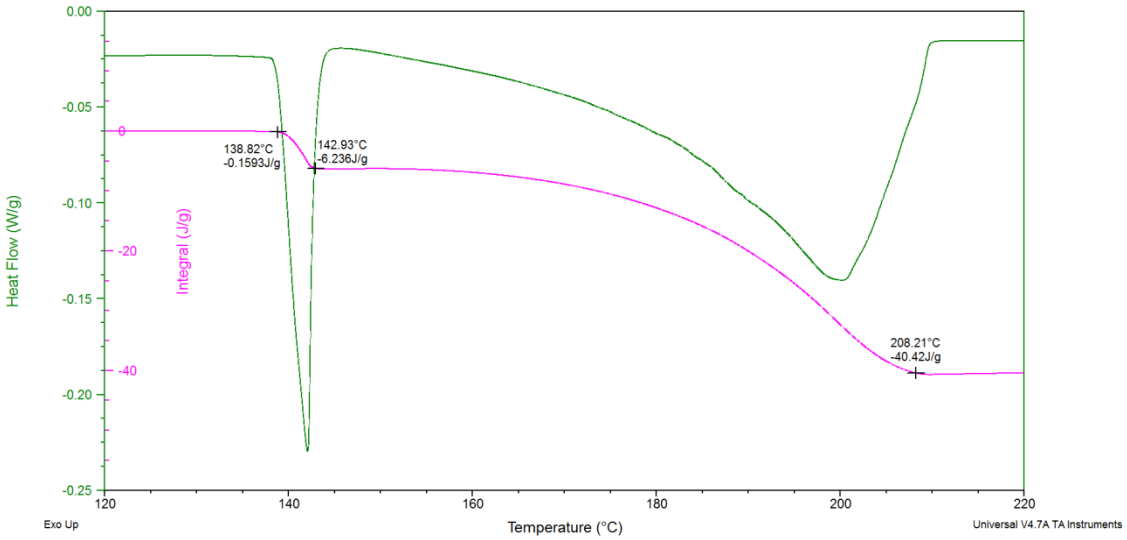

Sn80Bi20

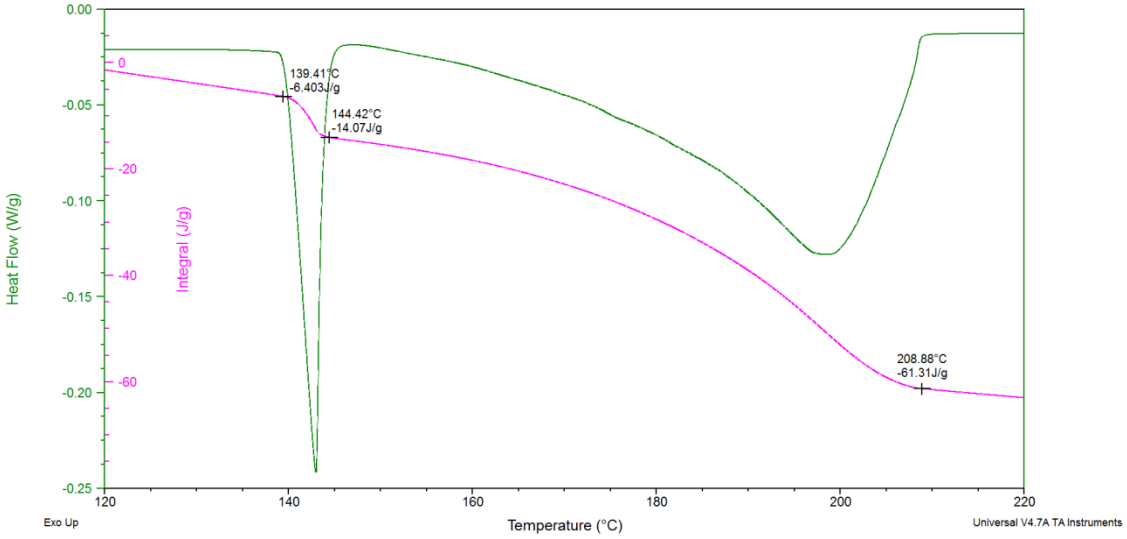

Sn70Bi30

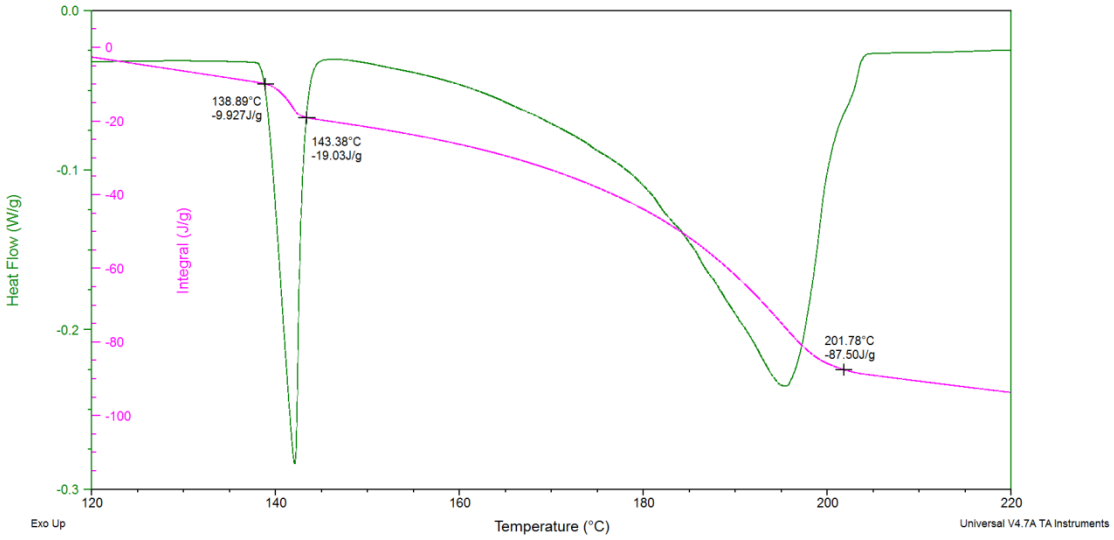

Sn76Bi20Ag<4 (due to poor mixing)

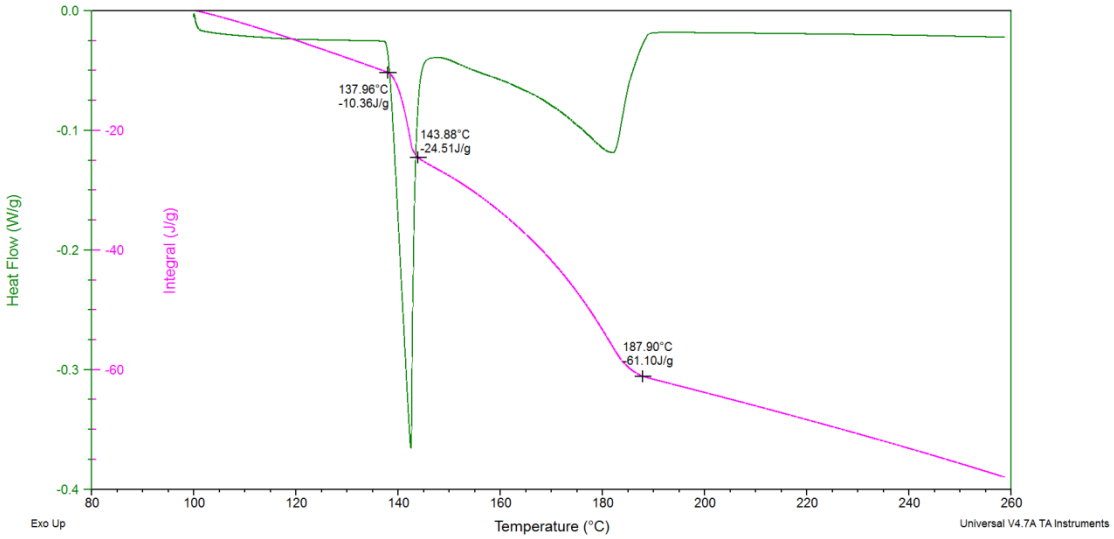

Sn66Bi30Ag4

Appendix H:

EDXS spot mapping of alloy samples

Sample 10

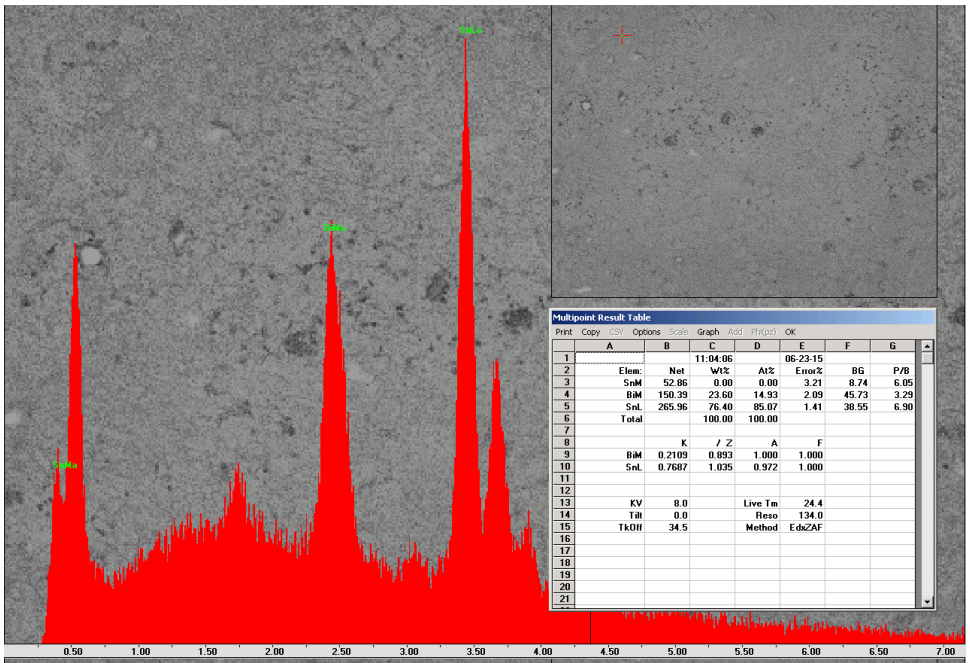

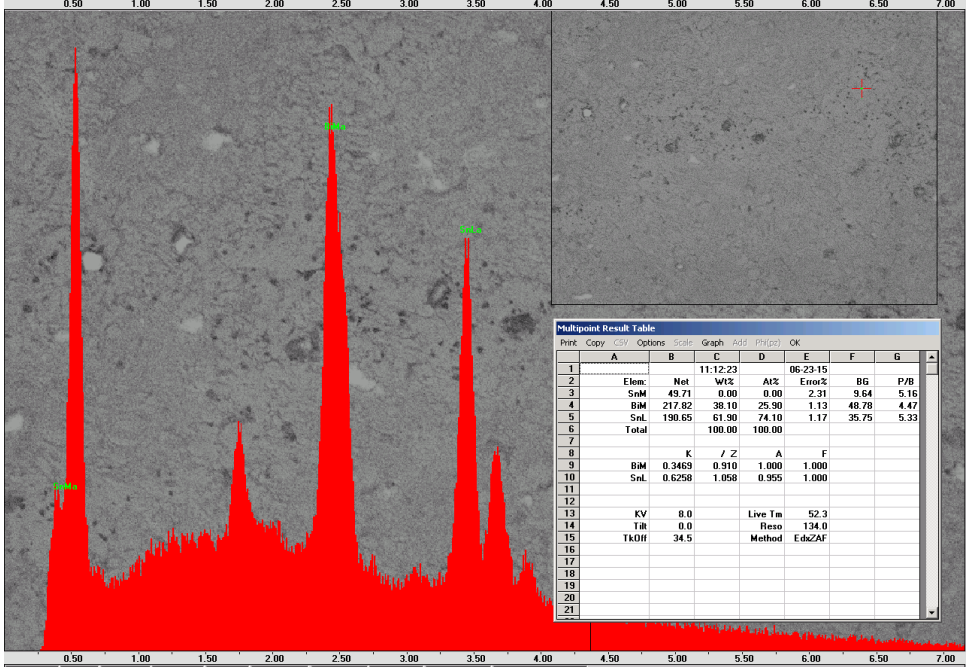

Sample 11

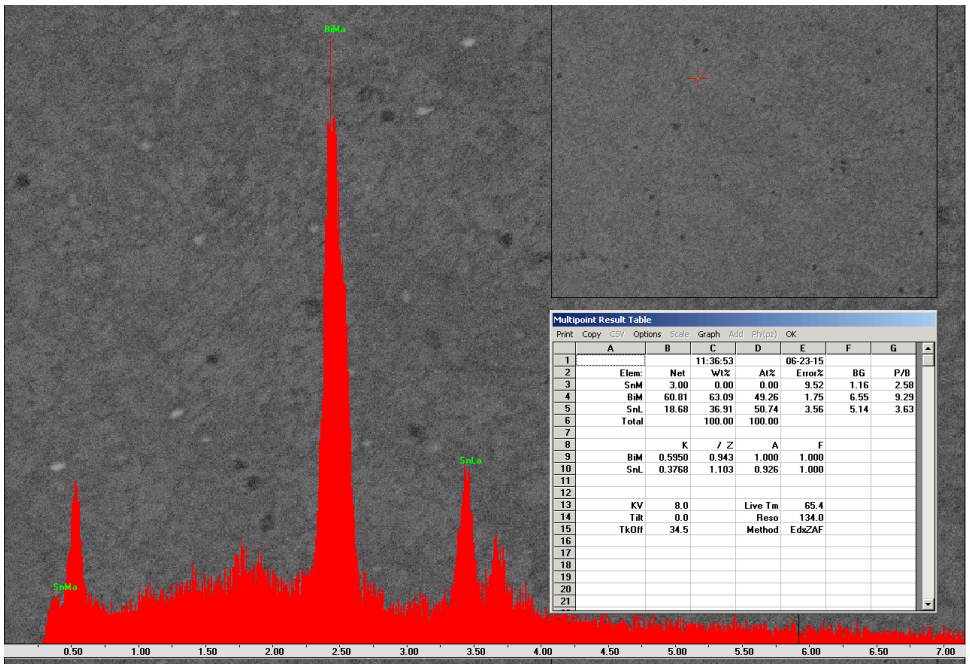

	A	B	C	D	E	F	G
1			11:36:53		06-23-15		
2	Elem:	Net	Wt%	At%	Error%	BG	P/B
3	SnM	3.00	0.00	0.00	9.52	1.16	2.58
4	BiM	60.81	63.09	49.26	1.75	6.55	9.29
5	SnL	18.68	36.91	50.74	3.56	5.14	3.63
6	Total		100.00	100.00			
7							
8		K	/ Z	A	F		
9	BiM	0.5950	0.943	1.000	1.000		
10	SnL	0.3768	1.103	0.926	1.000		
11							
12							
13	KV	8.0		Live Tm	65.4		
14	Tilt	0.0		Reso	134.0		
15	TkOff	34.5		Method	EdxZAF		
16							
17							
18							
19							
20							
21							

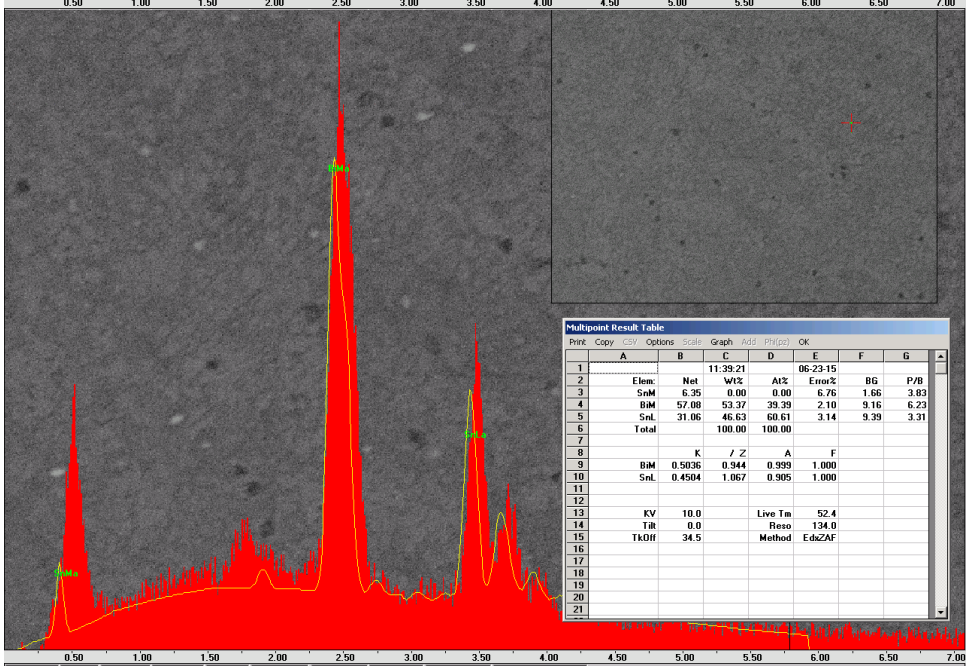

	A	B	C	D	E	F	G
1			11:39:21		06-23-15		
2	Elem:	Net	Wt%	At%	Error%	BG	P/B
3	SnM	6.35	0.00	0.00	6.76	1.66	3.83
4	BiM	57.08	53.37	39.39	2.10	9.16	6.23
5	SnL	31.06	46.63	60.61	3.14	9.39	3.31
6	Total		100.00	100.00			
7							
8		K	/ Z	A	F		
9	BiM	0.5036	0.944	0.999	1.000		
10	SnL	0.4504	1.067	0.905	1.000		
11							
12							
13	KV	10.0		Live Tm	52.4		
14	Tilt	0.0		Reso	134.0		
15	TkOff	34.5		Method	EdxZAF		
16							
17							
18							
19							
20							
21							

Sample 13

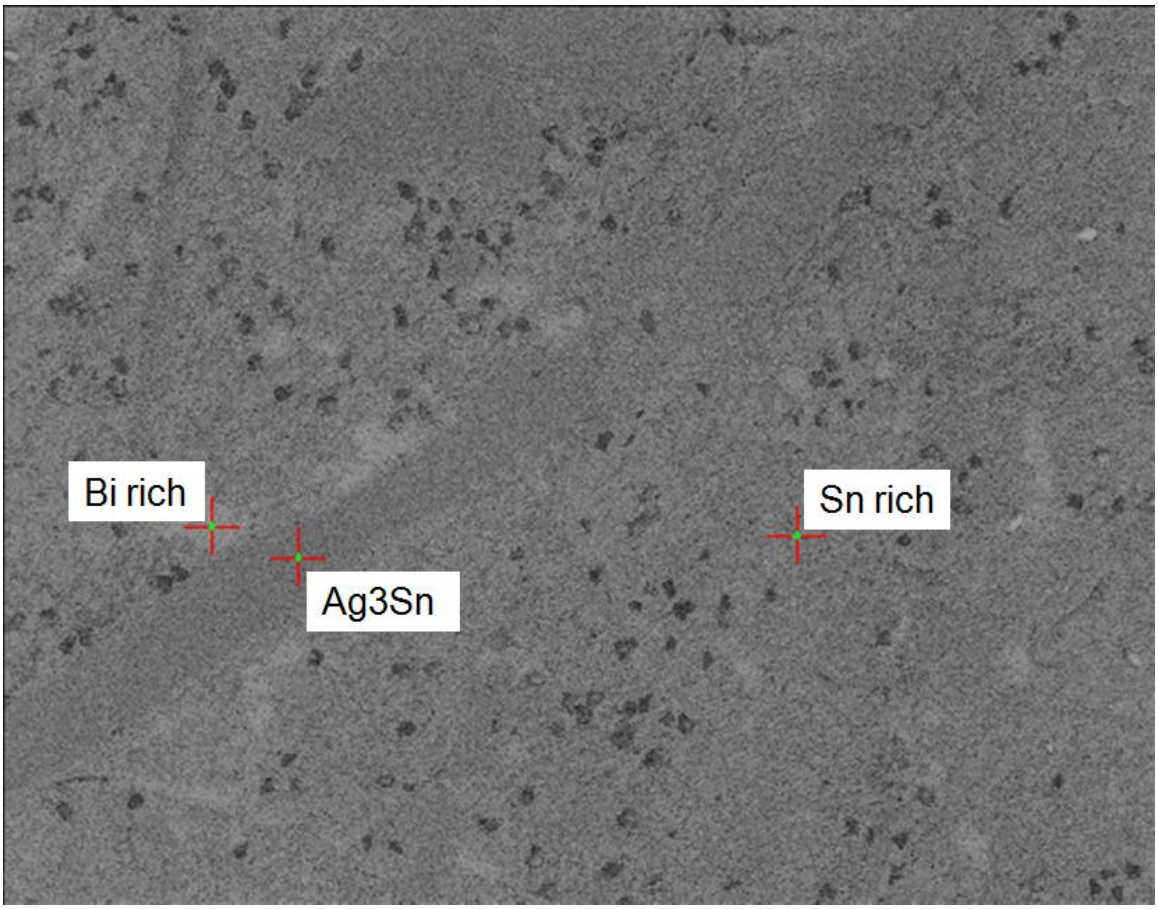

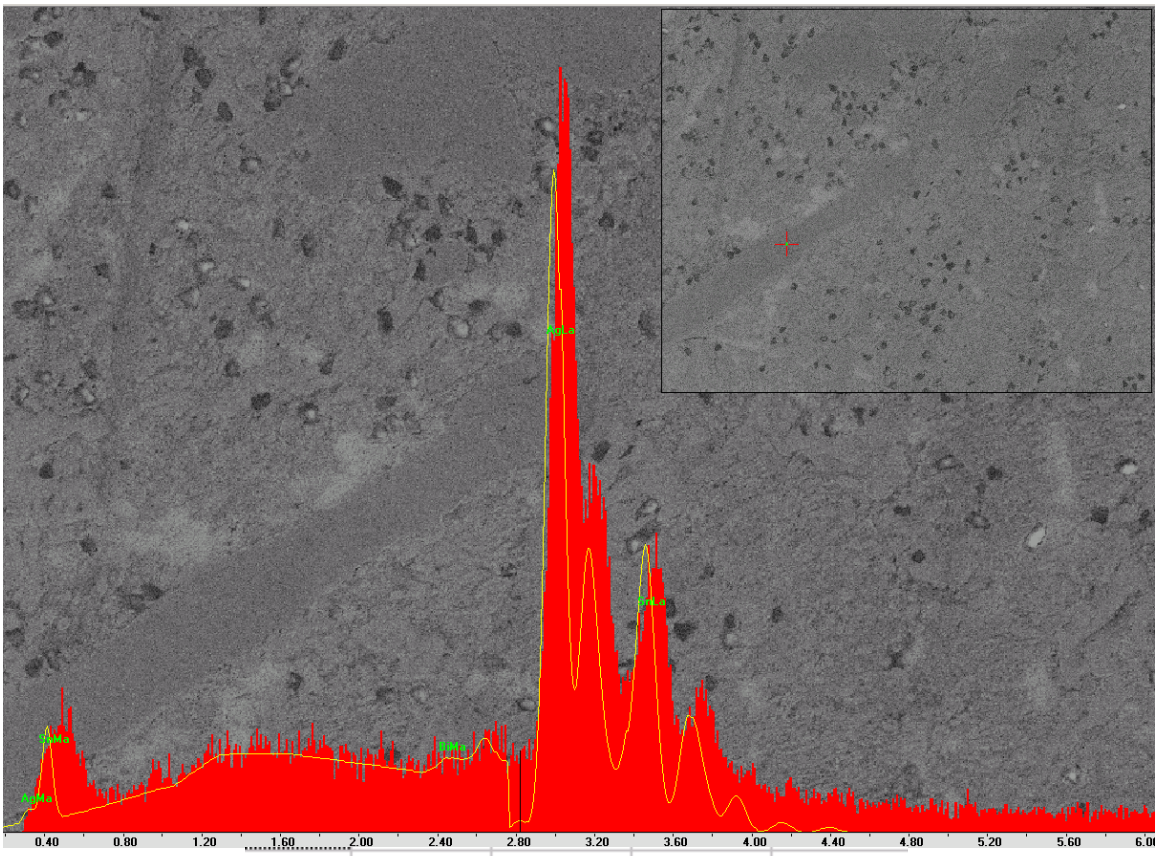

Elem:	Net	Wt%	At%	Error%
AgM	0.72	0.00	0.00	21.64
SnM	5.00	0.00	0.00	5.60
BiM	0.74	0.73	0.39	53.45
AgL	56.13	59.73	62.19	1.44
SnL	25.24	39.54	37.42	2.14
Total		100.00	100.00	
	K	/ Z	A	F
BiM	0.0065	0.873	1.016	1.001
AgL	0.6080	1.017	0.991	1.009
SnL	0.3618	0.975	0.938	1.000
KV	10.0		Live Tm	86.2
Tilt	0.0		Reso	134.0
TkOff	34.5		Method	EdxZAF

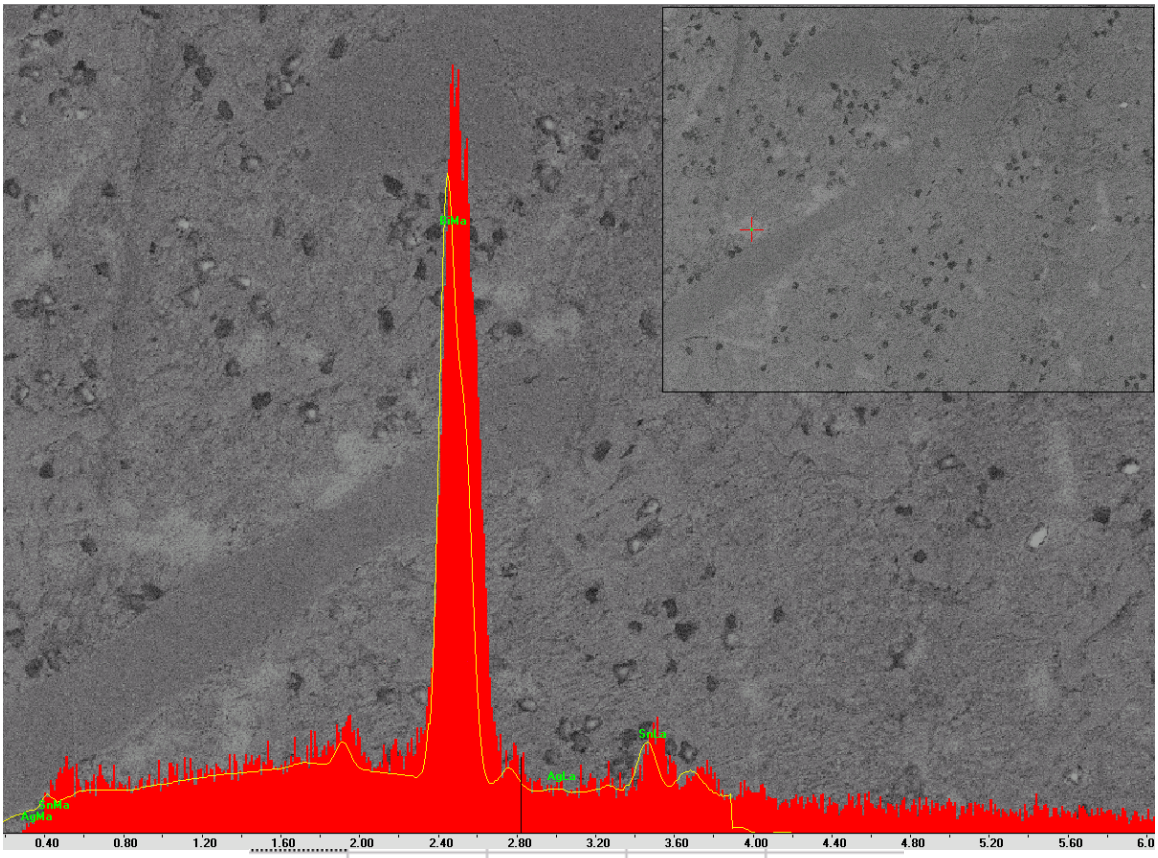

Elem:	Net	Wt%	At%	Error%
AgM	0.00	0.00	0.00	0.00
SnM	1.70	0.00	0.00	34.22
BiM	130.07	85.86	77.40	1.65
AgL	1.17	0.99	1.74	71.51
SnL	11.69	13.15	20.86	9.12
Total		100.00	100.00	
	K	/ Z	A	F
BiM	0.8426	0.981	1.000	1.000
AgL	0.0094	1.156	0.818	1.002
SnL	0.1245	1.117	0.848	1.000
KV	10.0		Live Tm	34.1
Tilt	0.0		Reso	134.0
TkOff	34.5		Method	EdxZAF

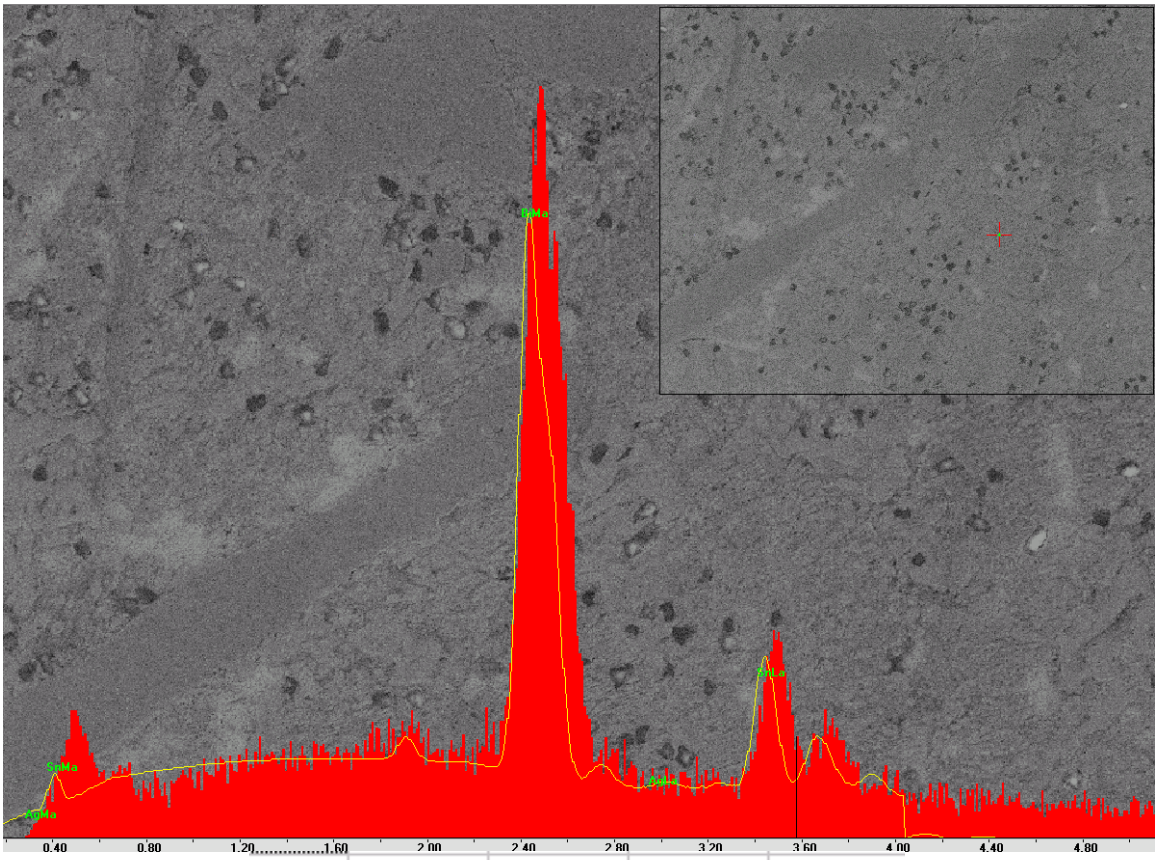

Elem:	Net	Wt%	At%	Error%
AgM	0.00	0.00	0.00	0.00
SnM	1.63	0.00	0.00	17.42
BiM	44.11	68.80	55.54	1.96
AgL	0.42	0.81	1.27	89.17
SnL	11.80	30.39	43.19	4.67
Total		100.00	100.00	
	K	/ Z	A	F
BiM	0.6610	0.961	1.000	1.000
AgL	0.0078	1.129	0.849	1.004
SnL	0.2906	1.090	0.877	1.000
KV	10.0		Live Tm	75.5
Tilt	0.0		Reso	134.0
TkOff	34.5		Method	EdxZAF

Appendix I:

Early test of SnZn eutectic commercial solder alloy

Material

This was the first metal material tested, and consisted of a 1lb roll of 4mmØ wire consisting of a eutectic composition of 85% tin, 15% zinc. Source: http://www.rotometals.com/product-p/zinc-sheet-solder-1-pound-spoo.htm

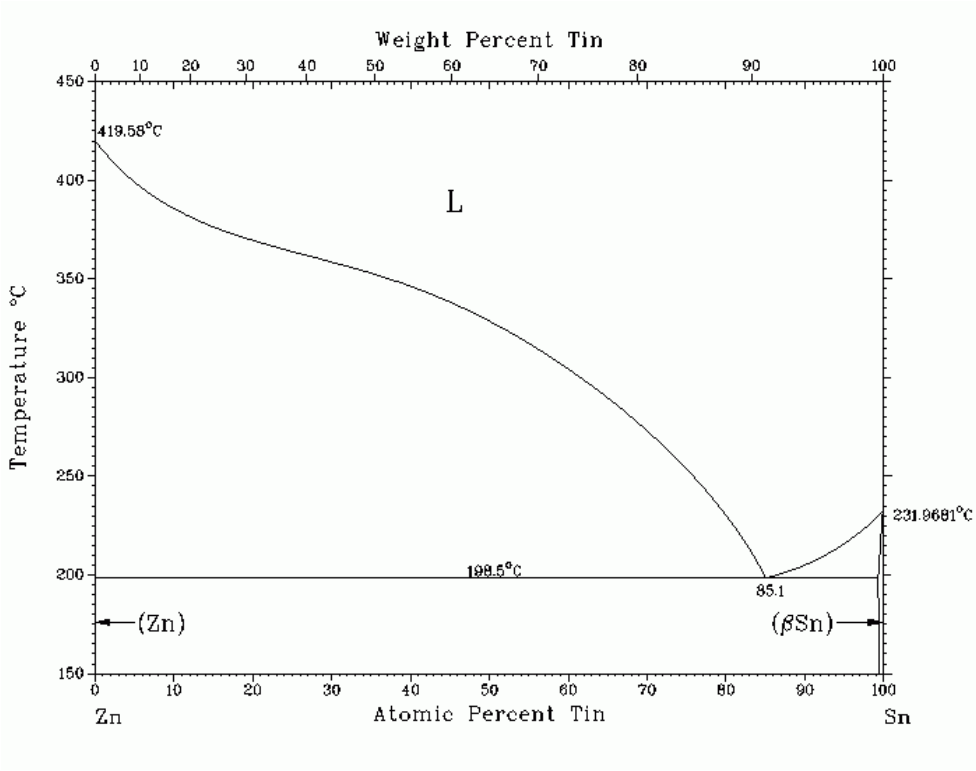

The melting point of this material is approximately 200°C, which is similar to that of common thermoplastic materials used in 3D printing such as PLA and ABS. Because the extrusion system in the Rostock Max is configured to use 1.75mmØ filament, it was necessary to draw the wire down to the proper dimensions by use of a series of dies.

Drawing

Drawing was performed manually using a tungsten carbide die drawing plate mounted in a bench vise. During each drawing step the procedure was as follows:

the wire end was filed to allow it to pass through the die

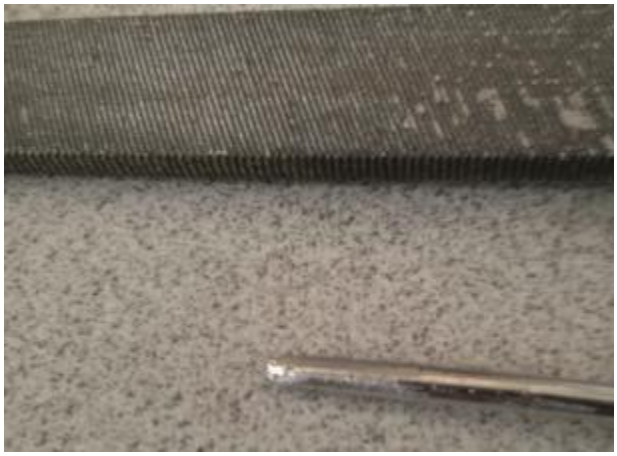

lubricant was applied to the wire

The filed end of the wire was inserted into the next smallest die (die steps were 0.1mmØ)

The end of the wire was grasped by wire drawing tongs and the filed portion was gently pulled through the die

The remaining length of the wire was pulled through the die

The SnZn alloy proved to be very ductile and drawing was succesful from 4mmØ down to 2mmØ. After 2mmØ, care was needed or necking could occur, resulting in smaller than desired filament dimensions, inconsistent dimensions, or breakage. ~5 meters of filament could be produced in a single piece in this manner from a starting length of 1m. The resulting samples were wound onto filament rolls for storage and subsequent use.

Printing

To test the printability of the material, a sample was loaded into the extrusion system of the Rostock Max. Due to the solubility of brass in molten tin which would result in damage to the standard brass nozzle on the system, it was replaced with a custom made stainless steel version produced by E3D. Due to the lower thermal conductivity of the SS versus the brass, this was expected to result in slightly higher running temperatures needed for the hot end. The nozzle was heated to 210°C, and the wire was manually fed into the system. It was discovered that the wire feed was somewhat erratic, and at while molten material could be ejected from the nozzle, the wire would sometimes stick, especially after slight retractions and/or hard extrusions. When the material was removed from the hot end, it was found that the liquid metal had backed up into the gap between the wire and the surrounding heat break barrel, causing it to cool and jam. This was suspected to be a result of the low viscosity of the molten metal, and the abrupt phase change which eutectic alloys undergo.

After attempting to compensate for this by using the minimum temperature with which successful extrusion could be achieved and slow extrusions with no retractions to prevent backflow, another problem appeared which resulted in total blockage of the nozzle: Dross. Formed by the oxidation of the metal in air at elevated temperatures, this grey crumbly material began to coat the inside of the nozzle, causing several clogs of increasing severity until the nozzle was unuseable. Switching from the standard 0.4mmØ nozzle to a larger 0.8mmØ nozzle helped for a while, but even this began to clog after a short time. Subsequent cleaning of the nozzle and extrusion with clear plastic filament showed the substantial build of Dross present.

Discussion/Conclusions

The eutectic SnZn alloy demonstrated that metal filament printing may be possible with the current system, but several hurdles must be overcome. The low melt viscosity and abrupt phase change in the melt chamber mean that under high pressure, back flow will be an issue. Switching to a Non-Eutectic alloy would remove the abrupt phase transition, thus allowing a more gradual melt onset and viscosity change. Controlling microstructure then may prove critical to ensuring the filament behaves as desired. Preventing oxidation of the metal filament in the melt chamber is also critical, so preventing air from entering the system and/or adding an oxide scavenger to prevent Dross build up will be essential. Pressurizing the Bowden delivery tube with anaerobic gas could be achieved, however sealing the filament entry would prove difficult. A better option was discovered in the form of a Dross inhibitor solution designed for use in wave solder applications. This solution floats on the surface of the molten solder to form an airtight barrier over the melt to prevent oxygen from entering. It also contains oxide scavenger molecules which can dissolve any Dross that has formed and prevent it from building up and clogging the system. This fluid could be used to fill the bowden delivery tube of the printer, which would be sealed at the bottom to the nozzle, preventing any air from entering the system except through the nozzle tip. Recirculating the inhibitor solution may be necessary to ensure a fresh supply where needed.

http://www.pkaymetal.com/index.php/ms2-dross-eliminator/

Followup

Attempts to use the MS2 dross inhibitor ended in failure, with the MS2 overheating in the system, and turning into a thick black tar-like material which then clogged then nozzle.

Appendix J:

Record of experimental conditions and results for stainless steel nozzle print calibration

0.25mm SS nozzle used with Sample 13 Sn66Bi30Ag4

Nozzle Temp (C) (1st/rest)	Bed Temp (C)	Fan (on/off)	Layer (mm) (1st/rest)	Ext width (mm) (1st/rest)	Speed (mm/s)/ Accel	Retraction Spd/dist	Move Speed/ Accel	Slicer	image
200/220	100	100%	0.4/0.4	0.7/0.6	15/500	30/0.5	90/1000	Slic3r	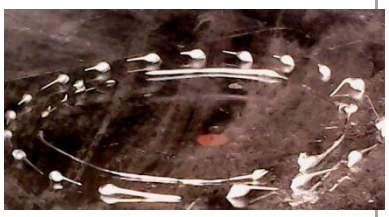
210	100	100%	0.4/0.4	0.7/0.6	3/500	30/0.5	15/1000	Slic3r	
215/225	100	100%	0.3/0.3	0.7/0.5	(2)3/500	30/0.5	30/1000	Slic3r	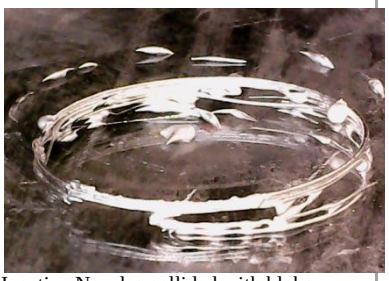 Inactive Nozzles collided with blobs. Retesting. Preference for long thin strings with beads indicates extrusion speed may be too high. Reducing layer height and extrusion width may help.

Nozzle Temp (C) (1st/rest)	Bed Temp (C)	Fan (on/off)	Layer (mm) (1st/rest)	Ext width (mm) (1st/rest)	Speed (mm/s)/ Accel	Retraction Spd/dist	Move Speed/ Accel	Slicer	image
210/225	100	100%	0.25/0.25	0.4/0.4	(2)5/500	30/0.5	30/1000	Slic3r	Reliable extrusion is difficult. Presence of oxides clogging nozzle? Higher melting alloys introduce greater oxidation rates.

Appendix K:

Record of experimental conditions and results for anodized nozzle print calibration 1

Layer 1 height	Layer height	Layer 1 width	Perimeter width	Layer 1 Speed	Perimeter Speed	Image	Notes
0.4	0.3	0.5	0.5	20%	60		
0.1	0.3	0.5	0.5	20%	60		
0.1	0.3	0.75	0.5	20%	60		
.1	.3	.75	.75	20%	30		Decreased move speed when not printing to 30

Layer 1 height	Layer height	Layer 1 width	Perimeter width	Layer 1 Speed	Perimeter Speed	Image	Notes
0.3	0.3	1	.75	20%	30		
0.3	0.3	1	1	50%	10		Disabled spiral vase mode to see if retract/move is better. Note the spike tails generated whenever a break occurs in the extrusion. This occurs on the opposite end of the segment from the nozzle, as it breaks away from the previously printed segment This appears to be a surface tension related effect. Evidence of anodization failure:

Layer 1 height	Layer height	Layer 1 width	Perimeter width	Layer 1 Speed	Perimeter Speed	Image	Notes
.3	.3	1	1	50%	10		Ran out of Sn Bi filament, so switched to mystery composition filament (Same settings as previous for comparison) Inactive head collisions with printed areas are of concern, causing printed traces to be knocked off, and subsequent extrusion to fail.
.3	.3	1	1	50%	10	 Saved as Sample 1	Inactive nozzles elevated from build plane. It appears that limited adhesion to the build surface, coupled with minor variations in height of the surface of the printed part, causes small elevations in the surface of the extruded traces, resulting in obstacles for the other heads to collide with. Collisions then misplace traces, causing the resulting failure of the print.
.3	.3	1	.75	50%	10	 Sample 2	Fan was turned on ~half way up the print, and resulted in much more definition between layers. Suggest using fan for subsequent trials, as it will improve cornering as well as lateral resolution capabilities.

Layer 1 height	Layer height	Layer 1 width	Perimeter width	Layer 1 Speed	Perimeter Speed	Image	Notes
.3	.3	1	.5	25%	20	Sample 3	Nozzle showing additional signs of wear
.3	.3	1	.5	5	100	Sample 4	Melted region in the foreground was where the layer change was occuring, and as a result of the slower move speed, extra material was being deposited there during the move.
.3	.3	1	.6	5	50	Sample 5	Pause caused by retraction appears to be a problem. Is retraction even necessary for this filament?

Layer 1 height	Layer height	Layer 1 width	Perimeter width	Layer 1 Speed	Perimeter Speed	Image	Notes
.3	.3	1	.6	5	50	Sample 6	Disabled retraction: Definite improvement, but still having trouble with gaps forming at the layer change point. Extrusion width too low? Measured filament diameter: 1.65mm. Changed from 1.7-1.65 in slicer settings.
.3	.2	1	.6	5	50	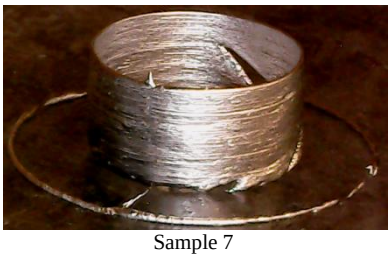 Sample 7	Gaps in initial layer resulted in later failures. Initial layer is critical. Temperature curve shows a drastic drop in temperature after the initial peak, suggesting that the thermal transfer to the glass bed is causing poor extrusion. 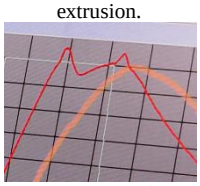 Slower first layer? What of a solid fill first layer?
.3	.2	1.25	.6	2.5	50	Sample 8	Bottom layer failed to print well, and was knocked free. Low speed appeared to result in poor bottom layer. Increase speed? Also, enable fan? Try to enable fan during warm up to try to prevent temperature drop…
.3	.2	1.25	.6	50	50	Sample 9	Surface tension effects very noticeable. Lower 1st layer height needed? Lower extrusion temperature?

Layer 1 height	Layer height	Layer 1 width	Perimeter width	Layer 1 Speed	Perimeter Speed	Image	Notes
.2	.2	1.25	.6	50	50	Discarded	Disabling retraction also disables Z-hop, which is necessary. This is the cause of the destruction of the infill. Setting a 0.001mm retraction allows the re-enabling of the z-hop feature, without a noticeable retraction. Nozzle erosion has now resulted in a increased effective nozzle height, so calibration is difficult. Also, because of the wetting of the exposed aluminum, the effective nozzle diameter has increased substantially.
.2	.2	1.25	.6	50	50	Discarded	Effective Z-hopping allowed infill to remain undisturbed. Unfortunately, miscalibration and oversized nozzle are now dominating problem. Changing nozzle to fresh coated nozzle, with lighter shade of hard-coat (observed to have porous surface structure under microscope, which may help prevent cracking from thermal stress. Nozzle cleaning for post-use analysis showed minimal oxide buildup Inspection of the nozzle shows that the internal anodization is intact.

Removing the old nozzle:
When removing the old nozzle, the oxide coating on the threads disintegrated, causing potentially worrysome abrasion inside the heater block. Upon removal, the debris was examined:

Similar thermal stress patterns as those witnessed on the tip are evident, and the sharp edges formed by the cracks are certain to have caused damage to the internal threads of the heater block. A new heater block may need to be made at some point if nozzles will need to be exchanged regularly.

Inserting the new nozzle:
Cracking on the surface of the nozzle became apparent immediately upon insertion:

Great care was taken this time to install it at only a modest 170C. Also, care will be taken to subject the nozzle to as little impact as possible.

When the oxide layer is intact, the contact angle of the molten metal is very high:

If care is taken, even though the layer is cracked, it should be possible to preserve it:

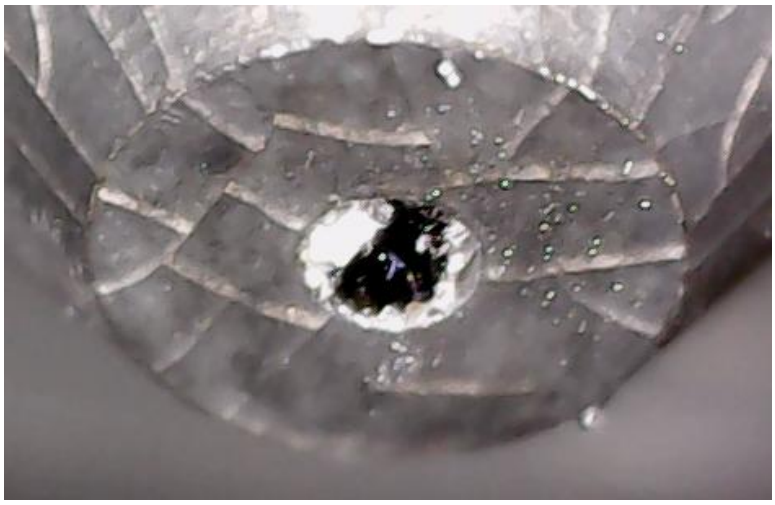

Orifice shown after printing sample 10

Layer 1 height	Layer height	Layer 1 width	Perimeter width	Layer 1 Speed	Perimeter Speed	Image	Notes
.2	.2	1	.6	50	50	Sample 10	It appears that surface tension effects are a problem on the first layer, perhaps a larger layer height is needed?

.4	.2	1	.6	50	50	Discarded	It appears that each pair of passes in the infill results in one fat line, followed by a gap. The expected increase in performance from the larger 1st layer height was not observed, and in fact the first layer printed worse. More careful calibration of the nozzle height may be needed, and the first layer height and extrusion width may need to be decreased to ensure good fidelity.

Appendix L:

Record of experimental conditions and results for electroless nickel coated nozzle print calibration

Image of nozzle tip after three calibration prints

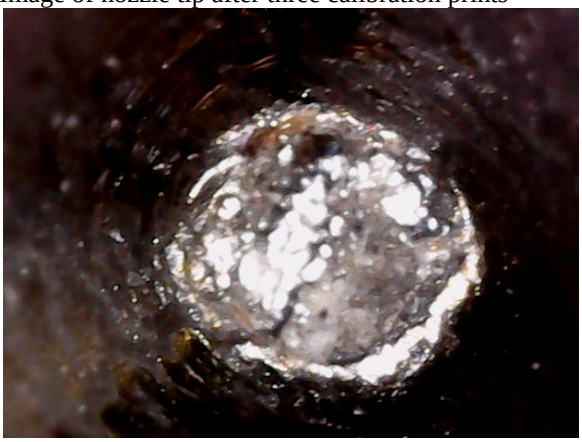

No Evidence of degradation, but wetting of the nozzle's outer surface was observed.

Test Printing of Sn70Bi30 filament
0.4mm EN coated brass nozzle printing a 3cm diameter cylinder with a single perimeter spiralized

Nozzle Temp (C)	Bed Temp (C)	Fan (on/off)	Layer (mm) (1st/rest)	Ext width (mm) (1st/rest)	Speed (mm/s)/ Accel	Retraction Spd/dist	Move Speed/ Accel	Slicer	image
185	100	Off	0.4	0.5	2/9000	30/0.5	150/ 9000	Cura	
185	100	Off	0.4	0.5	2/9000	30/0.5	150/ 9000	Cura	Nozzle Clog occurred. After removing the filament, it was found that the nozzle cleared as soon as the temperature was increased to 215, suggesting higher T_m components of the alloy were remaining in the nozzle as solids, but melted when the temperature was raised. This suggests that there is sufficient time for the two phases to separate and jamming is occuring in the particles of the solid phase.

Nozzle Temp (C)	Bed Temp (C)	Fan (on/off)	Layer (mm) (1st/rest)	Ext width (mm) (1st/rest)	Speed (mm/s)/ Accel	Retraction Spd/dist	Move Speed/ Accel	Slicer	image
195	100	Off	0.4	0.5	2/9000	30/0.5	150/ 9000	Cura	Some acceptable extrusion, but beading due to surface tension was a problem. Increase speed to decrease residual heat transfer in the printed material?
195	100	Off	0.4	0.5	5/9000	30/0.5	150/ 9000	Cura	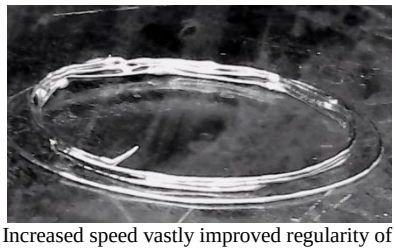 Increased speed vastly improved regularity of the extrudate. Further increase may further improve it. Of note, spiralize contour was not enabled until after this print. Also, it was noted that the non-print move speed was too rapid, causing the material in the nozzle to come out when lifted, and fail to extrude when it was dropped.
195	100	Off	0.4	0.5	10/9000	30/0.5	30/ 9000	Cura	Skirt extrusion was measured to confirm extrusion multiplier, found to be 0.5mm height, so nozzle height was reduced slightly. Also, acceleration for moves and printing was reduced to 200mm/s^2
190	100	Off	0.4	0.5	10/200	30/0.5	30/ 200	Cura	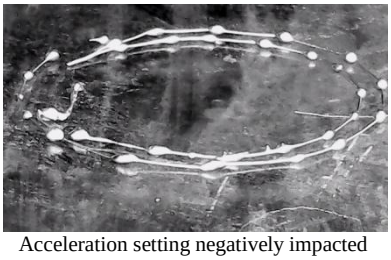 Acceleration setting negatively impacted print speed.

Nozzle Temp (C)	Bed Temp (C)	Fan (on/off)	Layer (mm) (1st/rest)	Ext width (mm) (1st/rest)	Speed (mm/s)/ Accel	Retraction Spd/dist	Move Speed/ Accel	Slicer	image
190	100	Off	0.4	0.5	10/3000	30/0.5	30/200	Cura	
190	100	Off	0.4	0.5	10/9000	30/0.5	30/1000	Cura	Reducing temperature seems to be the cause of worse extrusion.
200	100	Off	0.4	0.5	20/9000	30/0.5	30/1000	Cura	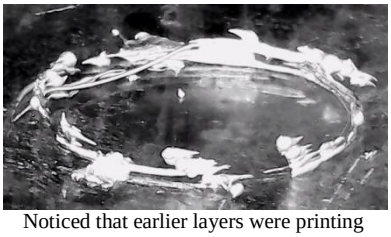 Noticed that earlier layers were printing slower, due to a bug in the cooling routine.
200	100	Off	0.4	0.5	10/9000	30/0.5	30/1000	Cura	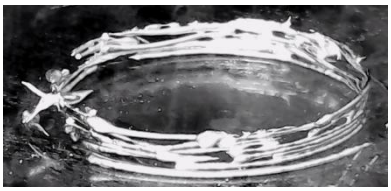 By setting the lower and upper bounds of the print speed settings equal, no scaling in speed occurred.
210	100	Off	0.4	0.5	10/9000	30/0.5	30/1000	Cura	Drain-pause extrusion was observed as a result of the reduced viscosity and large melt volume. Filament jamming was also witnessed, most likely due to backwash of molten filament in the delivery tube.

Nozzle Temp (C)	Bed Temp (C)	Fan (on/off)	Layer (mm) (1st/rest)	Ext width (mm) (1st/rest)	Speed (mm/s)/ Accel	Retraction Spd/dist	Move Speed/ Accel	Slicer	image
200	100	Off	0.4	0.75	5/9000	30/0.5	30/1000	Cura	Some Extrusion failure due to filament jamming. Increasing tension spring may help.
195	100	On	0.4/0.3	.6	5/500	30/0.5	30/1000	Slic3r	First layer printed well, but extrusion failures occurred after the first layer.
230	100	On	0.4/0.3	0.6	5/500	30/0.5	30/1000	Slic3r	The combination of the higher temperature (Approximately the melting point of tin itself) and the fan seems to result in good print results. **(SAVED AS SAMPLE 1)**
230	100	On	0.4/0.3	0.6	5/500	30/0.5	30/1000	Slic3r	Print model was changed to a 2x2 array of 1cm cylinders to test retraction settings. Because of the small retraction distance and Z-hop, small burs were occasionally left on the surface of the layer, which could be collided into by the nozzle, knocking the part off the bed. Adding the wipe while retracting flag may help minimize this. An extra length on restart may also help with the gaps in the perimeters. **(SAVED AS SAMPLE 2)**

Nozzle Temp (C)	Bed Temp (C)	Fan (on/off)	Layer (mm) (1st/rest)	Ext width (mm) (1st/rest)	Speed (mm/s)/ Accel	Retraction Spd/dist	Move Speed/ Accel	Slicer	image
230	100	On	0.4/0.3	0.6	5/500	30/0.5 wipe	30/1000	Slic3r	Poor initial layer resulted in subsequent layer failures. Retrying with larger 1st layer extrusion width.
230	100	On	0.4/0.3	1/0.6	5/500	30/0.5 wipe	30/1000	Slic3r	Extrusion seems to be stalling, larger extrusion widths, and an increasing first layer height suggest erosion of the nozzle. Imaging confirms this is likely... The smooth orifice of the nozzle evident here, is in sharp contrast to the rough orifice previously imaged. Cleaning and further imaging needed to confirm.

EN coated Brass nozzle after testing

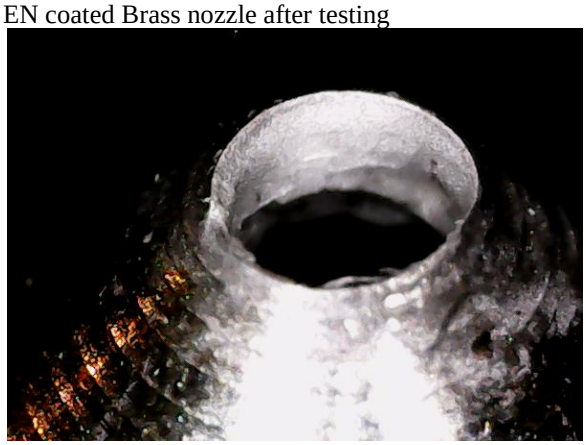

Diameter of orifice was measured to exceed 0.8mm

Image of a brand new nozzle at the same magnification, and the same position.

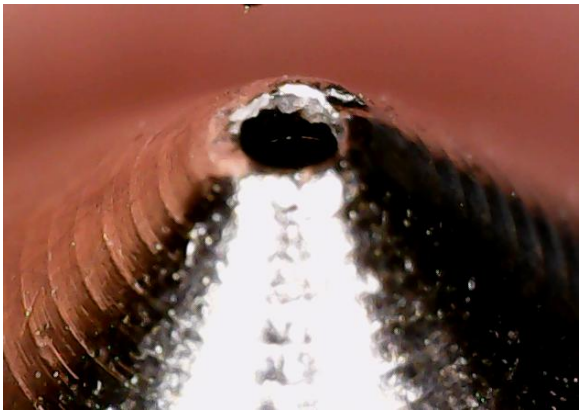

Inside of the rear entrance to the barrel of the nozzle after extrusion

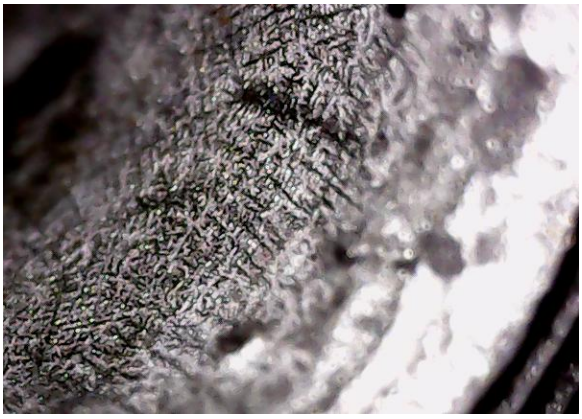

Brand new nozzle rear barrel view

Appendix M:

Record of experimental conditions and results for anodized nozzle print calibration 2

This test was performed with a 0.4mm nozzle with a sharp profile. The nozzle was kept heated throughout the experiment, to reduce the chance of damage from rapid thermal cycling.
In addition, the material used was:
Sn66Bi30Ag4

Nozzle Temp (C) (1st/rest)	Bed Temp (C)	Fan (on/off)	Layer (mm) (1st/rest)	Ext width (mm) (1st/rest)	Speed (mm/s)/ Accel	Retraction Spd/dist	Move Speed/ Accel	Slicer	image
200	100	On	0.6/0.6	0.7/0.6	5/500	30/0.5	30/1000	Slic3r	High layer heights, combined with high cooling, resulted in distinct wires on each layer, which did not adhere.
200/220	100	75%	0.4/0.4	0.7/0.6	5/500	30/0.5	30/1000	Slic3r	SUCCEEEESSSSSSSS!!!!! Nozzle still viable too!

Nozzle Temp (C) (1st/rest)	Bed Temp (C)	Fan (on/off)	Layer (mm) (1st/rest)	Ext width (mm) (1st/rest)	Speed (mm/s)/ Accel	Retraction Spd/dist	Move Speed/ Accel	Slicer	image
200/220	100	75%	0.4/0.4	0.7/0.6	5/500	30/0.5	30/1000	Slic3r	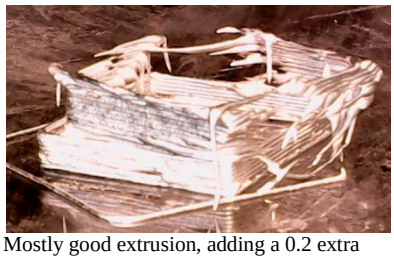 Mostly good extrusion, adding a 0.2 extra length on recovery from retraction appears to help gaps between retractions, but is too high a value, causing blobs, which then interfere with the nozzle, and cause the print to be dislodged.
200/220	100	75%	0.4/0.4	0.7/0.6	5/500	30/0.5	30/1000	Slic3r	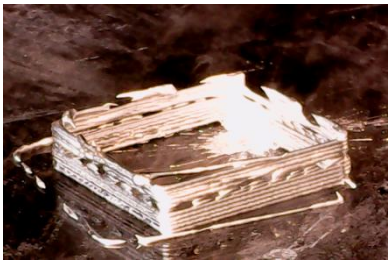 Reducing the extra length on restart to 0.1 produces a slightly better result. Lower retraction length may also help. intermittent Nozzle clog caused broken layers, reprint to investigate: Nozzle clog repeated, suggests possibly too low a temperature. Increasing upper layer temp to 225 Nozzle damage may also be the culprit:

High surface tension of the molten alloy:

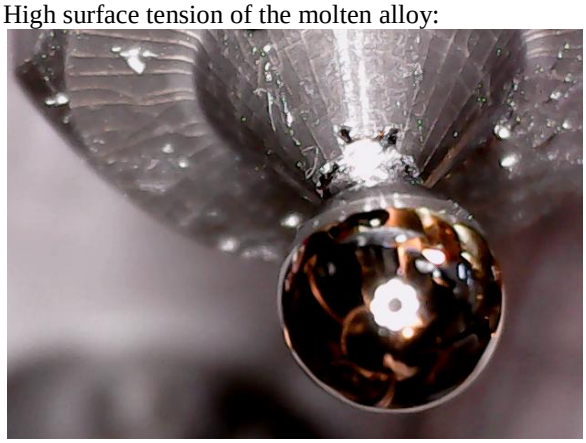

Alloy at 200C

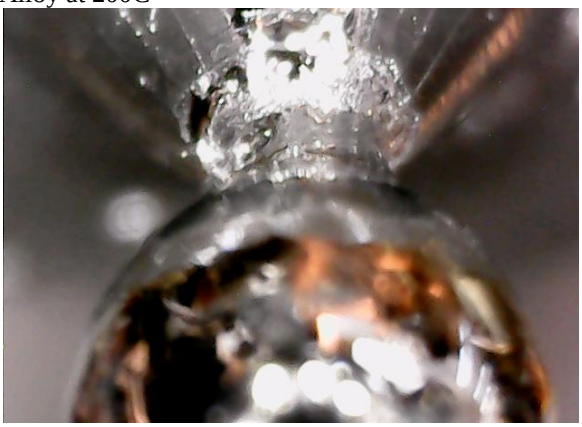

Alloy at 185, showing tip of nozzle. During retraction, movement in the space between shells of coating was observed, suggesting that the inner coating is compromized. This may have been what caused the clogging.

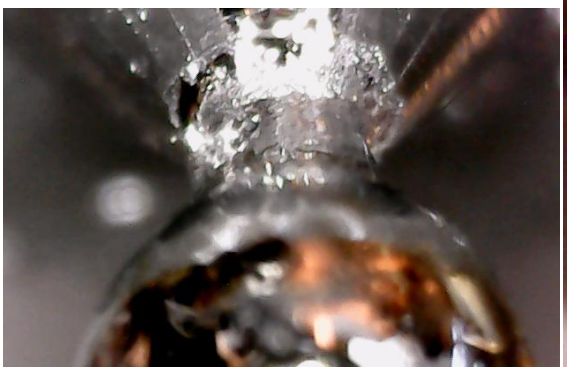

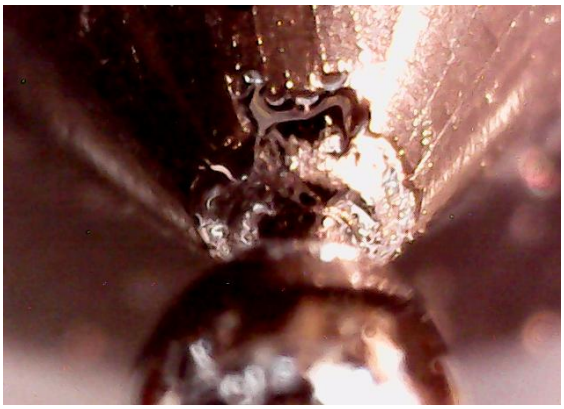

Appendix N:

Video of Sample 1 being printed

Filename:

Vid20150127160506.mp4